T.C.
YILDIZ TECHNICAL UNIVERSITY
GRADUATE SCHOOL OF NATURAL AND APPLIED SCIENCES

ADVANCED ELECTRODE/ELECTROLYTE MATERIALS FOR LOW AND INTERMEDIATE TEMPERATURE SOLID OXIDE FUEL CELLS

DİDEM BERCESTE BEYRİBEY

A DISSERTATION
CHEMICAL ENGINEERING DEPARTMENT
CHEMICAL ENGINEERING PROGRAM

SUPERVISOR
PROF. DR. SEYFETTİN ERTURAN

İSTANBUL, 2012

T.C.
YILDIZ TECHNICAL UNIVERSITY
GRADUATE SCHOOL OF NATURAL AND APPLIED SCIENCES

ADVANCED ELECTRODE/ELECTROLYTE MATERIALS FOR LOW AND INTERMEDIATE TEMPERATURE SOLID OXIDE FUEL CELLS

This thesis was presented by Didem Berceste Beyribey as partial fulfillment of the requirements for the degree, Doctor of Philosophy in Chemical Engineering at the Graduate School of Natural and Applied Science, Yıldız Technical University, 18th September 2012. The thesis was accepted by the committee members given below.

Advisor

Prof. Dr. Seyfettin ERTURAN
Yıldız Technical University

Committee members

Prof. Dr. Seyfettin ERTURAN
Yıldız Technical University ______________________

Prof. Dr. Hüseyin AFŞAR
Yıldız Technical University ______________________

Prof. Dr. Güldem ÜSTÜN
İstanbul Technical University ______________________

Prof. Dr. Hanifi SARAÇ
Yıldız Technical University ______________________

Prof. Dr. H. Ayşe AKSOY
İstanbul Technical University ______________________

This study is supported by Scientific Research Foundation of Yıldız Technical University Project No: 27-07-01-05.

To my mom and dad

ACKNOWLEDGEMENTS

This thesis is the culmination of an exciting and challenging graduate education in Chemical Engineering at the Graduate School of Natural and Applied Science, Yıldız Technical University. Its completion was only possible with the help of many individuals, to whom I would like to express my utmost respect and gratitude. First, special thanks to my advisor and mentor Prof. Dr. Seyfettin Erturan, for his support, everlasting guidance and encouragement. I could never have found my way to science without him. Similarly, to all members of Yıldız Technical University, in particular Assist. Prof. Dr. Burcu D. Çorbacıoğlu, Assist. Prof. Dr. Osman İsmail, Dr. Zehra Altın and Dr. M. Bora Akın for their time and valuable contributions in all stages of my career.

I would also like to thank my thesis committee members, Prof. Dr. Hüseyin Afşar and Prof. Dr. Güldem Üstün for their valuable advice and inputs.

I wish to thank Head of Chemical Engineering Department, Prof. Dr. Hanifi Saraç for his kindly consideration and support through writing of this thesis.

I would like to express my great appreciation to Prof. Dr. Mahmut D. Mat, who always accepted me as a member of his research group at Mechanical Engineering Department in Niğde University and spent a lot of time on my study. My thanks also go to all members of his research group, especially Çiğdem Timurkutluk, Tuğrul Y. Ertuğrul, Ali Çelen, Selahattin Çelik, Bora Timurkutluk, Adem Çiçek, Abdullah Mat, Fatma Aydın for sharing experimental set-up and helping on many tests.

I owe, of course, a great part of my success to Prof. Dr. Mogens Bjerg Mogensen, without whose care and guidance I might never have had a wonderful experience at Department of Energy Conversion and Storage in Technical University of Denmark. I also would like to thank all colleagues at Department of Energy Conversion and Storage for their assistance and discussions, especially Finn Willy Poulsen, Nikolaos Bonanos, Peter Holtappels, Jens F.S. Borchsenius, Jonathan Hallinder, Sandrine Ricote, Alberto Lapina.

Needless to say but I certainly must, I thank my best friends Izzy and Boğoçlu, with whom I have shared this entire experience. You make me a better person who looks to the future while still enjoying the present. To Palle, without whose support, care and help, I might never overcome the hard work in Denmark.

Last but not least, I thank my mother, Esincik, who lights up my life with her presence and smile. Without her love, I could not have begun or finished that study. To my father, Alp, I am ever grateful to him for being my hero. I am very proud to inherit the career in chemistry from my father. I have been missing you too much, Dad.

To my brother, Mengütay, is another part of me, my role model and superhero. I can not imagine a life without you.

September 2012

D. Berceste BEYRİBEY

TABLE OF CONTENTS

page

CHAPTER 1

CHAPTER 2

CHAPTER 3

CHAPTER 4

CHAPTER 5

CHAPTER 6

LIST OF SYMBOLS

pK_a	Acid Strength
ΔH	Enthalpy Change
T_c	Calcination Temperature
T_g	Glass Transition Temperature
i-V	Current-Voltage
i-P	Current-Power
pH_2O	Water Pressure
$T(H_2O)$	Water Temperature
R	Resistance
R_s	Serial Resistance
C	Capacitance
Q	Constant Phase Element
C_w	Equivalent Capacitance
n	Frequency Power
σ	Conductivity

LIST OF ABBREVIATIONS

AFC	Alkaline Fuel Cell
PEMFC	Proton Exchange Fuel Cell
PAFC	Phosphoric Acid Fuel Cell
MCFC	Molten Carbonate Fuel Cell
SOFC	Solid Oxide Fuel Cell
IT-SOFC	Intermediate Temperature Solid Acid Fuel Cell
SAFC	Solid Acid Fuel Cell (SAFC)
MIEC	Mixed Ionic and Electronic Conductor
SEM	Scanning Electron Microscopy
XRD	X-ray Diffraction
RT-XRD	Room Temperature X-ray Diffraction
HT-XRD	High Temperature X-ray Diffraction
EDS	Energy Dispersive X-ray Spectroscopy
TG	Thermogravimetry
DTA	Differential Thermal Analysis
DSC	Differential Scanning Calorimetry
EIS	Electrochemical Impedance Spectroscopy
OCV	Open Circuit Voltage
VMO	$V_xMo_{1-x}O_y$
CPE	Constant Phase Element
JCPDS	Joint Committee on Powder Diffraction Standards

LIST OF FIGURES

LIST OF TABLES

page

ABSTRACT

ADVANCED ELECTRODE/ELECTROLYTE MATERIALS FOR LOW AND INTERMEDIATE TEMPERATURE SOLID OXIDE FUEL CELLS

D. Berceste BEYRİBEY

Department of Chemical Engineering
A Dissertation

Supervisor: Prof. Dr. Seyfettin ERTURAN

In this thesis study, various advanced materials were synthesized and investigated as electrode and electrolyte for low and intermediate temperature solid oxide fuel cells (SOFCs). Molybdenum vanadium oxide ($V_{0.13}Mo_{0.87}O_{2.935}$) powder was obtained by a new method of reducing acidified vanadate and molybdate solution at 60 °C by passing hydrogen sulfide gas through the solution. The obtained mixed oxide was characterized by Scanning Electron Microscopy (SEM), X-ray Diffraction (XRD), Thermogravimetry (TG) and Differantial Thermal Analysis (DTA) and used as anode in a fuel cell for the first time in literature. Its electrochemical behaviour and performance in the solid oxide fuel cell were carried out using Electrochemical Impedance Spectroscopy (EIS) and Fuel Cell Test Station.

Three types of solid acids, rubidium phosphate tellurate, rubidium selenate with a secondary phase of rubidium hydroxide and cesium dihydrogen phosphate tellurite, were prepared and characterized by SEM, XRD, High Temperature X-ray Diffraction (HT-XRD), TG, DTA, Differential Scanning Calorimetry (DSC) and Energy Dispersive X-ray Spectroscopy (EDS) techniques. All solid acids were tested as electrolyte under various temperatures and atmospheres. Conductivity measurements were performed by EIS.

The results from the study showed that molybdenum vanadium oxide is a good candidate to be used as a mixed ionic and electronic conducting anode in intermediate temperature SOFCs. In addition, it is revealed that advanced solid acid materials have a potential to be used as electrolytes for low and intermediate temperature SOFCs.

Key words: Mixed ionic and electronic conductor, solid acid, electrolyte, electrode, low and intermediate temperature solid oxide fuel cells.

YILDIZ TECHNICAL UNIVERSITY

GRADUATE SCHOOL OF NATURAL AND APPLIED SCIENCES

ÖZET

DÜŞÜK VE ORTA SICAKLIK KATI OKSİT YAKIT PİLLERİ İÇİN YENİ ELEKTROT VE ELEKTROLİT MALZEMELERİ

D. Berceste BEYRİBEY

Kimya Mühendisliği Anabilim Dalı
Doktora Tezi

Danışman: Prof. Dr. Seyfettin ERTURAN

Bu tez çalışmasında, çeşitli gelişmiş malzemeler sentezlenmiş, düşük ve orta sıcaklık katı oksit yakıt pilleri için elektrot ve elektrolit malzemesi olarak incelenmişlerdir. Molibden vanadium oksit ($V_{0.13}Mo_{0.87}O_{2.935}$), yeni bir yöntem ile 60 °C'deki asitlendirilmiş vanadat-molibdat çözeltisinden hidrojen sülfür gazı geçirilmesi ile elde edilmiştir. Elde edilen karma oksit Taramalı Elektron Mikroskobu (SEM), X-ray Difraksiyonu (XRD), Termogravimetri (TG) ve Diferansiyel Termal Analiz (DTA) yöntemleri ile karakterize edilmiş ve literatürde ilk defa bir yakıt pilinde anot olarak kullanılmıştır. Katı oksit yakıt pillerindeki elektrokimyasal davranışı ve performansı Elektrokimyasal Empedans Spektroskopisi (EIS) ve Yakıt Pili Test Ünitesi kullanılarak belirlenmiştir.

Üç farklı katı asit (kuvvetli asitlerin alkali tuzları); rubidyum fosfat tellurat, rubidyum hidroksit safsızlığı içeren rubidyum selenate ve sezyum dihidrojen fosfat tellurit, hazırlanmış ve SEM, XRD, Yüksek Sıcaklık X-ray Difraksiyonu (HT-XRD), TG, DTA, Diferansiyel Taramalı Kalorimetri (DSC) ve Enerji Dağılımlı X-ray Spektoroskopi (EDS) yöntemleri ile karakterize edilmişlerdir. Tüm katı asitler elektrolit olarak farklı sıcaklık ve atmosferlerde test edilmişlerdir. İletkenlikleri, EIS kullanılarak belirlenmiştir.

Bu çalışmadaki sonuçlar, molibden vanadyum oksidin karma iyonik-elektronik iletken anot olarak orta sıcaklık kati oksit yakıt pillerinde kullanılmak için iyi bir aday olduğunu göstermektedir. Ayrıca, gelişmiş katı asit malzemelerin, düşük ve orta sıcaklık katı oksit yakıt pillerinde elektrolit olarak kullanılabileceğini de ortaya koymaktadır.

Anahtar Kelimeler: Karma iyonik-elektronik iletken, katı asit, elektrolit, elektrot, düşük ve orta sıcaklık katı oksit yakıt pilleri.

CHAPTER 1

INTRODUCTION

1.1 Literature Review

Fuel cells are electrochemical devices that convert chemical energy into electrical energy and some heat. Sir William Grove is known as the pioneer of the fuel cell technology and he discovered the basic operating principle of fuel cells by reversing water electrolysis to generate electricity from hydrogen and oxygen in 1839. However, fuel cells were forgotten until the middle of the 20th century and the first commercial use of fuel cells was in NASA space programs to generate power for space capsules. Since then, fuel cells have been used in many other applications such as transportation, stationary power and portable power systems.

Figure 1.1 illustrates a typical fuel cell system. In a typical fuel cell, gaseous fuel and an oxidant are fed continuously to the anode and cathode, respectively. An electric current is produced by the electrochemical reactions take place at the electrodes. Although the components and characteristics of a fuel cell are similar to those of a typical battery, the battery is an energy storage device and its maximum energy capacity is limited by the amount of the reactant stored within the battery itself. On the other hand, the fuel cell is an energy conversion device that theoretically has the capability of producing electrical energy for as long as the fuel and oxidant are supplied to the electrodes. In addition, on contrary to the conventional power generation methods, the fuel cells are not limited by thermodynamic limitations of heat engines such as the Carnot efficiency [1, 2].

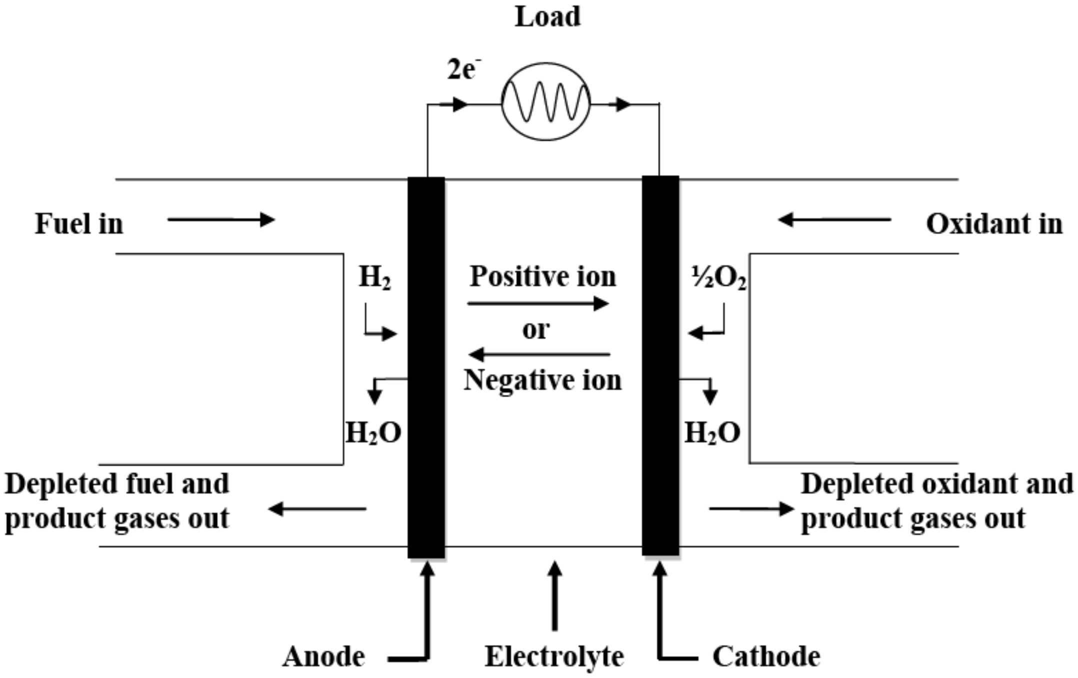

Figure 1.1 A typical fuel cell system

There are many types of fuel cells and the most common classification of fuel cells is by the type of electrolytes used in the cells:

- Alkaline fuel cell (AFC)
- Proton exchange fuel cell (PEMFC)
- Phosphoric acid fuel cell (PAFC)
- Molten carbonate fuel cell (MCFC)
- Solid oxide fuel cell (SOFC)
- Solid acid fuel cell (SAFC)

The choice of electrolyte dictates the operating temperature of the fuel cell. The physicochemical and thermo mechanical properties of materials used in the cell components depend on the operating temperature and useful life of a fuel cell. Table 1.1 lists types of fuel cells and their characteristics.

Table 1.1 Types of fuel cells and their characteristics

Fuel cell type	**Electrolyte**	**Charge carrier**	**Operating temperature**	**Fuel**
Alkaline FC (AFC)	KOH	OH^-	60-120 ºC	H_2
Proton exchange membrane FC (PEMFC)	Solid polymer	H^+	40-80 ºC	H_2
Phosphoric acid FC (PAFC)	Phosphoric acid	H^+	160-220 ºC	H_2
Molten carbonate FC (MCFC)	Lithium and potassium carbonate	CO_3^{2-}	600-700 ºC	H_2, CO, CH_4, other hydrocarbons
Solid oxide FC (SOFC)	Solid oxide electrolyte (yttria, zirconia)	O^{2-}	600-1000 ºC	H_2, CO, CH_4, other hydrocarbons
Solid acid FC (SAFC)	Solid acid electrolytes (CsH_2PO_4)	H^+	200-300 ºC	H_2

Aqueous electrolytes are limited to temperatures of about 200 ºC or lower because of their high vapor pressure and rapid degradation at higher temperatures. In low temperature fuel cells (AFCs, PEMFCs, PAFCs and SAFCs), only pure hydrogen can be used as fuel and all other fuels must be converted to hydrogen prior to entering to the fuel cell. The anode catalyst in low temperature fuel cells is strongly poisoned by unfavorable reactions of catalytic anode materials with sulfur and/or carbon species present in readily available hydrocarbon fuels resulting in performance loss and degradation of the anode. In addition to that, low operating temperatures provide an opportunity to low temperature fuel cells to be used for transport and portable power systems. In high temperature fuel cells (MCFCs and SOFCs), CO, CH_4 and other hydrocarbons can be internally converted to hydrogen or even directly oxidized. Due to their high operating temperatures, high temperature fuel cells have mainly been considered for large-scale stationary power generations. Their high electric efficiencies and fuel flexibilities are two major advantages of high temperature fuel cells over low temperature types [1, 2].

Alkaline Fuel Cell (AFC)

The electrodes are separated by a porous matrix saturated with an aqueous alkaline solution, such as potassium hydroxide (KOH). For low temperature application, concentrated KOH (35-50 wt. %) is used as the electrolyte [1]. Carbon dioxide (CO_2) poisons the AFCs through the conversion of KOH to potassium carbonate (K_2CO_3), which irreversibly blocks of the pores in the cathode and reduce the ionic conductivity of the electrolyte. Because of this fact, the main disadvantage of AFCs is the requirement to be operated under pure oxygen or at least purified air.

Proton Exchange Fuel Cell (PEMFC)

The electrolyte in PEMFCs is a proton conductor membrane, commonly fluorinated sulfonic acid polymer. Corrosion problems are minimal in this fuel cell due to the water is only liquid phase formed. However, the membrane needs to be hydrated for efficient performance and this problem restricts the operating temperature ($\leq$ 100 ºC) of PEMFCs.

Phosphoric Acid Fuel Cell (PAFC)

The phosphoric acid fuel cell is the first fuel cell technology to be commercialized [2]. The electrolyte in PAFCs is concentrated phosphoric acid and this fuel cell operates at 160-220 ºC due to poor ionic conductivity of the electrolyte at lower temperatures. The electrocatalyst in both the anode and cathode is platinum and it can be easily poisoned by adsorption of CO and/or sulfur impurities on the active sites.

Molten Carbonate Fuel Cell (MCFC)

In MCFCs, a combination of alkali (generally K, Li) carbonates is used as the electrolyte. The alkali carbonates form a highly conductive molten salt at 600-700 ºC and carbonate ions provide ionic conductivity. Although MCFCs do not require an external fuel reformer due to their high operating temperature, the corrosive electrolyte causes breakdown and corrosion of the components. At high operating temperatures in MCFCs, nickel anode and nickel oxide cathode are adequate to promote reactions [2].

Solid Oxide Fuel Cell (SOFC)

A solid oxide fuel cell consists of an anode and cathode, separated by an electrolyte layer, which allows the transfer of oxygen anions (O^{2-}), formed at the cathode, and prevents the exchange of electrons. Ionically (O^{2-}) conducting solid oxides, such as yttria stabilized zirconia (YSZ), is used as the electrolyte. Air is fed to cathode as the oxidant and oxygen from air is reduced at the cathode, when fuel is oxidized at the anode. Advantages of SOFCs are high efficiency, long-term stability, fuel flexibility, low emission and relatively low cost. The main disadvantage is long start-up times and mechanical and chemical compatibility issues due to their high operating temperatures.

More economical component materials can be applied to SOFC systems operating at intermediate temperatures (typically 700-850 ºC), which are known as intermediate temperature solid oxide fuel cells (IT-SOFCs) [3]. The lower operating temperature would solve various problems associated with the high temperature operation, such as densification of electrodes, formation of an insulating layer at the electrode/electrolyte interface by inter diffusion, and crack formation from stress caused by large differences in the thermal expansion coefficients of the cell components [4]. However, one of the major challenges for IT-SOFCs is anode poisoning by unfavorable reaction of anode material with impurities in hydrocarbon fuels, such as sulfur and carbon species.

Sulfur Poisoning of SOFC Anodes

Many economically available fuel sources (syngas, natural gas, diesel etc.) include impurities such as sulfur species. Table 1.2 shows the typical composition and H_2S concentrations of some fuel sources [3]. Hydrogen sulfide (H_2S) is the most common impurity in these fuels [5] and recognized as a problem in operating IT-SOFCs with the conventional anodes such as $Ni/Y_2O_3ZrO_2$ (Ni/YSZ), which is poisoned by H_2S rapidly and loss its activity for the electrochemical oxidation of hydrogen [6]. Even low H_2S concentrations cause irreversible sulfur poisoning for IT-SOFC, whereas the performance degradation can be reversible for SOFCs operating at high temperatures (>900 ºC). The possible reactions for sulfur-poisoning degradation mechanism of

Ni-based SOFC anode can be summarized as [3]:

$$H_2S(g) \leftrightarrow HS_{ads} + H(g/ads) \leftrightarrow S_{ads} + H_2(g/ads) \quad (1.1)$$

$$Ni + H_2S \leftrightarrow NiS + H_2 \quad (1.2)$$

$$3Ni + x\,H_2S \leftrightarrow Ni_3S_x + x\,H_2 \quad (1.3)$$

As given above, Ni can react with H_2S include chemisorptions (1.1) and sulfidation (1.2 and 1.3) according to different concentration. Another possible reaction is physical adsorption of H_2S on nickel.

Although, desulfurization pretreatment of fuel is available for SOFCs, overall system cost can be reduced by developing sulfur tolerant anode materials and cell integrity can be ensured in case of desulfurization system fault. Therefore, the major technical challenge in IT-SOFCs for H_2S-containing fuels is to develop alternative anode materials that are both chemically and electrochemically stable, and catalytically active in H_2S-rich environments for low operating temperatures [6, 7].

Table 1.2 Typical composition and H_2S concentration of some fuel sources [3]

Fuel type	**Typical composition**	**H_2S concentration**
Coal syngas	H_2, CO, CO_2, H_2O, N_2	100-300 ppm
Biogas	H_2, CO, CO_2, CH_4, H_2O, N_2	50-200 ppm
Natural gas	H_2, CO_2, N_2, C_2H_6, CH_4	> 1%

Sulfur Tolerant Anode Materials for SOFCs

Sulfur tolerant anode materials can be summarized in three main groups:

- Thiospinels and metal sulfides
- Metal cermets
- Mixed ionic and electronic conductors (MIECs)

Thiospinels are sulfide minerals with a general formula AB_2X_4 where A is a nominally +2 metal, B is +3 metal and X is -2 sulfide or similar anion (selenide or telluride).

Thiospinels and metal sulfides have good conductivity and show both catalytic activity toward H_2S oxidation and stability in H_2S-rich environments. However, their potential stability and catalytic activity under conventional fuels limit composite sulfide applications in SOFC systems.

Sulfur tolerant metal cermets with a sulfidation resistance up to a thousand ppm of H_2S can be achieved by modification of traditional Ni-YSZ in two ways: a partial or total substitution of Ni with more sulfur tolerant materials in Ni-YSZ and/or a replacement of YSZ by electrolyte material with higher ionic conductivity and stability during H_2S-containing fuels [3].

Mixed ionic and electronic conductors are good candidates for fuel cell anodes due to their both ionic and electronic conductivity. These materials are usually chemically stable in SOFCs at the elevated operating temperatures and their electronic and ionic conductivities can be easily modified by changing their stoichiometry or addition of dopants. Compared with metal-based anodes, transition metal oxide with mixed ionic and electronic conductivity are less likely to suffer from sulfur poisoning. All these desirable properties make MIECs attractive anode materials to be used in IT-SOFCs under sulfur-containing fuels.

Various MIECs have been tested for SOFCs as alternative sulfur-tolerant anodes, such as $La_{0.4}Sr_{0.6}TiO_{3\pm\delta}$-$Y_{0.2}Ce_{0.8}O_{2-\delta}$ (LST-YDC) [8], $La_{0.75}Sr_{0.25}Cr_{0.5}Mn_{0.5}O_{3\pm\delta}$ (LSCM55) [9], $Ce_{0.9}Sr_{0.1}Cr_{0.5}Fe_{0.5}O_{3\pm\delta}$ (CSCrF) [10], $Ce_{0.9}Sr_{0.1}VO_x$ (CSV) [11] and $Co_{0.5}Fe_{0.5}$+$Sm_{0.2}Ce_{0.8}O_{1.9}$ (SDC) [12]. Kurokawa et al. [13] investigated Y-doped $SrTiO_3$ (SYTO)-YSZ infiltrated with ceria and Ru for 10-40 ppm H_2S fuel streams. They achieved a constant maximum power density of 470 mW cm^{-2} in 10 ppm H_2S-containing H_2 and a sulfur tolerance much higher than that of traditional Ni-YSZ anodes. On the other hand, Li et al. [14] obtained only 135 mW cm^{-2} stable power density with undoped $BaTiO_3$ anode in 0.5% H_2S-CH_4 at 900 ºC. Lu et al. [15] and Zhu et al. [16] achieved good sulfur tolerant using Pd-impregnated SYT/LDC ($Sr_{0.88}Y_{0.08}TiO_{3-\delta}$/$La_{0.4}Ce_{0.6}O_{1.8}$) and Y-doped $La_{0.7}Sr_{0.3}CrO_{3-\delta}$ anodes, respectively. No decay in performance was seen for Pd-impregnated SYT/LDC anode in H_2 containing up to 50 ppm H_2S. Lohsoontorn et al. [17] showed that the gas composition and temperature have a significant impact on the interaction of sulfur with nickel-gadolinium-doped ceria (Ni-CGO).

Solid Acid Fuel Cell (SAFC)

Solid acid fuel cells utilize an anhydrous, nonpolymeric proton-conducting (solid acid) electrolyte that can operate at slightly elevated temperatures. Solid acids are chemical intermediates between normal salts and normal acids. Physically, the materials are similar to salts. At low temperatures, they have ordered structures. At higher temperatures, however, some solid acids undergo transitions to highly disordered structures that can exhibit anhydrous proton transport. Unlike the polymers in PEMFCs, proton conduction in oxyanion solid acids does not rely on the migration of hydronium ions. Haile and co-workers have showed solid acid proton conductors can be used in both H_2/O_2 and direct methanol fuel cells [18, 19]. Using supported thin CsH_2PO_4 electrolyte membranes on porous stainless steel gas-diffusion electrodes, peak power densities as high as 415 mW cm^{-2} were obtained [20].

Comparing with the traditional PEMFCs, SAFCs can reduce or eliminate the precious metal loadings due to their relatively high operating temperatures. These temperatures additionally imply a high tolerance of the catalysts to poisons, particularly CO, in the fuel stream. Unlike hydrated sulphonated polymers such as Nafion, no water molecules are required to facilitate proton transport in the solid acids, eliminating the need for continuous humidification of reactant gases. Furthermore, anhydrous proton transport eliminates the need for auxiliary humidification equipment and impermeability of the solid acid materials provides measurably higher open circuit voltages. While these many features render solid acids very attractive as fuel cell electrolytes several challenges must be overcame before solid acid based fuel cells can be commercially viable. Prominent amongst these is the water solubility of all known solid acids with high conductivity, which requires the implementation of engineering designs to prevent condensed water from contacting the electrolyte, particularly during fuel cell shutdown [21–23].

Solid Acid Electrolytes

Proton conductivity in the solid acid compounds (*e.g.*, sulphates, selenates and phosphates) arises upon a structural phase transformation at elevated temperature. These transitions create dynamical disorder in the H-bonded XO_4 network (where X= S, Se, P), enabling fast transport of protons mediated by rapid reorientations of the XO_4

tetrahedra (Grotthuss mechanism). The main inorganic acids used in the solid acids are given in Table 1.3.

Table 1.3 The main inorganic acids used in the solid acid electrolytes

Inorganic acids	**Molecular Formula**	**Molecular structure**	**pKa values**
Sulfuric acid	H_2SO_4	Tetrahedral 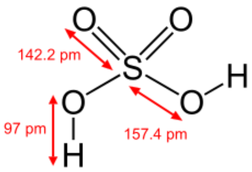 	pKa_1 = -3.0 pKa_2 = 1.92
Selenic acid	H_2SeO_4	Tetrahedral 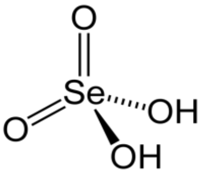 	Similar values with H_2SO_4
Phosphoric acid	H_3PO_4	Tetrahedral 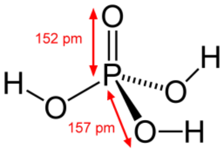 	pKa_1 = 2.15 pKa_2 = 7.20 pKa_3 = 12.37
Arsenic acid	H_3AsO_4	Tetrahedral 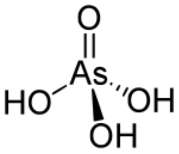 	pKa_1 = 2.19 pKa_2 = 6.94 pKa_3 = 11.5

The dynamic disordering of the hydrogen bond network leads to a dramatic increase in proton conductivity by several orders of magnitude. The transition is called superprotonic phase transition. The proton conductivity at the superprotonic phase transition increases abruptly by several orders of magnitudes and may reach the values up to 10^{-3}–10^{-2} S cm^{-1}[21, 23]. Table 1.4 represents conductivity and phase transition temperature of various solid acids.

Table 1.4 Conductivity and phase transition temperature of various solid acids

Compound	**Superprotonic phase transition temperature (°C)**	**Conductivity ($S\ cm^{-1}$)**	**Reference**
CsH_2PO_4	231	$\sim 2.0 \cdot 10^{-2}$	[21]
$KH(PO_3H)$	140	$4.2 \cdot 10^{-3}$	[24]
$CsH(PO_3H)$	160	$\sim 5.0 \cdot 10^{-3}$	[24, 25]
$Cs_3H(SeO_4)_2$	183	$\sim 10^{-3}$	[26]
β-$Cs_3(HSO_4)_3(H_x(P,S)O_4)$	125	$6 \cdot 10^{-3}$	[27]
$CsHSO_4$	141	$8 \cdot 10^{-3}$	[28]
$RbHSO_4$	160-170	$\sim 10^{-4}$	[28]
$KH(PO_3H)$-SiO_2	140	$1.15 \cdot 10^{-3}$	[23]
$Rb_{1.12}(NH_4)_{0.88}SO_4.Te(OH)_6$	209	$3 \cdot 10^{-2}$	[29]
$(NH_4)_2SeO_4 \cdot Te(OH)_6$	170	$2 \cdot 10^{-2}$	[30]
$Rb_2(SO_4)_{0.5}(SeO_4)_{0.5}Te(OH)_6$	227	$8 \cdot 10^{-2}$	[31]
$Rb_2SeO_4 \cdot Te(OH)_6$	217	$3.13 \cdot 10^{-3}$	[32]
$K_2(SO_4)_{0.9}(SeO_4)_{0.1} \cdot Te(OH)_6$	207	$5 \cdot 10^{-3}$	[33]

The solid acids with stoichiometry $MHXO_4$, $M_3H(XO_4)_2$, M_2HYO_4, or some variation thereof, are used as superprotonic solid acid electrolytes, where M = alkali metal or NH_4; X = S, Se; and Y = P, As. However, implementation of superprotonic solid acids in fuel cells is hindered by a poor chemical and mechanical stability. The alkali–metal hydrogen sulphates and selenates decompose in hydrogen containing atmospheres, whereas their dihydrogen phosphate counterparts need significant levels of humidification; for example, up to water vapour pressure of 0.30 atm for CsH_2PO_4, to keep their superprotonic properties.

Cesium dihydrogen phosphate (CsH_2PO_4) has been the best superprotonic solid acids known to date. Figure 1.2 illustrates the CsH_2PO_4 stability phase diagram [34].

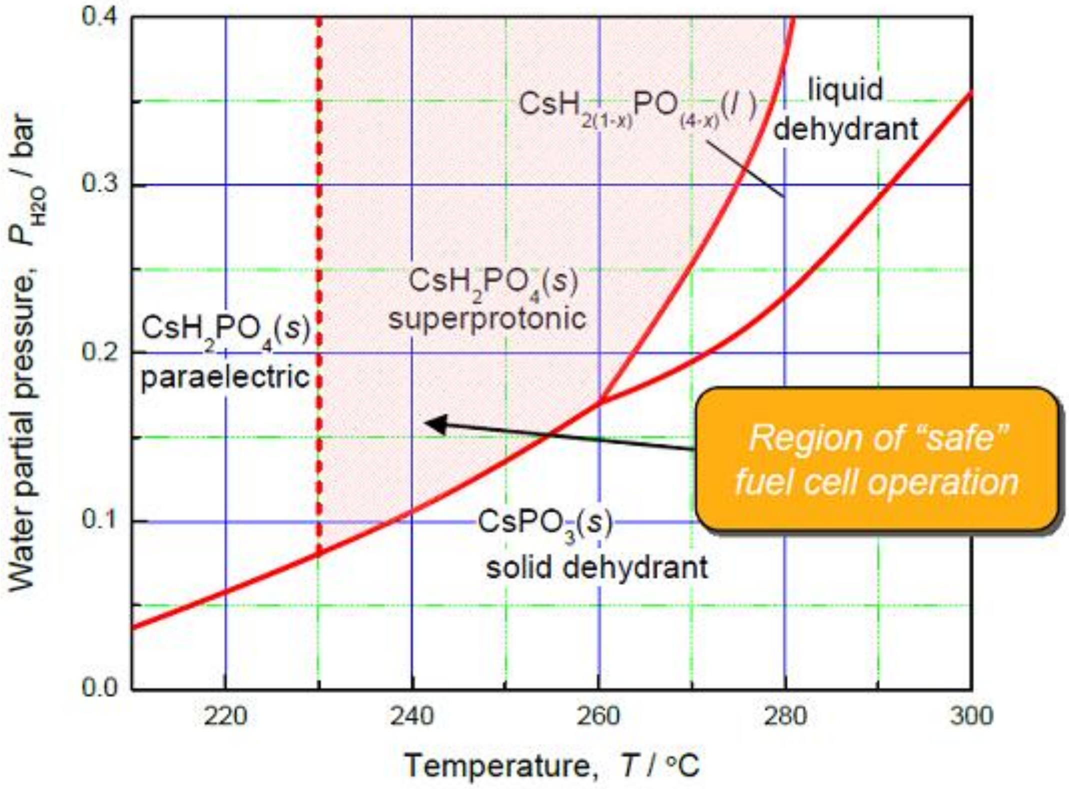

Figure 1.2 The stability phase diagram of CsH_2PO_4 [34]

The increase in the conductivity in solid acid electrolytes is still a dispute. Some researchers attributed the increase in the conductivity to water loss in the material caused by a thermal decomposition reaction where the generated water is responsible for the mobility of protons through the electrolyte material [22, 35]. The solid acid electrolytes decompose by the thermal dehydration through the following chemical reaction (1.4):

$$nXH_2PO_4(s) \rightarrow X_nH_2P_nO_{3n+1}(s) + (n-1)H_2O(v) \quad (1.4)$$

where *n* is the number of molecules present in stoichiometric equation, the letter 's' and 'v' enclosed in parenthesis denotes that the corresponding compound is in the solid or vapor state.

The other researchers attribute this increase in the conductivity to a phase transition to a high temperature stable superprotonic phase [22]. In that case, the oxyanions acquire higher rotational freedom in the crystal lattice. This leads to a disorder in the hydrogen bonding between the oxyanion groups and allows more combinations of possible hydrogen bond due to the lattice rearrangement. A fraction of the possible hydrogen bonds is occupied enabling the protons to move among the proton vacancies of the lattice (hopping). This conduction mechanism is known as 'Grotthuss mechanism'. Grotthuss mechanism is separated from the vehicle mechanism due to proton hopping provides the conduction between oxyanions rather than a proton solvent [35]. Figure 1.3 shows the Grotthuss conduction mechanism.

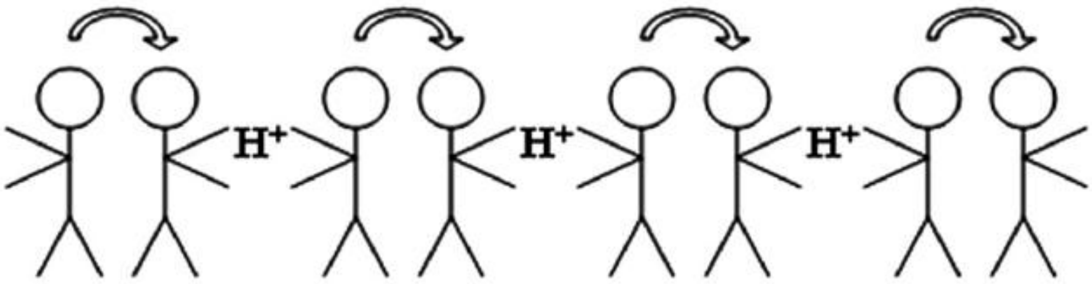

Figure 1.3 Grotthuss conduction mechanism [36]

1.2 Aim of Thesis

Solid oxide fuel cells are promising candidate for future energy conversion systems because they have higher energy conversion efficiency than conventional heat engine systems and other types of fuel cells. Capability of SOFC to use conventional fosil fuels with multiple compositions is essential for commercialization of SOFCs.

Low and intermediate temperature SOFCs have received more attention recently due to the less severe requirements for materials compatibilities at higher temperature. As a result, reducing the SOFC operating temperature may greatly lower fabrication and material cost. Since sulfur tolerance of traditional Ni-YSZ anodes drown drastically at lower temperatures, alternative sulfur tolerant anodes are need to allow the direct use of practical fuels, without the need for extensive reforming and fuel conditioning.

Another issue to be overcome in the field of low temperature SOFCs is the necessity of proton solid electrolytes operating at 160-500 ºC. Recently, solid acid electrolytes such as CsH_2PO_4 has been gained attention for applications at elevated temperatures up to 300 ºC due to their high conductivity and being not affected by humid atmospheres compared with polymer electrolytes require humid conditions.

The aim of this thesis study is to develop and examine the properties of some advanced materials as electrode and electrolyte for low temperature SOFCs.

1.3 Objectives

The specific thesis objectives are:

1. To prepare and characterize molybdenum vanadium oxide and study its anodic properties in solid oxide fuel cells.

2. To examine effects of the operation parameters, such as temperature, flow rate of fuel and sulfur contamination, on the cell performance.

3. To prepare and characterize solid acid materials (rubidium dihydrogen phosphate tellurate, rubidium selenate with a second phase of rubidium hydroxide and cesium dihydrogen phosphate tellurite) as electrolytes for low temperature SOFCs.

4. To investigate the effects of various parameters (temperature, humidification and test atmospheres) on the protonic conductivity of the synthesized solid acid electrolytes.

CHAPTER 2

VANADIUM MOLYBDENUM OXIDE

In this chapter, $V_{0.1}Mo_{0.87}O_{2.935}$ powder was obtained by reducing acidified vanadate and molybdate solution at 60 ºC by passing hydrogen sulfide gas through the solution. The obtained mixed ionic-electronic conductor oxide was used as an anode material in SOFCs for the first time in literature and its electrochemical performance was tested at various operation temperatures for intermediate temperature solid oxide fuel cell (IT-SOFC) under pure and 50 ppm H_2S containing hydrogen fuel. The highest cell performance of 0.18 W cm^{-2} peak power was reached at an operation temperature of 750 ºC for dry H_2. It was found that the addition of 50 ppm H_2S to the anode gas caused a 22 % decrease in the cell peak power. The loss in the cell performance was attributed to both gas conversion and diffusion. Short-term regeneration tests indicated that 1 hour-exposure to sulfur free gas was insufficient for the reactivation of the cell performance.

2.1 Introduction

Intermediate temperature solid oxide fuel cells (IT-SOFCs) are promising energy conversion and generating system due to their comparative advantages such as high efficiency, low pollution, system compactness and flexibility of fuel selection. Unfortunately, anodes in IT-SOFCs are easily poisoned by the impurities in the gas streams, such as sulfur commonly present in natural gas [5, 9]. Hydrogen sulfide (H_2S) is the most common impurity in these fuels [5] and recognized as a problem in operating IT-SOFCs with the conventional anodes such as $Ni/Y_2O_3ZrO_2$ (Ni/YSZ), which is poisoned by H_2S rapidly and loss its activity for the electrochemical oxidation of hydrogen [6]. Therefore, the major technical challenge in IT-SOFCs for H_2S-

containing fuels is to develop alternative anode materials that are both chemically and electrochemically stable, and catalytically active in H_2S-rich environments [6, 7].

Various Ni-free materials have been tested for SOFCS as alternative sulfur-tolerant anodes [6, 8-12]. However, the most of these materials were found deactivated in H_2S-containing fuels and the contents of various S species on the surface. Eventually, none of them provides all criteria that are required for a successful and effective anode with low polarization resistance and acceptable long-term stability [7].

On the other hand, mixed ionic and electronic conductors are of great interest for their high catalytic and electrochemical properties. These metastable structures often demonstrate new or enhanced properties compared to their thermodynamically stable forms [36-38]. The requirement of multiple preparation steps for synthesis is one of the most important challenges of mixed oxide catalysts [39]. These materials can often be prepared at low temperatures by electrochemical intercalation, inorganic ion exchange, or organic precursor methods [40]. The composition of the oxide elements affects the catalytic performance of mixed oxide materials. Schur et al. [41] reported that the structure and performance of mixed metal oxide catalysts depends on each step of the preparation method. It is rather difficult and demanding to isolate the effects of each preparation parameter upon the structural and performance changes of the resulting catalysts [39]. The preferred preparation method for an effective mixed metal oxide catalyst includes the intimate mixing of all starting chemicals to form a precursor solution [42]. Many researchers in catalysis field have still studied on characterization the active phases or structures of the catalysts and correlation of these active phases or structures with the catalytic performance.

Vanadium-molybdenum oxides have been frequently used in heterogeneous oxidation catalysis due to their high surface acidity. These catalysts have found a wide application in selective partial oxidation, such as benzene to maleic anhydride [43, 44], acrolein to acrylic acid [45], crotonaldehyde to maleic anhydride [43]. The similarity of ionic radius and the structures in the highest oxidation state of V_2O_5 and MoO_3 provides a unique interaction between these materials. These similarities enable the formation of substitutional solid solutions with structures, which may be interpreted as a shear structure of ReO_3 lattice with different oxidation states of cations [46]. As compared to molybdenum and vanadium binary oxide, the particular hexagonal structure of

$V_{0.13}Mo_{0.87}O_{2.935}$ has attracted attention due to its potential applications as a catalyst or molecular sieve. The ternary oxide of $V_{0.13}Mo_{0.87}O_{2.935}$ possesses a complex tunnel structure along the crystallographic c direction. In this structure, the molybdate and vanadate framework consists of zigzag chains of edge-shared octahedral parallel to the c axis; these chains share octahedral corners to create one-dimensional channels [47].

Previously, $V_{0.13}Mo_{0.87}O_{2.935}$ was obtained by complete dehydration from the protonic form $H_{0.13}V_{0.13}Mo_{0.87}O_3{\cdot}nH_2O$ [40, 48]. This protonic form was synthesized using two different approaches. The first approach consists of the synthesis of an intermediary brannerite-type phase $LiVMoO_6$ by $LiVO_3$ and MoO_3 solid-state reaction. In a second approach, lithiated mixed vanadium-molybdenum oxide hydrates isotypic with hexagonal MoO_3 structure are synthesized by dissolution of V_2O_5 and MoO_3 in LiOH aqueous solution or by dissolution of $LiVO_3$ and $Li_2Mo_2O_7$ in water. Afterwards, Dupont et al. [49] reported a new way of obtaining not only the pure protonic hexagonal MoO_3 type oxide hydrate with the ratio V/Mo=0.13/0.87 but also $H_xV_xMo_{1-x}O_3{\cdot}nH_2O$ phases family with $0.06 \leq x \leq 0.18$. The synthesis method consists of the dissolution of metallic molybdenum and V_2O_5 in hydrogen peroxide solution. Then, the solution is heated until a yellow precipitate (the precursor) appears.

In this part of the study, a new synthesis method of the pure hexagonal $V_{0.13}Mo_{0.87}O_{2.935}$ is reported. This method is based on reducing acidified vanadate and molybdate solution at 60 ºC by passing hydrogen sulfide gas through the solution. Then, the performance and sulfur tolerance of $V_xMo_{(1-x)}O_y$ in IT-SOFCs as an alternative anode material are reported.

2.2 Experimental

2.2.1 Synthesis and Characterization

0.009 mol ammonium heptamolybdate tetrahydrate ($(NH_4)_6Mo_7O_{24}$ * 4 H_2O) (Merck) and 0.001 mol ammonium monovanadate (NH_4VO_3) (Merck) were dissolved in deionized water (1 liter). Concentrated hydrochloric acid (37%, Sigma-Aldrich) was added to the solution for adjusting the pH to the value of ≤ 1. The solution was then transferred to the two-necked bottle and heated to 60 °C with stirring (Yellowline, MSC basic C) for two hours. $V_xMo_{1-x}O_y$ particles (VMO) were synthesized by passing hydrogen sulfide (H_2S) gas through the solution into the reaction bottle during four hours. The resultant solids were collected by centrifugation (Nüve, NF615), washed several times with deionized water and acetone and then dried in air at 50℃ overnight.

Scanning electron microscopy (SEM) was carried out by Zeiss Evo 60. X-ray diffraction (XRD) data were recorded at room temperature using Stoe Theta-Theta XRD (40 kV, 30 mA, Cu $K\alpha_1$) and analyzed using the STOE Win XPOW 2.20 program. Termogravimetry (TG) and differential thermal analysis (DTA) were carried out using Perkin Elmer TG/DTA-6300 and Netzsch STA 409 CD instruments. Thermal analysis experiment was performed in air (50 ml min^{-1}) with a heating rate of 5 ºC min^{-1}. The measurements were done in the temperature range of room temperature to 700 an 1100 ºC. Samples were grounded with an agate mortar prior the measurements.

2.2.2 Electrolyte Fabrication

YSZ ($(Y_2O_3)_{0.08}(ZrO_2)_{0.92}$) and ScSZ ($(ZrO_2)_{0.90}(Sc_2O_3)_{0.10}$) electrolytes were produced by tape casting**.** Commercial electrolyte powders (YSZ and ScSZ) (Nextech Materials) was mixed with an organic dispersant and solvent, respectively. After ball milling around 24 h, certain amount of plasticizer and binder were added. The mixture was ball milled again for another 24 h. Then the slurry was tape cast with a blade gap of 170 µm. Six tapes of electrolyte were stacked together and laminated isostatically under 40 MPa pressure for 10 minutes. The laminates were then cut into circle (38 mm in diameter) for YSZ electrolyte and square (79 mm x 79 mm) for ScSZ electrolyte using a laser cutter. The sintering of the electrolyte was performed at two stages. In the first stage, the electrolyte was heated to 1000 °C and held for 2 h. In the second stage, the electrolyte was sintered at 1400 ºC for 4 h. The thickness of the electrolytes was measured as 150 µm after sintering whereas the outer dimensions were reduced to 30 mm in diameter for YSZ and 60 mm x 60 mm for ScSZ.

2.2.3 Cell Preparation

LSCF ($(La_{0.60}Sr_{0.40})(Co_{0.20}Fe_{0.80})O_{3-\delta}$) (Nextech Materials) powder was used as the cathode material. LSCF powders were initially mixed with ethyl cellulose and terpineol at proper ratios (50 wt.% solid loading) to prepare a cathode screen printing paste. After ball milling about 12 h, the cathode paste was screen-printed on the both YSZ and ScSZ electrolytes. The sintering of the cathode was achieved at 1050 ºC for 2 hours. The anode screen printing paste was prepared similarly and screen-printed on the other side of the electrolytes symmetric to the cathode. The anode layers printed on YSZ and ScSZ electrolytes were sintered at 850 ºC for 2 h and 650 ºC for 2.5 h, respectively. Then, two cells were ready for testing. The active area of the cells was 1 cm^2 with YSZ electrolyte (Cell A) and 16 cm^2 (4 cm x 4 cm) with ScSZ electrolyte (Cell B).

2.2.4 Cell Testing

The single cells was placed between two stainless steel interconnectors with nickel foam and stainless steel mesh which were respectively used as anode and cathode current collectors. The details of the short stack configuration can be found elsewhere [50-52].

2.2.4.1 The Cell A

Figure 2.1 illustrates the anode and cathode surfaces of the produced single cell (VMO/YSZ/LSCF) with 1 cm^2 active area. Ag paste was applied as a current collector and the single cell was placed between two stainless steel interconnectors (Figure 2.2) for the performance tests. The experiments were conducted in the temperature range of 700-800 ºC for the Cell A. After the temperature was stable, dry hydrogen ($pH_2O<0.001$ bar) with the rate of 1.0 L min^{-1} were introduced to anode side of the single cell while ambient air was used as oxidant at the cathode side. Current and power densities of the Cell A were obtained using a fuel cell test station (Arbin Instruments FCTS, TX, USA) (Figure 2.3) which has a temperature controlled furnace with a push rod pressing capability to improve the contact between the cell and interconnectors. Scanning electron microscopy, on the other hand, was through Carl Zeiss Evo 40.

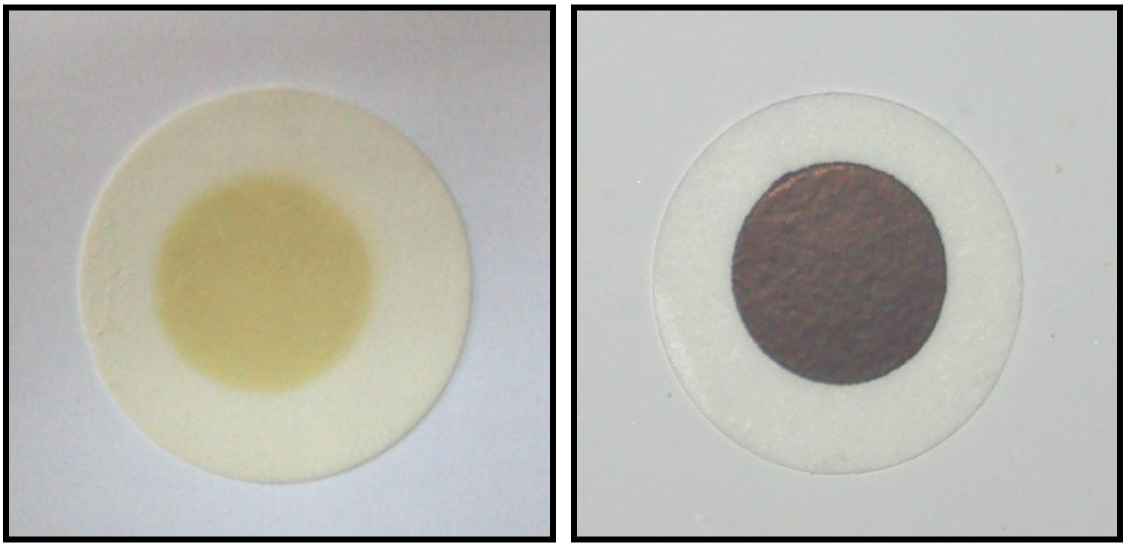

(a) (b)

Figure 2.1 The (a) anode and (b) cathode surface of the produced Cell A (VMO/YSZ/LSCF) with 1 cm^2 active area

Figure 2.2 The stainless steel interconnectors used in the tests of the Cell A

Figure 2.3 The fuel cell test station

2.2.4.2 The Cell B

Figure 2.4 shows the anode and cathode surfaces of the produced single cell (VMO/ScSZ/LSCF) with 16 cm^2 active area. No paste was applied as a current collector and the single cell was placed between two stainless steel interconnectors for the performance tests (Figure 2.5). All experiments were conducted in the temperature range of 650-750 ºC for the Cell B. After temperature was stable, various flow rates of hydrogen between 0.5-2.0 L min^{-1} were introduced to anode side of the single cell while ambient air was used as oxidant at the cathode side. The measurements were performed under dry hydrogen ($pH_2O<0.001$ bar) and dry hydrogen containing 50 ppm hydrogen sulfide. Performance curves were obtained using a fuel cell test station (Arbin Instruments FCTS, TX, USA) (Figure 2.3).

Electrochemical impedance spectra were recorded under fuel cell test environment using a Parstat 2273 frequency response analyzer. Impedance measurements were carried out over the frequency range of 100 kHz to 0.01 Hz under open circuit voltage (OCV). Data analysis was done using the software *ZSimpWin 3.21*, supplied by Princeton Applied Research. Scanning electron microscopy was through Carl Zeiss Evo 40.

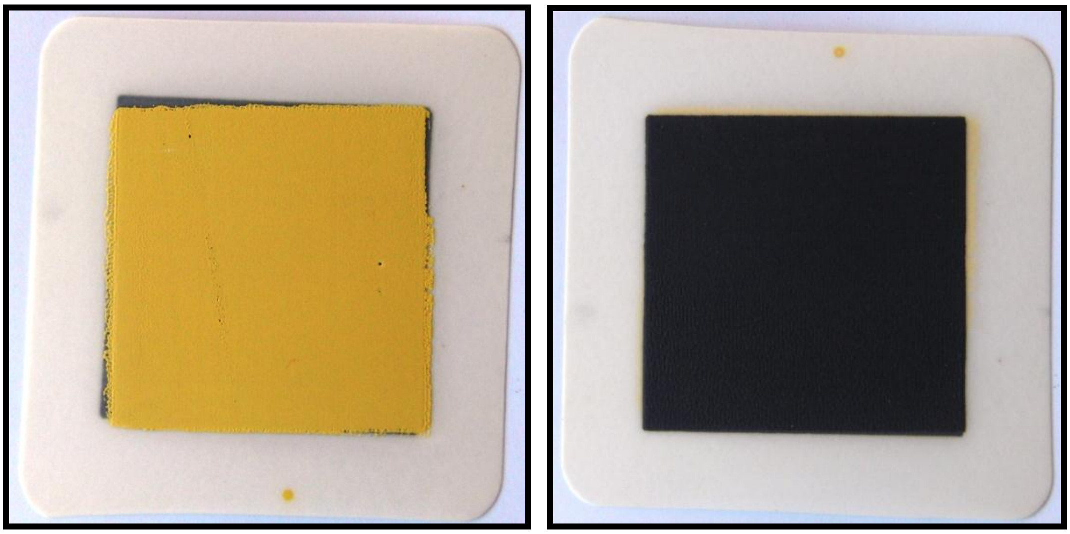

(a) (b)

Figure 2.4 The (a) anode and (b) cathode surface of the produced Cell B (VMO/ScSZ/LSCF) with 16 cm^2 active area

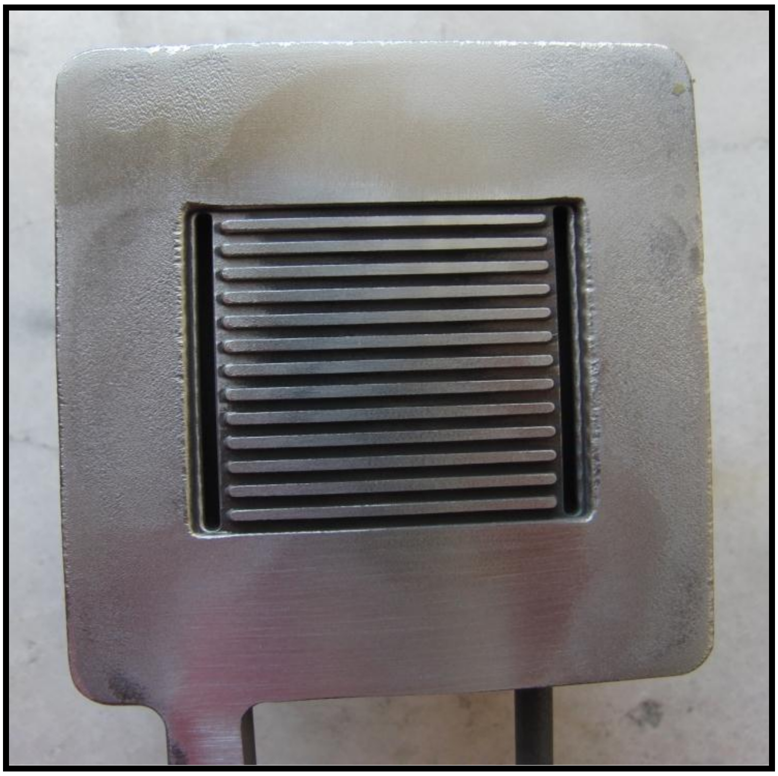

Figure 2.5 The stainless steel interconnectors used in the tests of the Cell B

2.3 Results and Discussions

2.3.1 Structural and Thermal Analysis

SEM micrograph was taken in order to determine the crystalline size and morphology. The morphology of $V_{0.13}Mo_{0.87}O_{2.935}$ powder is shown in Figure 2.6. Synthesis resulted in $V_{0.13}Mo_{0.87}O_{2.935}$ particles with diameters in the range of about 200 nm to 2-3 μm.

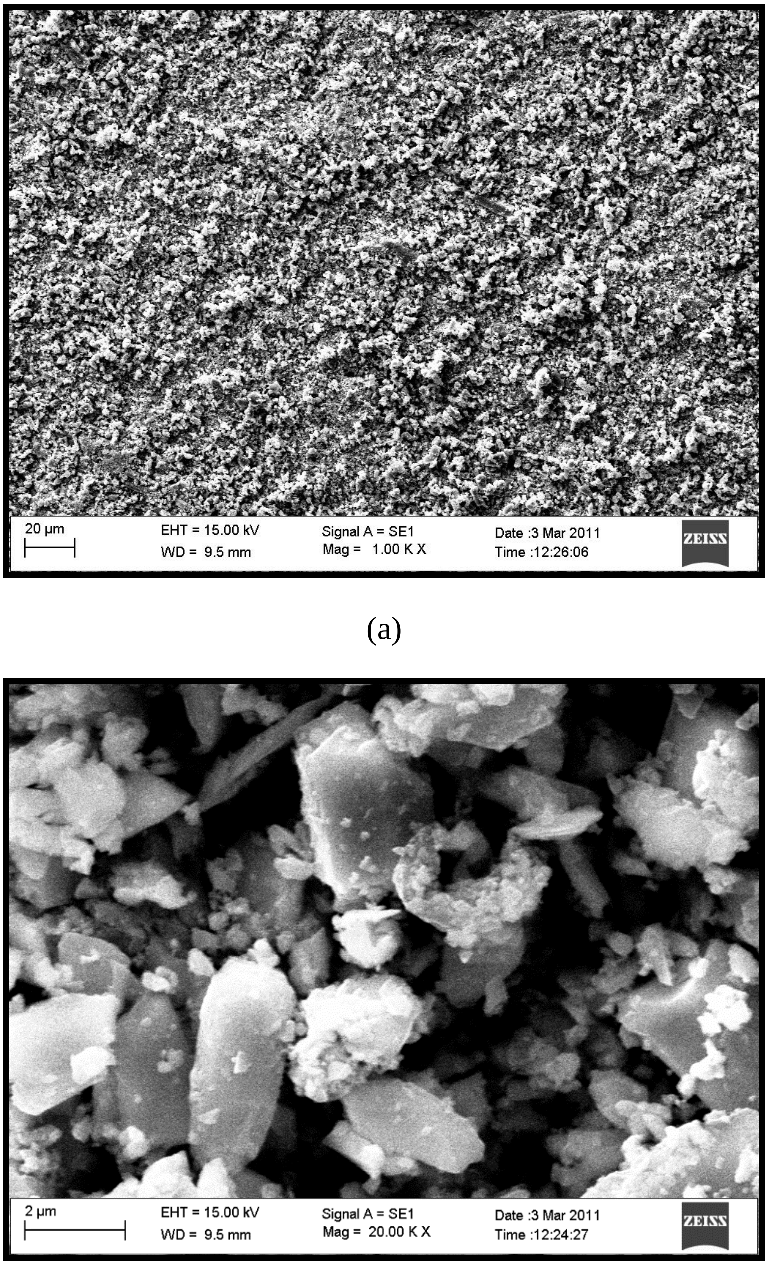

(a)

(b)

Figure 2.6. The SEM image of synthesized $V_{0.13}Mo_{0.87}O_{2.935}$ powder; (a) 1000 X, (b) 20000 X

In order to investigate the thermal stability of the $V_{0.13}Mo_{0.87}O_{2.935}$ powder, thermal analysis (TG and DTA) were conducted. Figure 2.7 shows the TG and DTA curves of $V_{0.13}Mo_{0.87}O_{2.935}$ from room temperature to 700 ºC. As shown in Figure 2.7 (a), approximately 9 wt.% weight loss was observed in the range of 30-420 °C due to the eliminating of adsorbed sulfur and remained ammonium groups as NH_3 and/or NO_x. Some unreacted ammonium heptamolybdate and ammonium monovanadate are responsible of the remained volatiles.

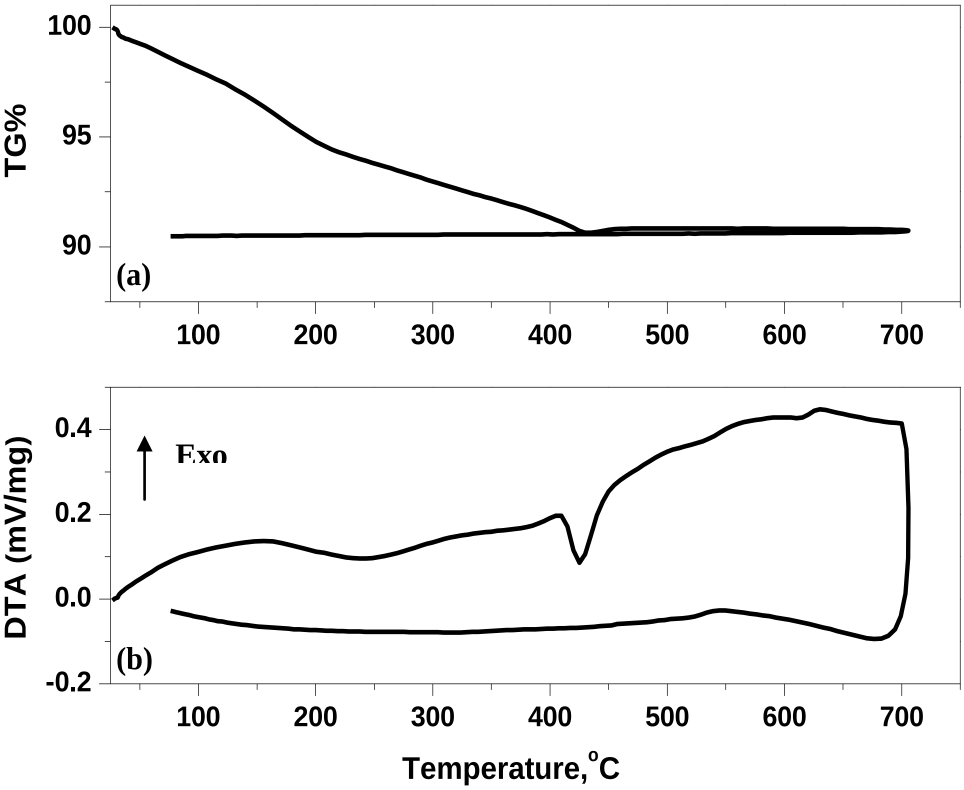

Figure 2.7 (a) TG and (b) DTA analysis of synthesized $V_{0.13}Mo_{0.87}O_{2.935}$ powder up to 700 ºC

In the DTA measurement seen in Figure 2.7 (b), the main features of the DTA trace for the reaction in air were a large exotherm (peak maximum 150 °C) attributed to reaction of adsorbed sulfur with oxygen, a large endoterm (peak maximum 245 °C) due to the eliminating the volatile compounds and a sharp endotherm at 430 °C representing phase transformation. While cooling from a maximum temperature of 700 °C, no reverse is seen in Figure 2.4 (b). This phase transition temperature is lower than the previously reported values of 460 °C [48] and 480 °C [49]. Dupont et al. [49] showed that hexagonal $V_{0.13}Mo_{0.87}O_{2.935}$ is stable up to 480 °C and above this temperature, this solid is irreversibly transformed into a stable orthorhombic mixed oxide, isotypic to a-MoO_3, which retains the same V/Mo = 0.13/0.87 ratio. Therefore when calcined at Tc = 400 °C, these Mo, V mixed phases could be transformed into orthorhombic $V_{0.13}Mo_{0.87}O_{2.925}$. Moreover, Dupont et al. [49] reported that the heating of the orthorhombic $V_{0.13}Mo_{0.87}O_{2.925}$ around 600 °C induces the formation of a liquid phase and a solid phase chemical composition. In contrast to their results, no evidence was found for the formation of a liquid phase in our experiments.

Because of no decomposition was seen up to 700 °C, a second thermal analysis was done up to 1100 °C to determine the decomposition temperature of the mixed oxide, as given in Figure 2.8. Another mass loss with a value of 15 wt.% is attributed to the sublimation of MoO_3 formed by segregation of $V_{0.13}Mo_{0.87}O_{2.935}$ (between 750-795 °C). As seen in Figure 2.8, DTA profile of the compound represents a large exothermic effect upon heating from room temperature to 750 °C. The reaction of adsorbed sulfur with oxygen and segregation of $V_{0.13}Mo_{0.87}O_{2.935}$ might be responsible of that exothermic effect. The segregation of $V_{0.13}Mo_{0.87}O_{2.935}$ (above 600 °C) is given with the following reaction [37, 49]:

$$V_{0.13}Mo_{0.87}O_{2.935} \rightarrow V_2MoO_8\text{- type phase} + MoO_3 \qquad (2.1)$$

At higher temperatures, sublimation of MoO_3, which has a sublimation temperature of 795 °C [53], occurs and the mass loss reaches at 100 wt.% by the temperature of 830 °C.

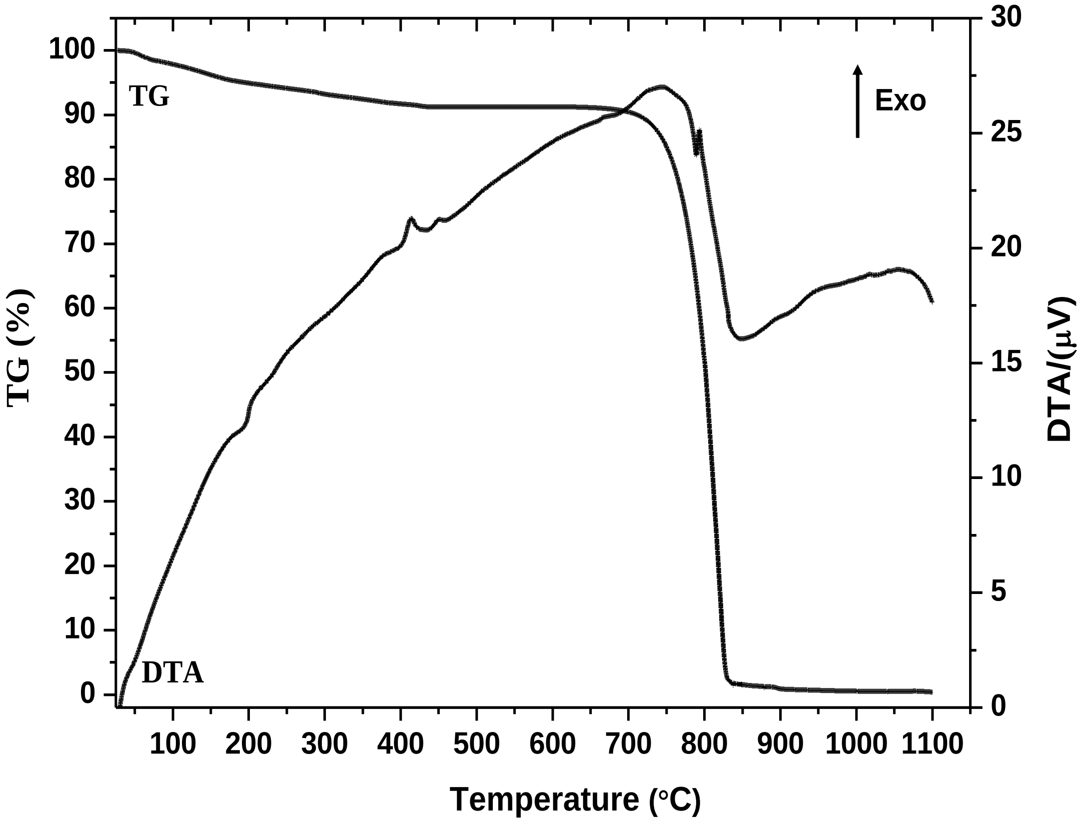

Figure 2.8 Thermal analyses (TG and DTA) of the synthesized $V_{0.13}Mo_{0.87}O_{2.935}$ powder up to 1100 ºC

Figure 2.9 demonstrates the XRD pattern of synthesized powder, which are in good agreement with hexagonal $V_{0.13}Mo_{0.87}O_{2.935}$ phase with lattice parameters of a= b= 10.59 Å and c= 3.69 Å (# 48-0766 in the JCPDS database, space group *P6₃*). The XRD pattern demonstrated a high degree of crystalline material. No other phases were detected.

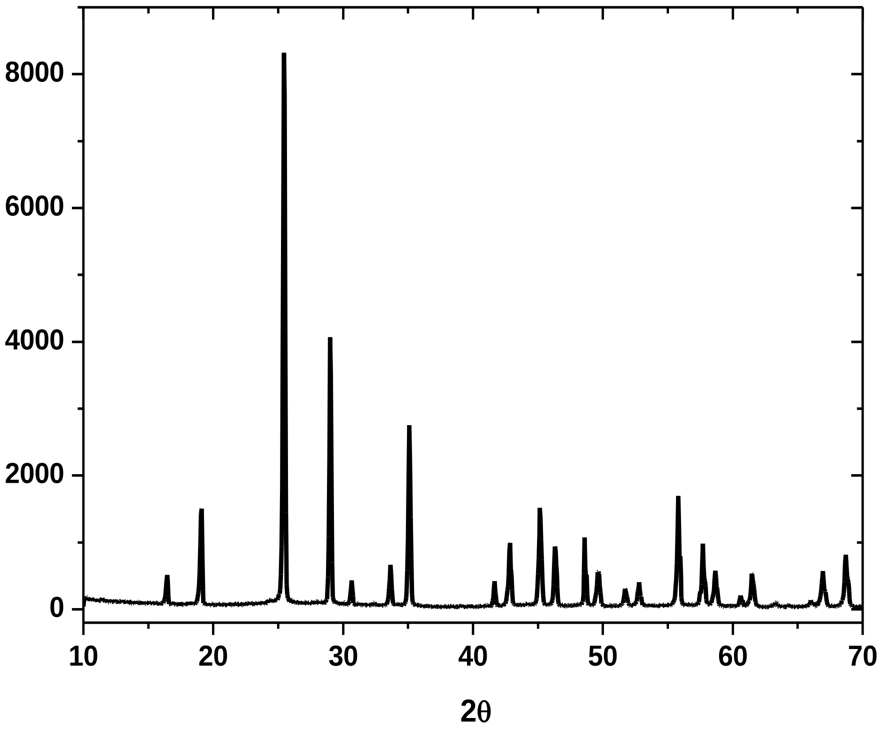

Figure 2.9 XRD pattern of synthesized $V_{0.13}Mo_{0.87}O_{2.935}$ powder

2.3.2 Cell Testing

2.3.2.1 The Cell A

Performance Tests

To determine the catalytic activity of $V_{0.13}Mo_{0.87}O_{2.935}$ as anode material, it was tested in the cell for the temperatures of 700, 750 and 800 °C. The effect of temperature on the current density and the power is given in Table 2.1. As it is seen in Table 2.1, current density and power increases by increasing temperature. 0.38 ± 0.06 A cm^2 current density and 0.18 ± 0.03 W power was obtained at 800 °C in the cell.

Table 2.1 The effect of temperature on the current density and the power of the cell

Operating temperature (°C)	**Current density (A/cm^2)**	**Power density (W/cm^2)**
700	0.20 ± 0.02	0.10 ± 0.01
750	0.32 ± 0.05	0.16 ± 0.02
800	0.38 ± 0.06	0.18 ± 0.03

The effect of temperature on OCV is shown in Figure 2.10. The results showed that OCV values of the cell are close to the theoretical value.

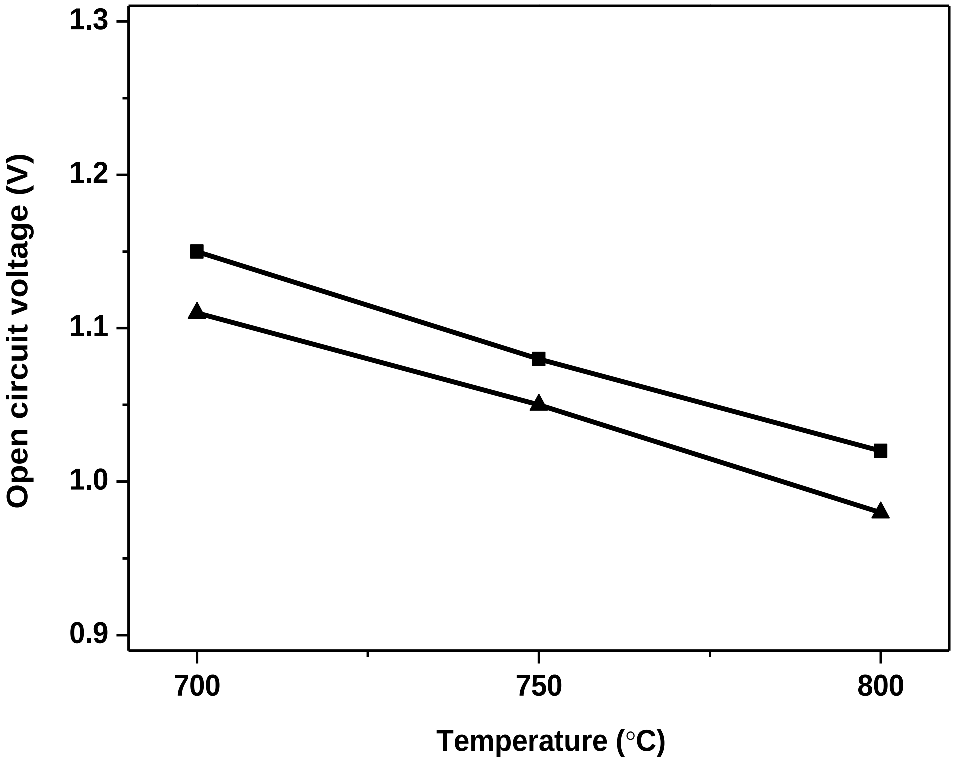

Figure 2.10 The OCV values of the cell versus the operating temperature

Surface Analysis

Figure 2.11 denotes the details of the pre-tested and post-tested anode surface, while Figure 2.12 shows the microstructure of the cross section of the pre-tested and post-tested cell. As seen in Figure 2.11, the anode possesses porous structure (Figure 2.11 (a)) whereas the YSZ electrolyte is seen to be uniform, continuous and dense (Figure 2.12 (a)). It seems VMO anode is stable under dry hydrogen and no remarkable deformation is seen between the anode and the electrolyte (Figure 2.12 (b)). On the other hand, it is obvious that nano-sized VMO particles grow under reducing atmosphere (Figure 2.11 (b)) and reaches to micro-scale. Characteristic needle structure of $V_{0.13}Mo_{0.87}O_{2.935}$ particles can be easily seen in Figure 2.11 (b).

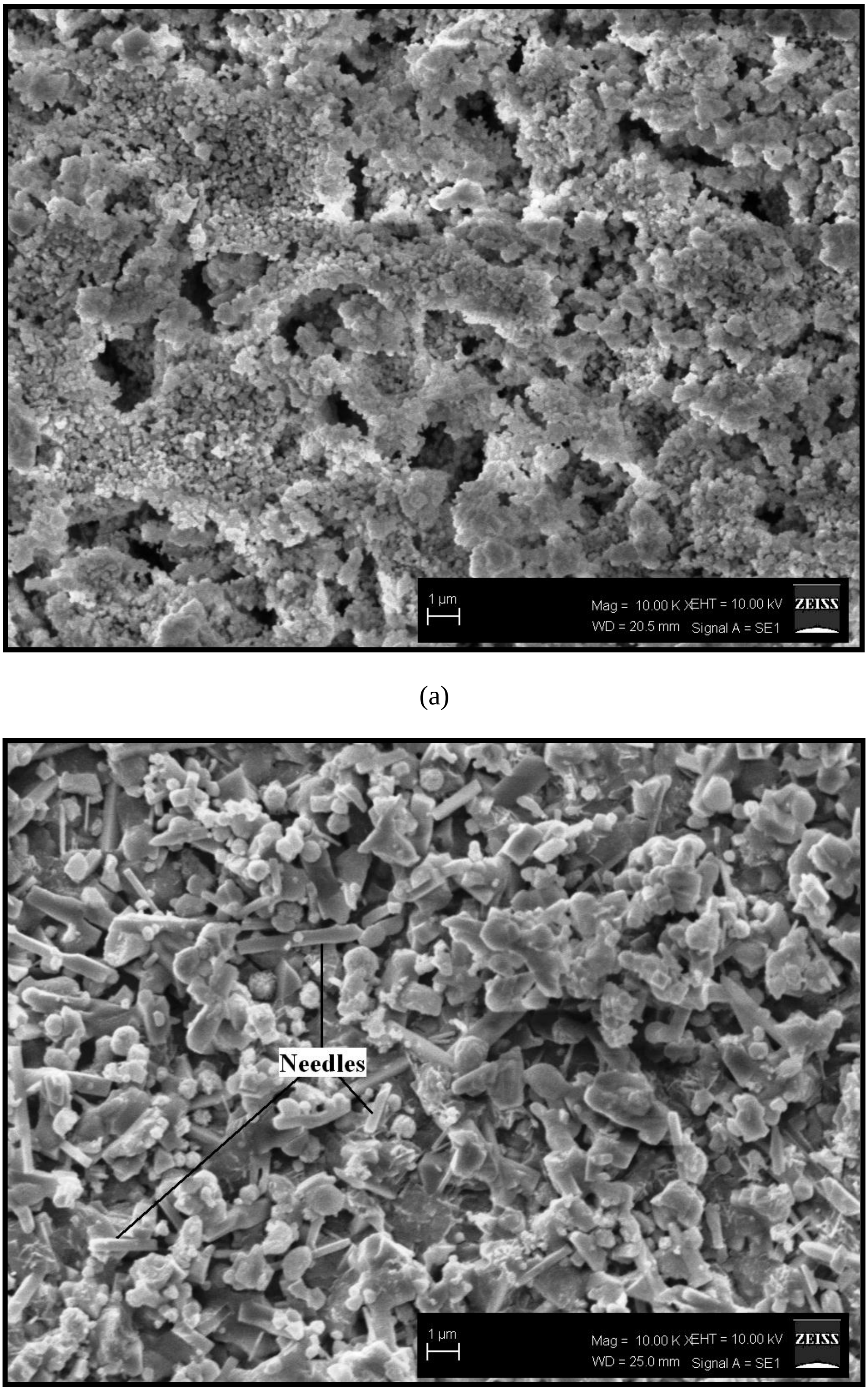

(a)

(b)

Figure 2.11 SEM images of the (a) pre-tested and (b) post-tested anode surface (10000X)

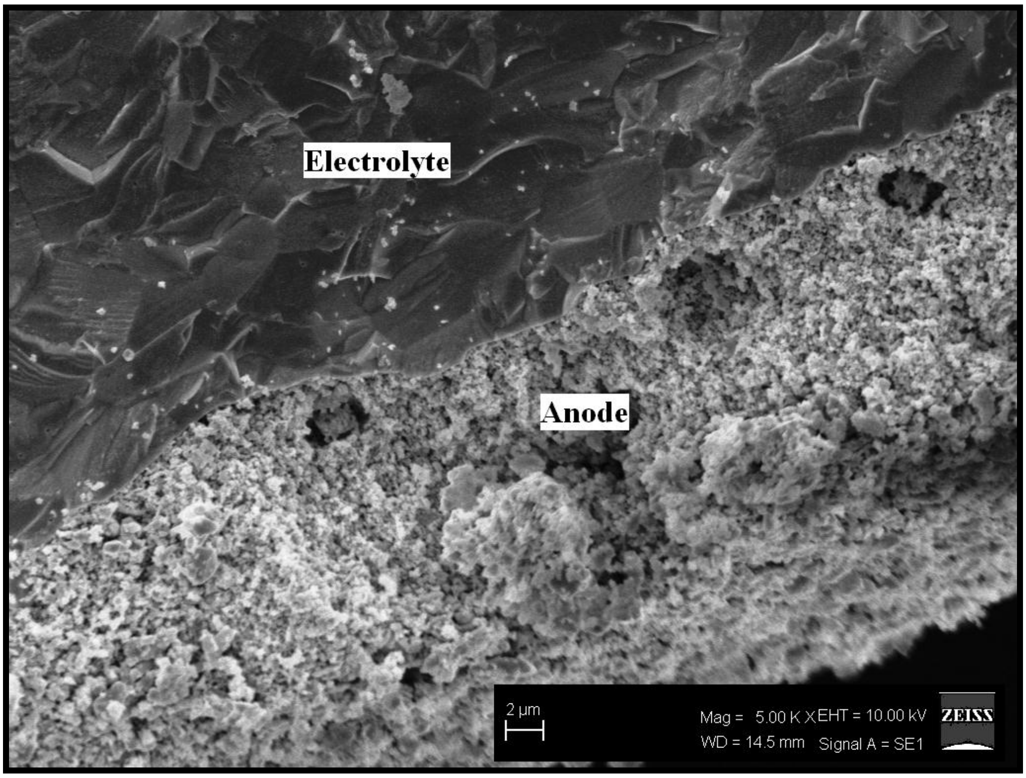

(a)

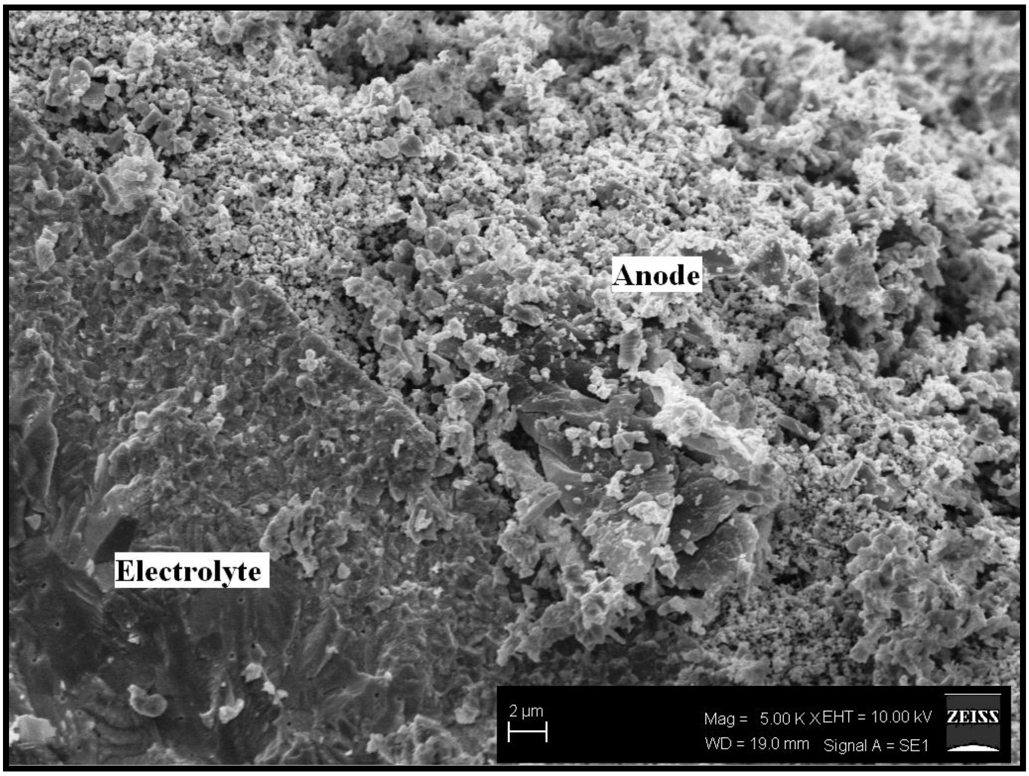

(b)

Figure 2.12 SEM images of the cross section of the (a) pre-tested and (b) post-tested cell (5000X)

Several parameters influence the physicochemical as well as the catalytic properties of the mixed oxides. The nature and crystallinity of phases and the surface composition of the synthesized catalyst depend on the temperature of calcination (T_c). Therefore, even though the cell showed relatively lower current density and power, it is possible to enhance the performance of the cell by changing the calcination medium of the metal oxide or firing temperature of the cell as it was presented in the literature [50, 51]. It is obvious that $V_xMo_{(1-x)}O_y$ can be used as anode materials in solid oxide fuel cells.

2.3.2.2 The Cell B

Performance Tests

Figures 2.13-2.15 show the cell voltage and power density as a function of the current density at operation temperatures of 650, 700 and 750 °C for various dry hydrogen flow rates, respectively. It is seen that the cell performance tends to increase with increasing the hydrogen flow rate at all temperatures as expected. However, the effect of the hydrogen flow rate on the cell performance is extremely significant at 650 °C operation temperature (Figure 2.13), comparing with that at higher operation temperatures can be seen at 700 and 750 °C operation temperatures (Figure 2.14 and Figure 2.15). It seems concentration polarization is extremely effective limiting the cell performance at 650 °C operation temperature. Concentration polarization mainly dominates at low voltage regions (≤0.4 V) and as seen in Figure 2.13, it surprisingly limits the cell performance at about 0.8 V in 0.5 L min^{-1} H_2 flow. By increasing the hydrogen flow rate, the cell performance enhances due to the decrease in the ohmic polarization while the concentration polarization still limits the cell performance at high voltages.

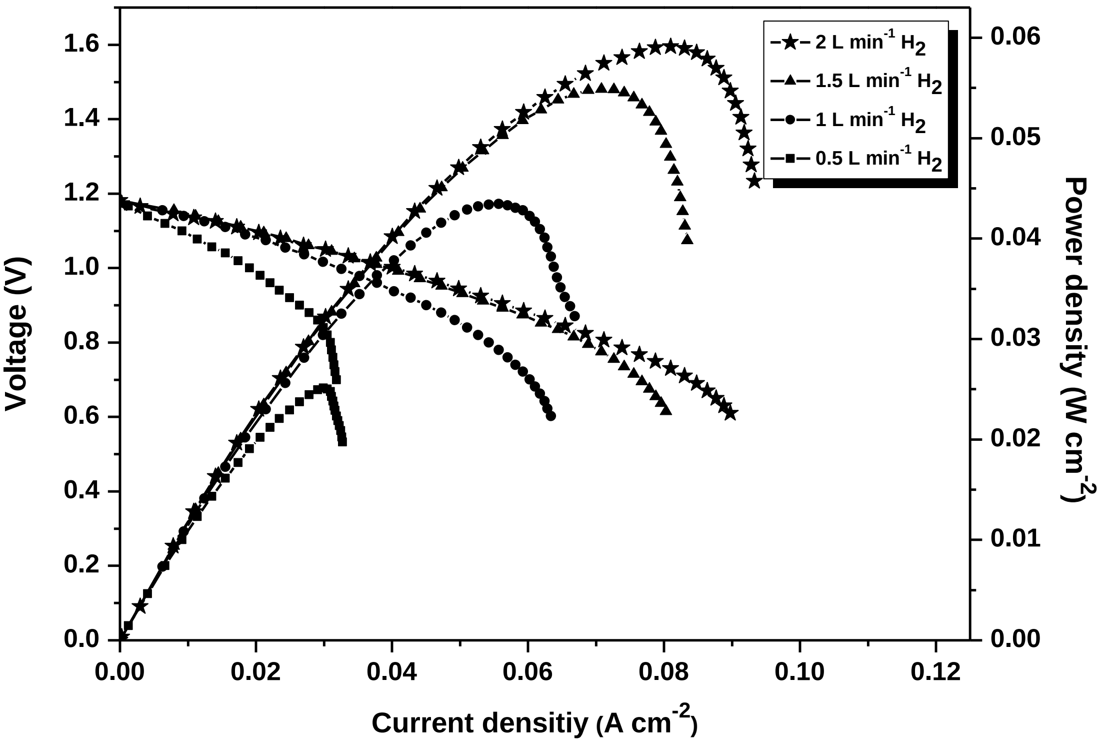

Figure 2.13 The voltage and power density output versus the current density under various flow rates of dry H_2; *T*= 650 °C

The single cell exhibited almost 1 W (~0.06 W cm^{-2}) maximum power output at 650 °C operation temperature when the hydrogen flow rate was set to the maximum (2 L min^{-1}). Similar behaviour can be seen at 700 and 750 °C operation temperatures Figure 2.14 and Figure 2.15. The highest cell performance was obtained at maximum hydrogen flow rate at both operation temperatures. The cell provides 1.76 W (~0.11 W cm^{-2}) and 2.88 W (0.18 W cm^{-2}) peak power at 700 °C and 750 °C, respectively. Moreover, concentration polarization finally dominates to limit the cell performance at low voltage region (~0.4 V) at 750 °C operation temperature. Furthermore, at all operation temperatures considered, the open circuit potential was around 1.17 V which was very close to the theoretical one indicating that the electrolyte is fully dense.

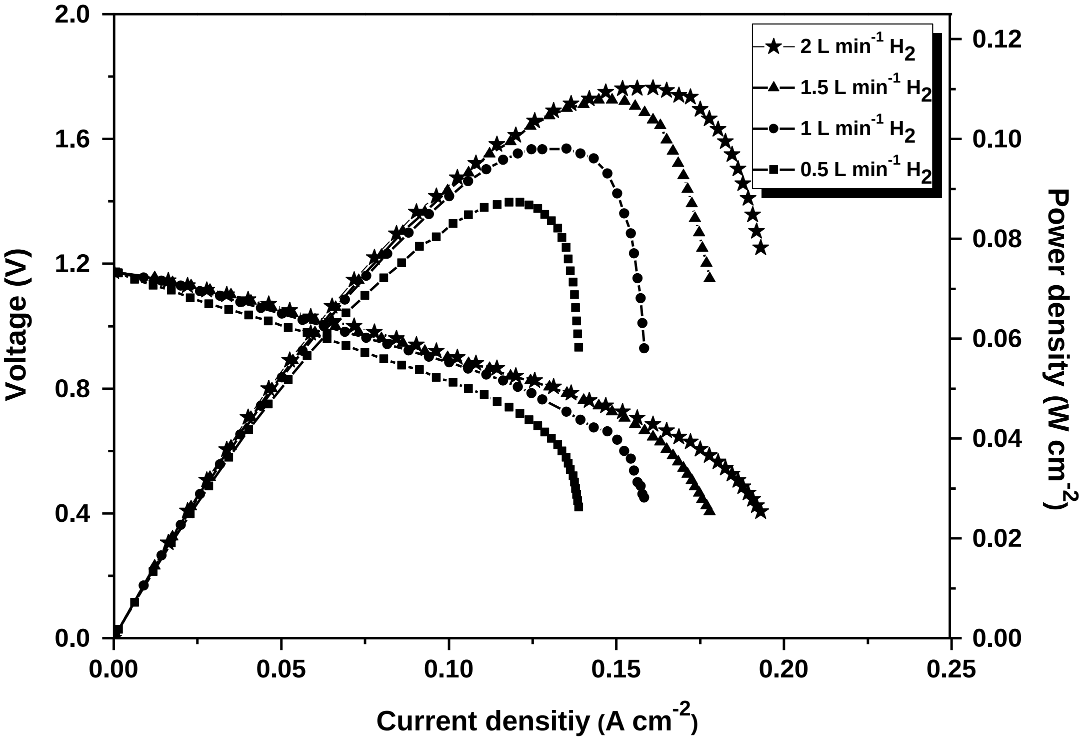

Figure 2.14 The voltage and power density output versus the current density under various flow rates of dry H_2; T= 700 ºC

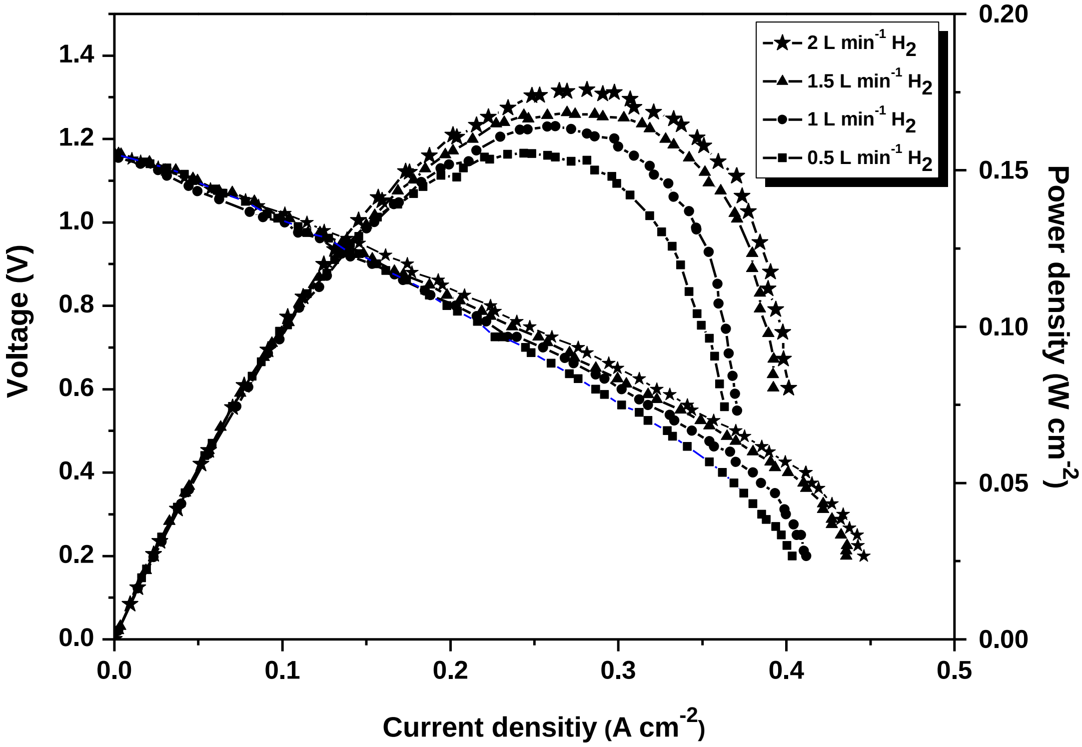

Figure 2.15 The voltage and power density output versus the current density under various flow rates of dry H_2; T= 750 ºC

Figure 2.16 shows the cell voltage and power density as a function of the current density at an operation temperature of 750 ºC in dry H_2 and 50 ppm H_2S-containing dry H_2 with a flow rate of 2 L min^{-1}. The cell was first stabilized in pure hydrogen gas until a steady open circuit potential was observed. Then the current-voltage (*i-V*) and the current-power (*i-P*) curves were recorded under both dry H_2 and 50 ppm H_2S-containing dry H_2 to figure out the effect of H_2S on the cell performance. The results show that 50 ppm H_2S contamination causes a 22 % decrease in the peak power density from 0.18 W cm^{-2} to 0.14 W cm^{-2} at 750 ºC. Pillai et al. [54] tested a solid oxide fuel cell with Ni-YSZ anode supported on $Sr_{0.8}La_{0.2}TiO_3$ in H_2 containing 100 ppm H_2S and observed a 20 % decrease in the peak power density at 800 ºC. In a similar study, Kurokawa et al. [13] found ca. a 10 % decrease in the power density at 800 ºC, testing a SOFC with a Y-doped $SrTiO_3$ anode in 10 ppm H_2S-containing H_2. These results are comparable with our observation on the cell performance under H_2S-containing H_2.

After switching to sulfur-free gas (pure H_2) for 1 hour, no reactivation of the cell was obtained. This means that the presence of 50 ppm H_2S in H_2 fuel degrades the performance of $V_xMo_{(1-x)}O_y$ anode at 750 ºC and the degradation can not be recovered by a short-term exposure to sulfur-free fuel gas. Zhang et al. [55] reported that even 5 ppm H_2S-containing H_2 fuel causes an unrecoverable degradation for Ni/YSZ anode, after treated under pure H_2 in a period of 2 h. On the other hand, Rasmussen et al. [56] found that for Ni/YSZ anodes which were subjected to 2 ppm H_2S-containing H_2 fuel, the recovery takes ~250 h, while Lohsoontorn et al. [17] showed 25 h-recovering time is necessary for Ni/GDC anodes after exposed to 1 ppm H_2S-containing H_2.

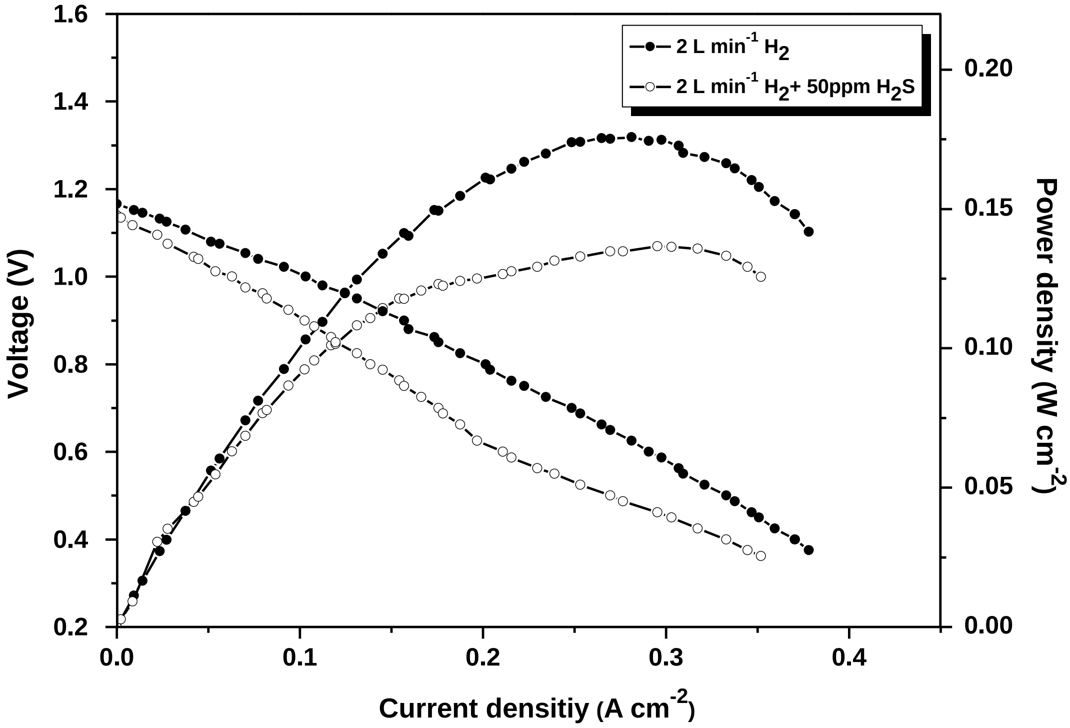

Figure 2.16 The voltage and power density output versus the current density under flowing dry H_2 and 50 ppm H_2S-containing dry H_2. *T*= 750ºC

Electrochemical Impedance Spectroscopy

All EIS data represented in this paper were fitted to equivalent circuit model consisting of serially coupled $(RQ)^{\gamma}$ elements. The spectra was treated with as few $(RQ)^{\gamma}$ elements as possible. The general model is shown in Figure 2.17. Similar models were used in the literature for comparable systems [51, 57, 58].

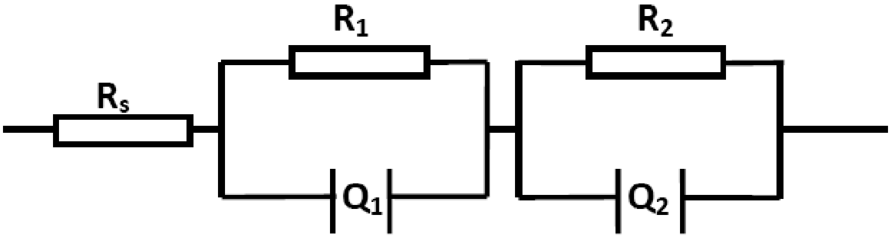

Figure 2.17 Equivalent circuit model used fit the impedance spectra

Figure 2.18 denotes the measured resistances as function of the operation temperature in dry H_2 and it is seen that total resistivity of the single cell decreases with increasing temperature as expected. The model used to fit the impedance data is also shown in Figure 2.18. The serial resistance, R_s, arises mainly from the ionic conductivity of the electrolyte if the specific electronic conductivity of the electrode material is much higher than the specific ionic conductivity of the electrolyte [59]. The electrode response at higher frequencies is referred to as Arc 1, and its resistance and capacitance is denoted R_1 and C_1. Arc 1 probably relates ion transfer impedance at between the electrolyte and the electrode [59]. The low frequency response is referred to as Arc 2, which can be related to either gas diffusion or gas conversion [57], and its resistance, and capacitance is denoted R_2 and C_2. The fitted parameters from impedance measurements of the cell with $V_xMo_{(1-x)}O_y$ anode are given in Table 2.2. Arc 2 is perfectly fitted with an n-value of unity indicates a process behaving like an ideal capacitor in parallel with a resistor at 650 and 700 ºC. However, it became depressed at 750 ºC. Arc 2 has a rather large capacitance (C_2) of about 8-12 F cm^{-2} at 650 and 700 ºC, while it suddenly decreased to 0.55 F cm^{-2} at 750 ºC. This amount of decrease in capacitance may be attributed to the completion of the segregation of the anode material at about 750 ºC (Figure 2.8 and (2.1)). Arc 1 is also found to be depressed at all temperatures. Capacitances are determined using the expression for all depressed arcs [60]:

$$C_\omega = R^{\frac{1-n}{n}} Q^{\frac{1}{n}} \tag{2.2}$$

Q is the constant phase element (CPE) and n is the frequency power observed from the fitting of the spectra. R_s values are found as 108±1.52, 88±1.24 and 78±0.77 mΩ cm^2 at 650, 700 and 750 ºC, respectively (Table 2.2). This indicates that R_s derived from the ohmic resistance is dependent on the temperature and decreases with the increasing temperature. As seen in Figure 2.18, the high frequency response (Arc 1) with the summit frequency in the range of 20-80 Hz can be assigned to diffusion (10 Hz- 1 kHz) [61, 62]. R_1 is found as 285.6±8.1 mΩ cm^2 at 650 ºC, 111.3±3.2 mΩ cm^2 at 700 ºC and 20±1.9 mΩ cm^2 at 750 ºC (Table 1). A low frequency response (Arc 2), with the summit frequency in the range of 0.3-1 Hz is not a thermally activated process and it means this process is not a part of the electrode reaction kinetics but reflects a concentration polarization [57] such as gas conversion at the anode (0.1–10 Hz) [63]. The value of R_2 is about 80-90 mΩ cm^2 and relatively independent on the operation temperature. The decrease in the total resistance is found to be related mainly to R_1.

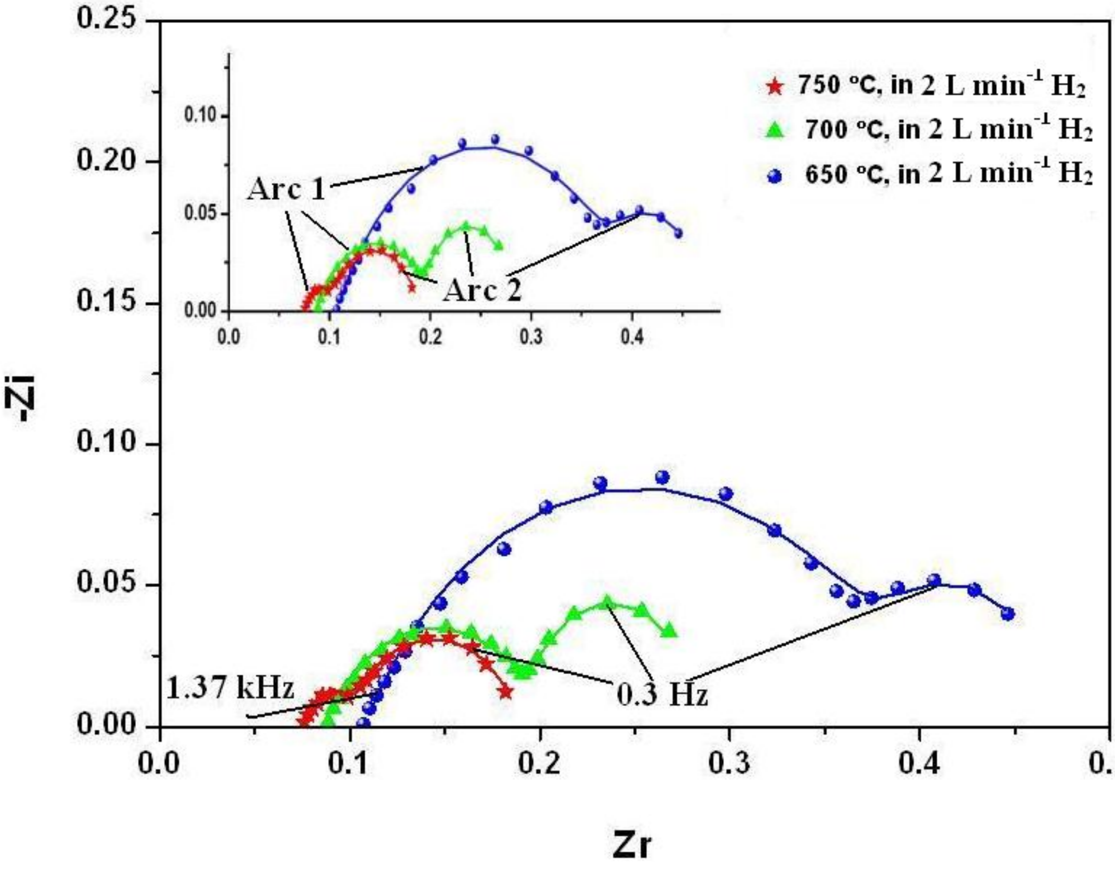

Figure 2.18 Impedance spectra of the cell in dry H_2 at 650, 700 and 750 ºC; symbols and lines respectively shows the measured values and the fittings by the model

Figure 2.19 represents the comparison of the impedance spectra at 750 ºC in dry H_2 and 50 ppm H_2S-containing dry H_2, and the model used to fit the impedance data. |Z| is plotted against the logarithmic frequency to demonstrate the difference in the cell before and after sulfur poisoning at 750 ºC. The impedance spectra are different in frequency ranges below 4.52 Hz. This frequency range was reported to be related to diffusion and/or gas conversion at the anode (summit frequency below 10 Hz) [64]. As shown in Figure 2.19, the sizes of the Arc 1 and Arc 2 respectively related to the gas conversion on the $V_xMo_{(1-x)}O_y$ anode and diffusion of the reactant from/to interface increase with the presence of H_2S in H_2. The significant increase of the Arc 2 indicates the substantial loss of the activity of the $V_xMo_{(1-x)}O_y$ anode for the H_2 oxidation reaction after H_2S-containing H_2 fuel due to the strong chemisorption of H_2S on the anode active sites. This result is compatible with previously reported results for the loss of the activity of Ni/YSZ anodes for H_2S-containing fuel [56].

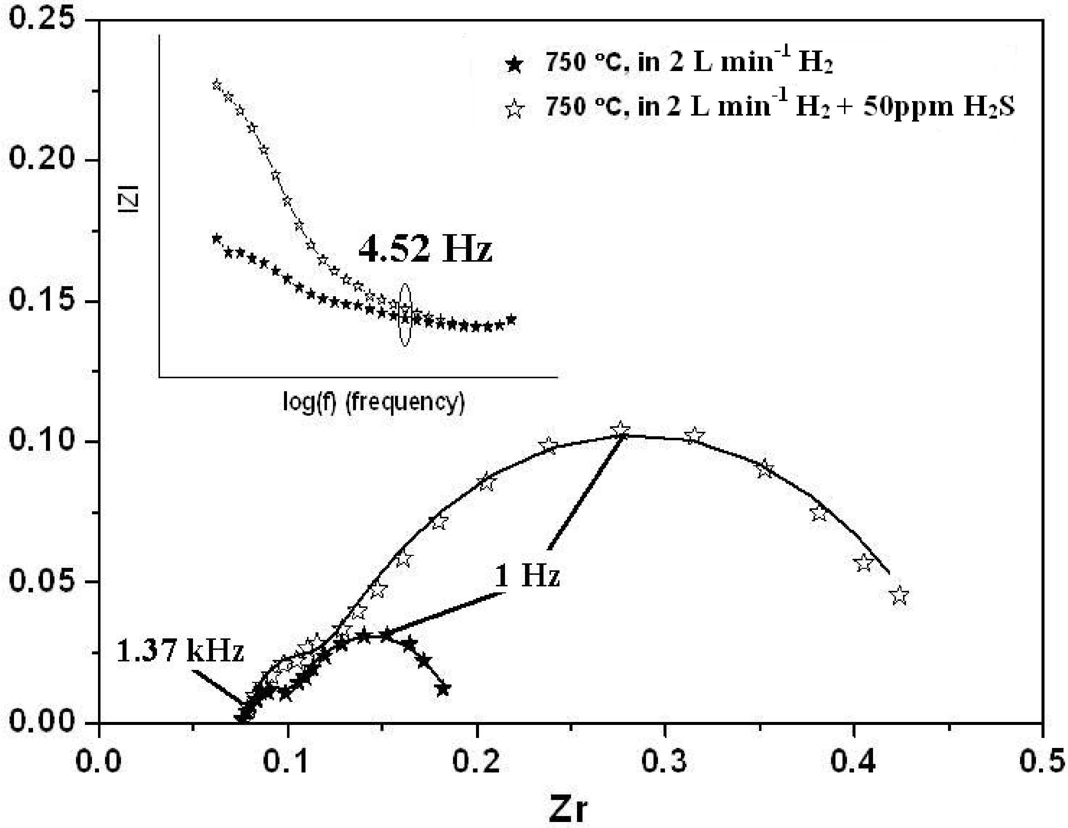

Figure 2.19 The comparison of the impedance spectra of the cell in dry H_2 and 50 ppm H_2S-containing dry H_2 at 750 ºC; symbols and lines respectively shows the measured values and fittings by the model

Table 2.2 Fitted parameters from the impedance measurements of the cell with $V_xMo_{(1-x)}O_y$ anode in pure H_2 and 50 ppm H_2S-containing H_2 at various temperatures

	Pure H_2			**50 ppm H_2S-containing H_2**
	650 ºC	**700 ºC**	**750 ºC**	**750 ºC**
Rs (mΩ cm^2)	108±1.52	88±1.24	78±0.77	77±1.9
R_1 (mΩ cm^2)	285.6±8.1	111.3±3.2	20±1.9	44.6±8.8
C_1 (F cm^{-2})	0.038	0.039	0.052	0.028
n_1	0.67	0.71	0.83	0.77
R_2 (mΩ cm^2)	76±7.6	83±4.25	92±5.2	329±16.4
C_2 (F cm^{-2})	12.24	8.39	0.55	0.50
n_2	1	1	0.8	0.72

Figure 2.20 shows the effect of operation time on OCV of the cell at 750 ºC operation temperature. The OCV values of the single cell in pure and 50 ppm H_2S containing H_2 are compared in the figure. It is seen that the OCV value in pure H_2 is close to theoretical value and it is independent on the operation time. However, the OCV value decreases quickly in an almost linear way just after hydrogen sulfide is introduced into the fuel as expected for a short-term sulfur poisoning process.

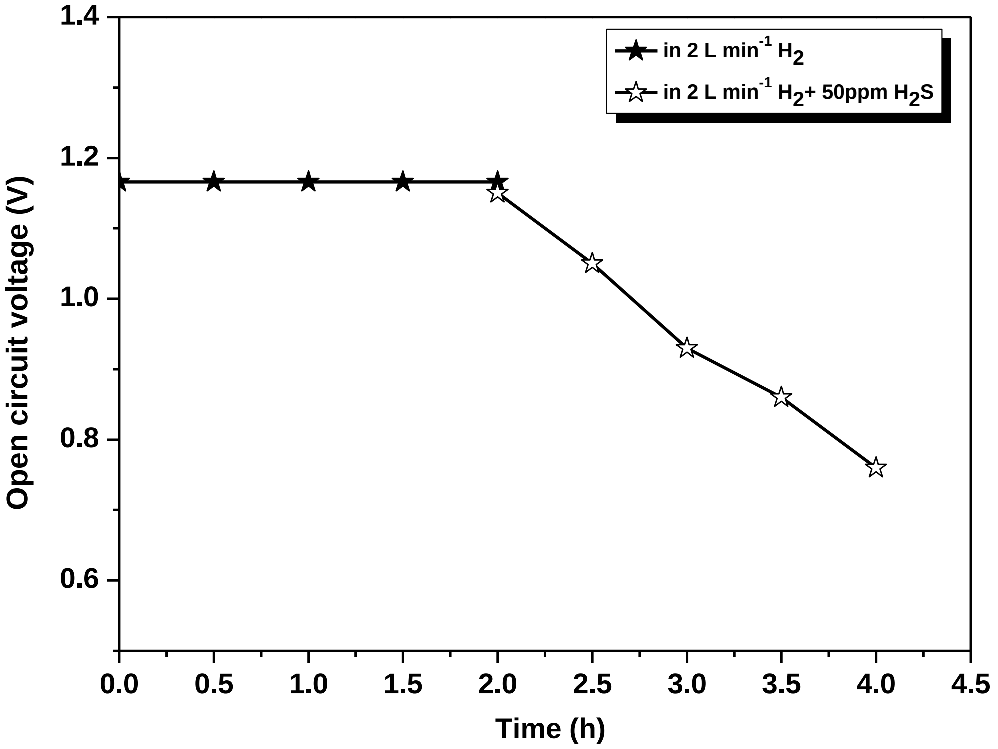

Figure 2.20 The open circuit voltage (OCV) versus time in flowing pure and 50 ppm H_2S-containing H_2. *T*= 750 ºC

Surface Analysis

Figure 2.21 shows the SEM images of the anode surface before and after the test. According to the Figure 2.21 (a), the anode surface has a structure including needle and platelet crystals. It has been reported that $V_{0.13}Mo_{0.87}O_{2.935}$ crystals have a global needle or stick shape and vanadium content in $V_xMo_{1-x}O_y$ systems affects the dimensions of the needles [37, 49]. Platelet crystals are formed above 600 ºC by segregation between the vanadium and molybdenum takes place [49]. Sintering of the anode layer at 650 ºC leads the formation of platelet crystals. During segregation, the vanadium goes away with some neighbouring molybdenum and oxygen atoms, and the platelets of MoO_3 grow on the $V_{0.13}Mo_{0.87}O_{2.935}$ needles and/or sticks. The amount of vanadium decreases in the double layer and this mechanism lasts until all vanadium leaves the particle and MoO_3 is formed (2.1).

Figure 2.21 (b) shows the anode surface of the cell after than 4 hour-testing in H_2 and 50 ppm H_2S containing H_2. It can be clearly seen that the surface morphology of the cell tested with H_2 and H_2S containing H_2 is significantly different from that of the fresh cell, indicating that H_2S decreased the performance of the system. MoO_2 and MoS_2 are formed by reducing of Mo(VI) species to Mo(IV) ones under H_2 (2.2) and H_2S-containing H_2 (2.3) atmospheres [65, 66]:

$$MoO_3 + H_2 \leftrightarrow MoO_2 + H_2O \tag{2.2}$$

$$MoO_3 + 2H_2S + H_2 \leftrightarrow MoS_2 + 3H_2O \tag{2.3}$$

The anode surface of the tested cell presumably includes MoO_3, MoO_2 and MoS_2 particles. Figure 2.22 denotes the cross section of the (a) pre-tested and (b) post-tested cell. It is clear that needles (Figure 2.22 (a)) become platelets of MoO_3 (Figure 2.22 (b)). On the other hand, a decrease in the cell performance by forming of MoS_2 is not expected due to its high electronic conduction. MoS_2 has already tested as SOFC anode materials in H_2S-containing fuels [7, 67, 68] and was reported a good candidate as an anode material for H_2S-powered SOFC [7]. Therefore, instead of MoO_3, MoO_2 and MoS_2 formation, chemisorption of H_2S on the active sites of the anode surface can be related to the decrease in the cell performance. In addition to that, sulfur poisoning of the nickel foam used as the current collector on the anode side presumably contributes to the increase in the resistance of the cell. The surface of the nickel foam exposed to H_2S-containing fuel is poisoned by forming of Ni_xS and this leads to severe cracking, loss of mechanical strength and the significant increase in the electrical resistance [69]. Figure 2.23 represents the stainless steel interconnectors after the measurements under sulfur containing hydrogen. Sulfur deposition is also seen on the interconnectors, which can be responsible of the loss in the cell performance.

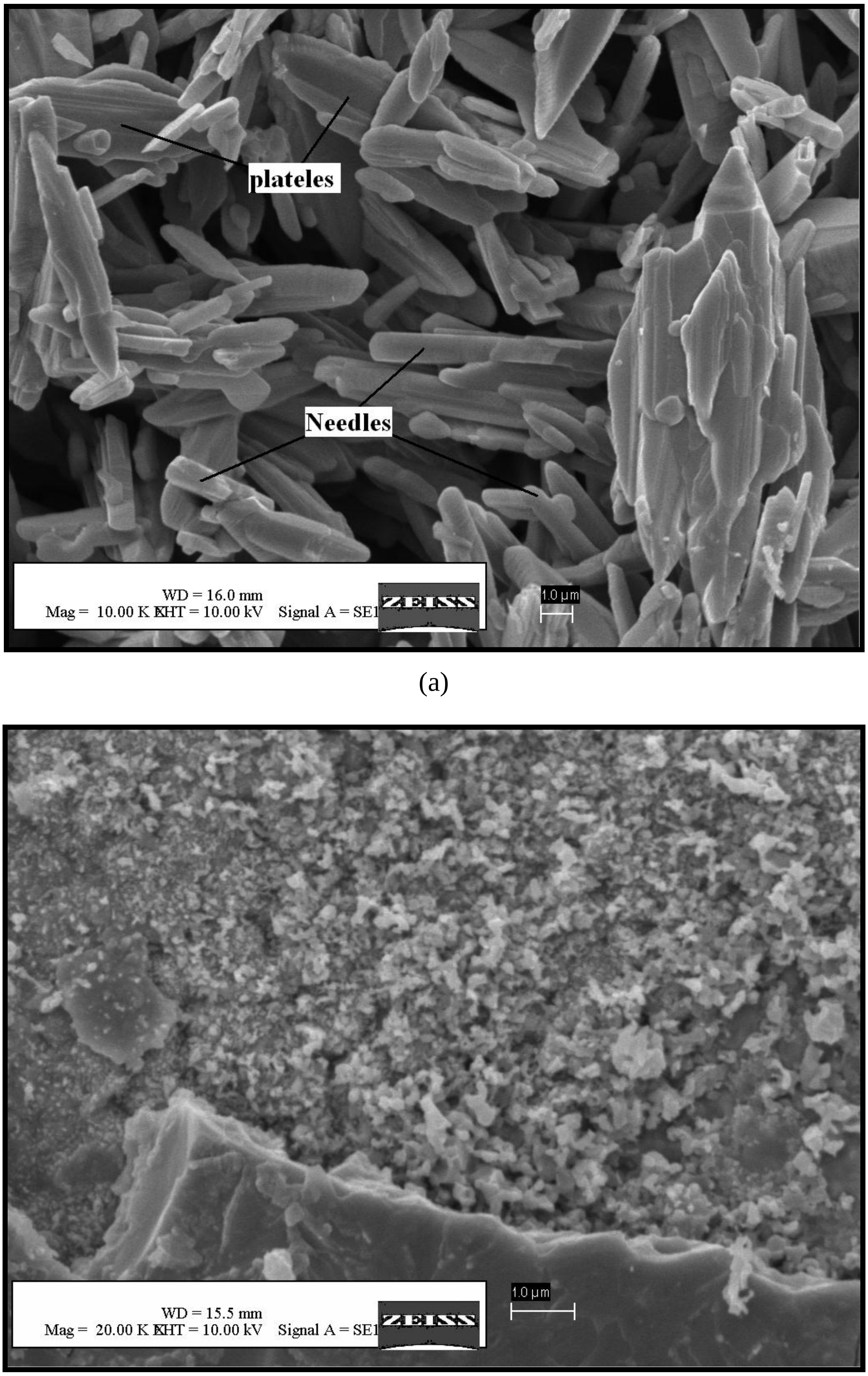

(a)

(b)

Figure 2.21 SEM images of the anode surface; (a) pre-test and (b) post- test

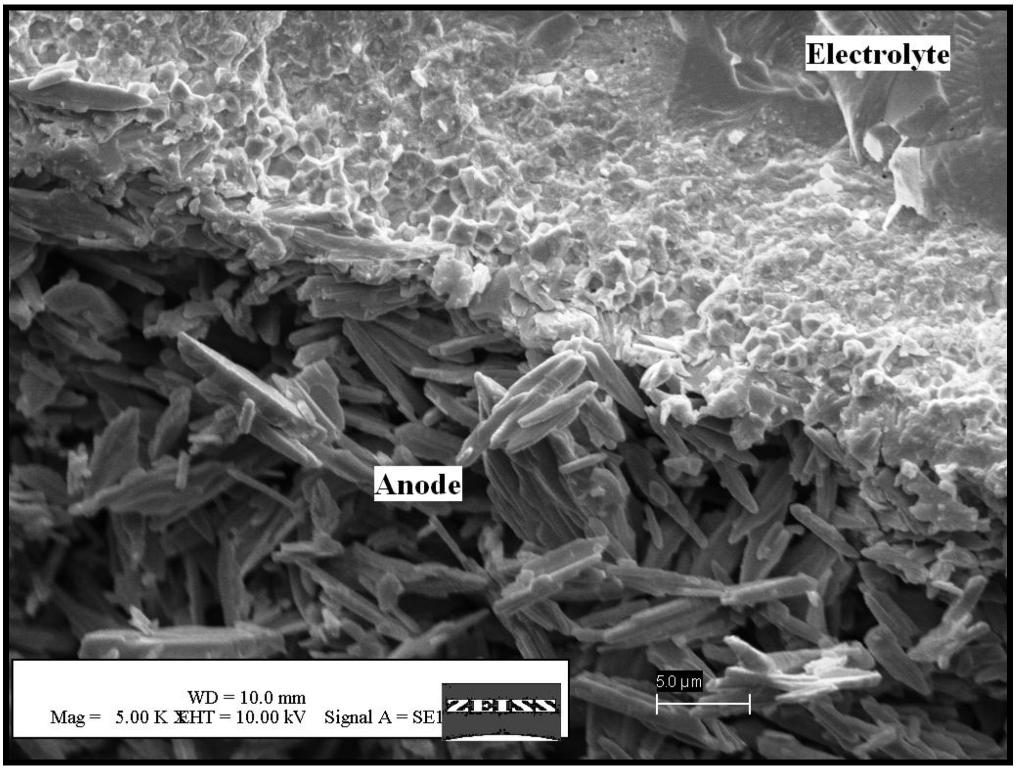

(a)

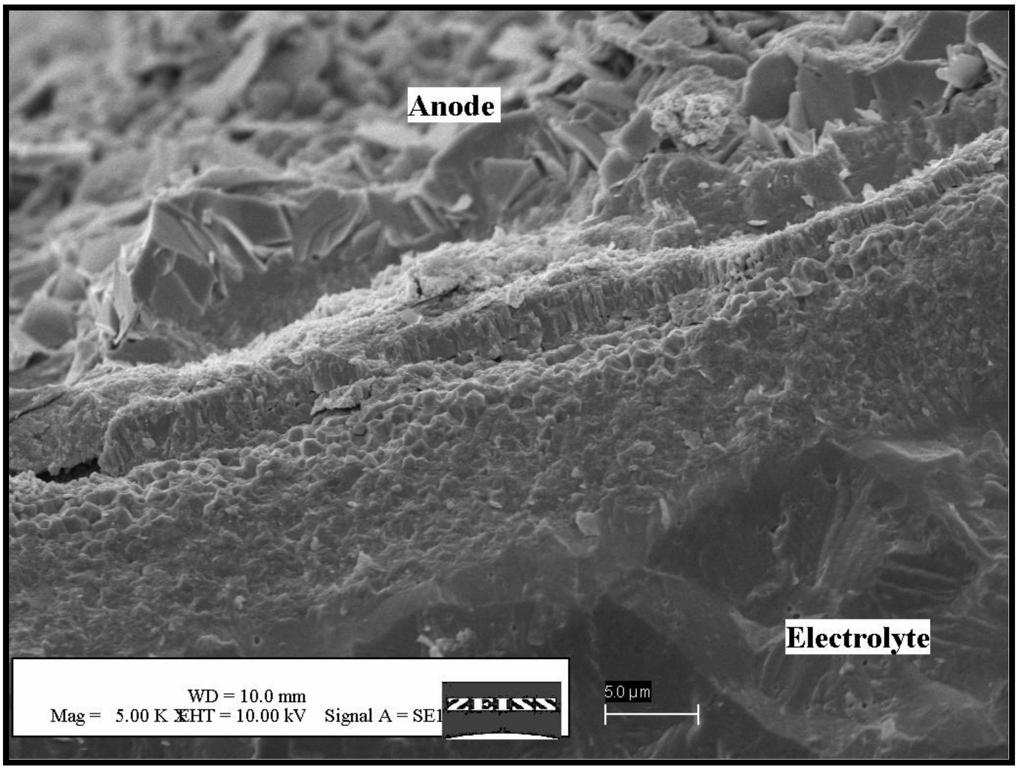

(b)

Figure 2.22 SEM images of the cross section of the (a) pre-tested and (b) post-tested cell (5000X)

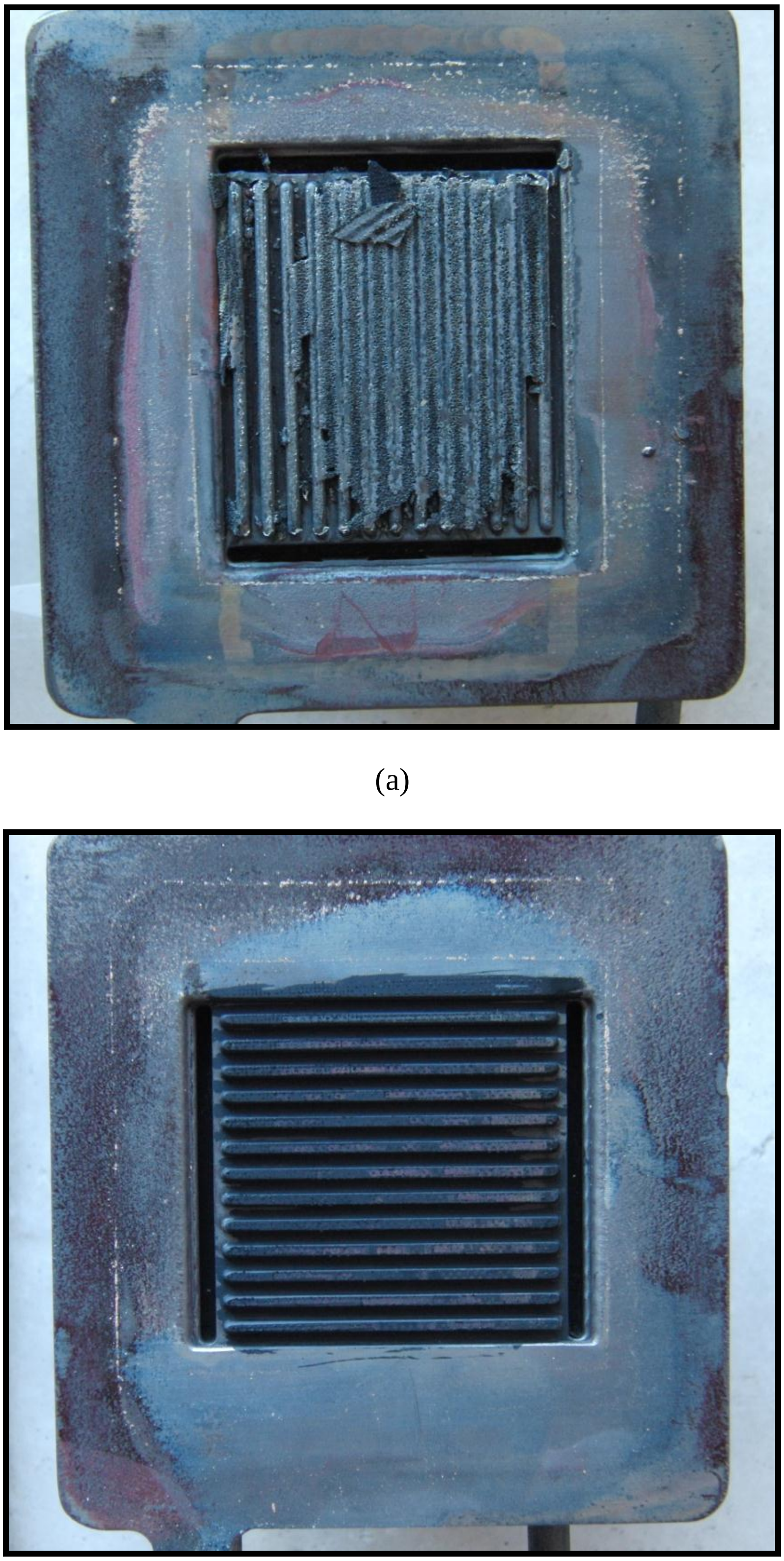

(a)

(b)

Figure 2.23 Stainless steel interconnectors after the measurement under sulfur containing H_2; (a) anode side, (b) cathode side

2.4 Conclusions

In summary, $V_{0.13}Mo_{0.87}O_{2.935}$ powder was successfully synthesized by reducing acidified vanadate and molybdate solution at 60 ºC by passing hydrogen sulfide gas through the solution. A phase transition between hexagonal to orthorhombic structures was observed at low temperature (430 ºC) despite contrary indications in the literature.

The electrochemical behavior and sulfur tolerance of $V_xMo_{(1-x)}O_y$ mixed oxide were investigated as an anode material for solid oxide fuel cell. Performance measurements showed that the highest cell performance with a peak power of 2.88 W was observed at an operation temperature of 750 ºC in dry $H_{2.}$ It was found that 50 ppm H_2S contamination in dry H_2 caused a 22% decrease in the peak power and the deactivation process was found to be irreversible for a short-term exposure to sulfur free gas. However, the reactivation of the cell may be achieved through a long-term hydrogen treatment, which causes a reaction of hydrogen with adsorbed sulfur to form the volatile compound of H_2S.

Electrochemical impedance measurements resulted in two responses at high and low frequencies, respectively. The high frequency response was considered as a thermally activated process thus can be assigned to diffusion. The low frequency response, on the other hand, was relatively independent on temperature and attributed to the gas conversion on the anode surface. Furthermore, 50 ppm-H_2S contamination in dry H_2 negatively affected the electrode polarization resistance due to the chemical adsorption of the anode active sites and OCV value of the cell decreased linearly as expected for a typical short-term sulfur poisoning process.

CHAPTER 3

NOVEL RUBIDIUM PHOSPHITE TELLURATE COMPOUND

In this chapter, structural, thermal and electrical properties studies of rubidium phosphite tellurate, $RbH(PO_3H).Te(OH)_6$, were performed. An endothermic peak, which reached a completion at about 315 °C accompanied with a weight loss of 4.6 wt.%, was attributed to dehydration. Four types of pellets were produced, namely pellets A, B, C and D. Pellet A was tested with platinum-carbon paper electrode, and pellets B, C and D were tested with gold electrodes. Both pellets A and B were studied from 113 °C to 317 °C for 135 hours. Pellet C was first investigated from room temperature to 176 °C for 360 hours. After cooling down to room temperature, a second measurement with pellet C was carried out under the same conditions as used for pellets A and B. Pellet D, on the other hand, was heated up to 450 ºC, kept at that temperature for two hours and then cooled down to room temperature prior to the conductivity measurements. It was observed that the conductivities of pellets A and B decreased to the values of $5.2 \cdot 10^{-8}$ S cm^{-1} and $6.6 \cdot 10^{-7}$ Scm^{-1} at 317 °C, respectively. And an unexpected rise in the conductivity ($9.89 \cdot 10^{-6}$ S cm^{-1} at 317 °C) was seen with pellet C. Dehydration of $RbH(PO_3H)\cdot Te(OH)_6$ might be responsible for this unexpected rise in the conductivity of pellet C. The monoprotic part $RbH(PO_3H)$ of $RbH(PO_3H)\cdot Te(OH)_6$ apparently became diprotic ($Rb_2H_2P_2O_5$) part of $Rb_2H_2P_2O_5\cdot[Te(OH)_6]_2$ after dehydration. The measured conductivity of pellet D, which was dehydrated prior to the measurement, reached a value of $5.41 \cdot 10^{-5}$ S cm^{-1} at 317 °C and showed a good stability over-each-run time and temperatures measurement up to 317 °C. The dehydrated compound, $Rb_2H_2P_2O_5\cdot[Te(OH)_6]_2$, has also a higher hydrogen density relative to the starting compound, $RbH(PO_3H)\cdot Te(OH)_6$. The completion of the dehydration may be responsible for the unexpected rise in the conductivity of $RbH(PO_3H)\cdot Te(OH)_6$. This unusual case is important for studies in solid acid proton conductors.

3.1 Introduction

Many acid salts of inorganic oxy-acids have gained attention as promising electrolytes. Some of their properties, such as proton conductivity or ferroelectric transition, are due to specific features of hydrogen bonds formed in crystal structures of these compounds [21, 70, 71].

Alkali-metal acid sulfates and acid phosphates have been studied in detail since Baranov and coworkers [23, 72 73] demonstrated that the conductivity of $CsHSO_4$ increases with 2 to 3 orders of magnitude upon heating the material above its phase transition temperature where it goes from a monoclinic phase to a high-temperature tetragonal phase. On the other hand, the first systematic results on the crystal structures of acid phosphites, such as MH_2PO_3 (where M= Rb^+, Cs^+, Tl^+), $(MH_2PO_3H)_2 \cdot H_3PO_3$ (where M= Rb^+, Tl^+) and $MH_2PO_3 \cdot H_3PO_3$ (where M= K^+, Cs^+) were presented by Kosterina and coworkers [70, 71]. Chisholm et al. [25] showed that cesium dihydrogen phosphite, $CsH(PO_3H)$, undergoes a transition, with an onset of 137 °C, to a phase with high proton conductivity. Zhou et al. [24] studied electrical conductivity of solid acid phosphites $MH(PO_3H)$ with M= Li^+, Na^+, K^+, Rb^+, Cs^+, NH_4^+ for the first time. They observed superprotonic conductivity following a phase transition in the temperature range from 120 to 190 °C for the monoclinic forms, including Na^+, K^+, Rb^+, Cs^+, NH_4^+ derivatives. No superprotonic phase transition was observed for orthorhombic $LiH(PO_3H)$. The conductivities of $KH(PO_3H)$ and $LiH(PO_3H)$ reached the values of $4.2 \cdot 10^{-3}\ \Omega^{-1}\ cm^{-1}$ (at 140 °C) and $3 \cdot 10^{-3}\ \Omega^{-1}\ cm^{-1}$ (at 160 °C), respectively. Bondarenko et al. [23] investigated a superprotonic $KH(PO_3H)$-SiO_2 composite electrolyte and showed that dispersion with nano-sized SiO_2 particles leads to improved mechanical properties.

Compounds with general formulas of $M_xM'_{(1-x)}AO_4 \cdot Te(OH)_6$ and $M_2(AO_4)_x(A'O_4)_{(1-x)} \cdot Te(OH)_6$ (where M, M′ is Na^+, K^+, Rb^+, NH_4^+, Tl^+ and A, $A'=S^{2-}$, Se^{2-}) were studied by Dammak and coworkers [29-33, 74-85]. They showed that all of these compounds exhibit superprotonic behaviour. The conductivity of $8 \times 10^{-2}\ S\ cm^{-1}$ in air at 357 °C was achieved for $Rb_2(SO_4)_{0.5}(SeO_4)_{0.5} \cdot Te(OH)_6$ [31]. The stability of phosphites in hydrogen atmosphere and the relatively high operating temperature of tellurate compounds inspired us to investigate rubidium phosphite tellurate. This part of the study presents the first results of synthesis, structural, thermal and electrical studies on $RbH(PO_3H).Te(OH)_6$.

3.2 Experimental

Rubidium carbonate (99.8%, Sigma-Aldrich), phosphorous acid (99%, Sigma-Aldrich) and telluric acid (99%, Sigma-Aldrich) with a molar ratio of 1:2:2 were dissolved in deionized water, separately. Concentrations of Rb_2CO_3, $H_2(PO_3H)$ and $Te(OH)_6$ solutions were 12.63 mmol/40 mL, 25.25 mmol/15 mL and 25.25 mmol/ 25mL, respectively. The phosphorous acid solution was slowly added to the rubidium carbonate solution. After one hour, telluric acid solution was added to the obtained solution. $RbH(PO_3H).Te(OH)_6$ powder was obtained by slow evaporation of the aqueous solution continuously at approximately 50 °C during 2 days.

The reaction is:

$$Rb_2CO_3 + 2H_2(PO_3H) + 2Te(OH)_6 \rightarrow 2RbH(PO_3H)\cdot Te(OH)_6 + CO_2 + H_2O \qquad (3.1)$$

The powder was dried in an oven in air at about 130 °C during two weeks prior to experiments.

Scanning Electron Microscopy and Energy Dispersive X-ray Spectroscopy (EDS) analysis were carried out using a Zeiss Evo 60. EDS data were analyzed using the NSS 2.2 X-ray MicroAnalysis program. X-ray diffraction data were recorded at room temperature using Stoe Theta-Theta XRD (40 kV, 30 mA, Cu $K\alpha_1$) and analyzed using the STOE Win XPOW 2.20 program. Termogravimetry and differential thermal analysis were carried out in air using TG-DTA system (Netzsch STA 409 CD) with a scan rate of 5 °C min^{-1}. Differential scanning calorimetry (DSC) experiments were performed in air by Netzsch DSC 200 F3, heating $RbH(PO_3H)\cdot Te(OH)_6$ from room temperature to 500 °C with a scan rate of 5 °C min^{-1}. Samples were ground with an agate mortar prior the measurements.

Conductivity measurements were carried out using electrochemical impedance spectroscopy. Four pellets, namely pellet A, B, C and D were produced by pressing $RbH(PO_3H)\cdot Te(OH)_6$ powders into discs of about 1 mm thickness and 8 mm diameter at 200 MPa pressure. The rig used in the experiments is given in Figure 3.1. The pellet A was tested with platinum-carbon paper electrode, and the pellets B, C and D were tested with gold electrodes. Gold electrodes were sputtered on both sides of the pellets B, C and D. Both the pellets A and B were investigated from 113 °C to 317 °C for 135 hours. The pellet C was first investigated from room temperature to 176 °C for 360 hours. After cooling down to room temperature, a second measurement with pellet C was carried out under the same conditions as used for the pellets A and B. The pellet D, on the other hand, was heated up to 450 ºC, kept at that temperature for two hours and then cooled down to room temperature at heating/cooling scan rate of 1 °C min^{-1} prior to the conductivity measurements. The heating procedures applied to the pellets are given schematically in Figure 3.2.

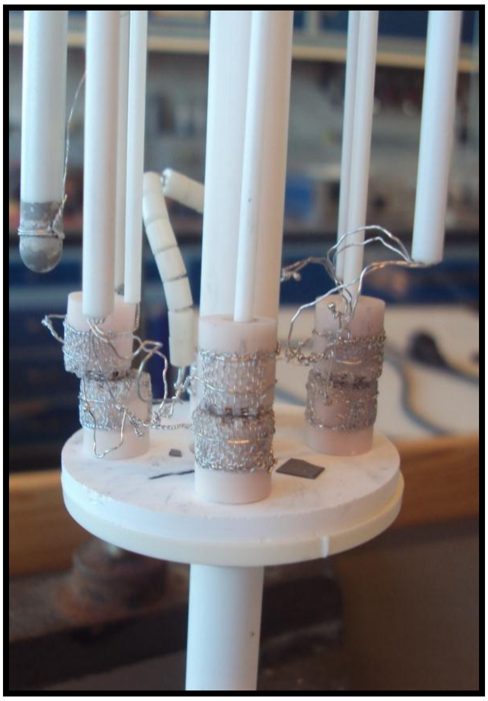

Figure 3.1 The rig used in the EIS experiments

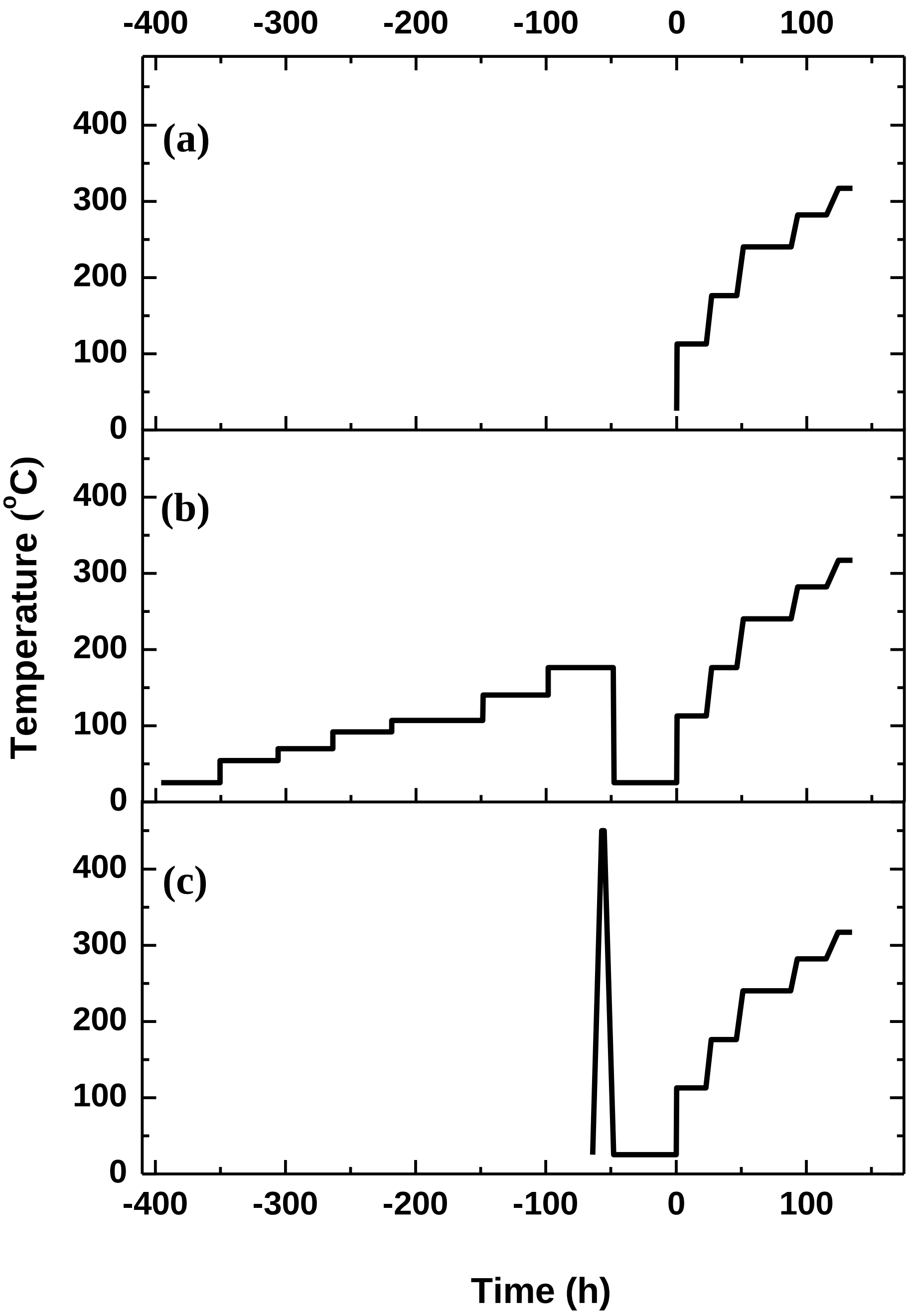

Figure 3.2 The heating procedures applied to (a) the pellets A and B, (b) the pellet C and (c) the pellet D. The pellets A and B were tested for 135 hours between 113 to 317 °C. The pellet C (earlier investigated at various temperatures up to 176 °C for 360 hours) and the pellet D (heated up to 450 °C and then cooled down to room temperature prior to the measurement) were tested under the same conditions as used for the pellets A and B.

The measurements were done under dry air ($pH_2O < 0.001$ bar), humidified air ($pH_2O = 0.1$ bar) and humidified gas mixture of 9 % H_2 in N_2 ($pH_2O = 0.1$ bar). The gases were humidified by bubbling the gas through a heated water bottle ($T(H_2O)= 46$ °C). Impedance spectra were recorded under flowing gases (50 mL/min) using a Solartron 1260 frequency analyzer in all measurement series. An excitation voltage with amplitude of 20 mV was used. No bias voltage was applied. The temperature of measurement was increased stepwise with heating rates of 5 °C min^{-1}. Measurements were carried out over the frequency range of 1 MHz to 1 Hz. Data analysis was done using the ZSimpWin 3.21 program.

3.3 Results and Discussions

3.3.1 Structural and Thermal Analysis

Synthesis with slow evaporation resulted in $RbH(PO_3H)\cdot Te(OH)_6$ particles with diameters in the range of less than 1 to 60 µm. A SEM micrograph of the synthesized powder is shown in Figure 3.3. It can be seen that smaller particles tend to form agglomerates.

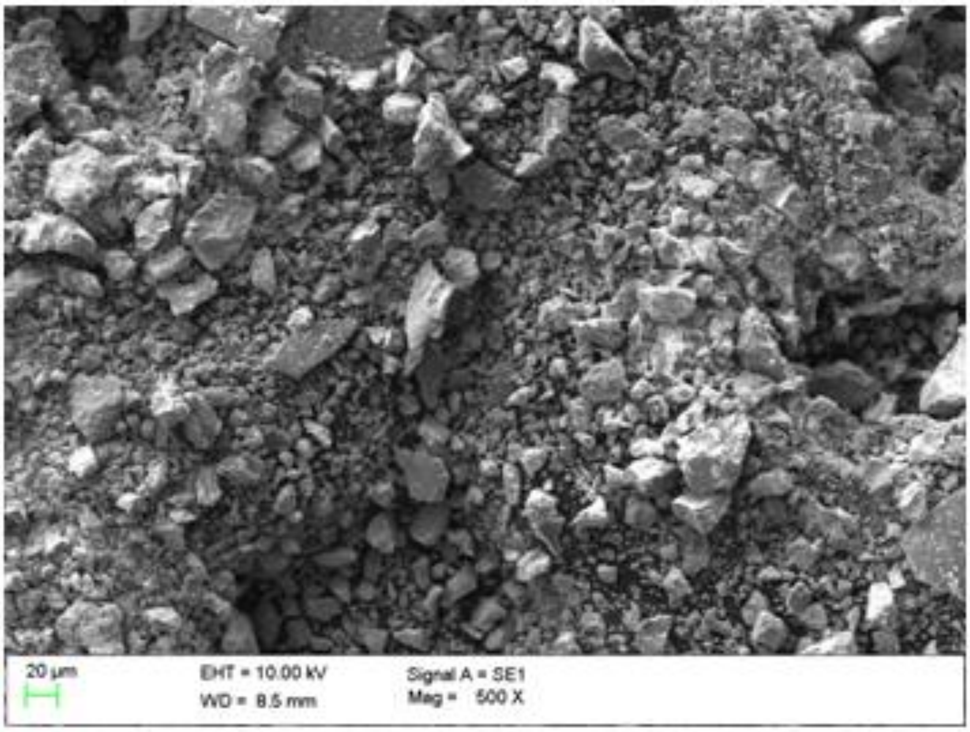

Figure 3.3 SEM image taken from $RbH(PO_3H)\cdot Te(OH)_6$ powder which was synthesized by slow evaporation of the aqueous solution, X500

Figure 3.4 gives a typical EDS spectrum, which shows that the powder consists of the expected elements (hydrogen cannot be detected by EDS). Figure 3.5 shows the results of 5 EDS point analyses on the surface of the powder, which shows distribution of elements for different points. Referring to Figure 3.5, the difference in composition (atomic %) of the synthesized $RbH(PO_3H){\cdot}Te(OH)_6$ compound that is seen for each point investigated by EDS analysis may be attributed to topographical effects rather than variation of the chemical composition across the sample [86].

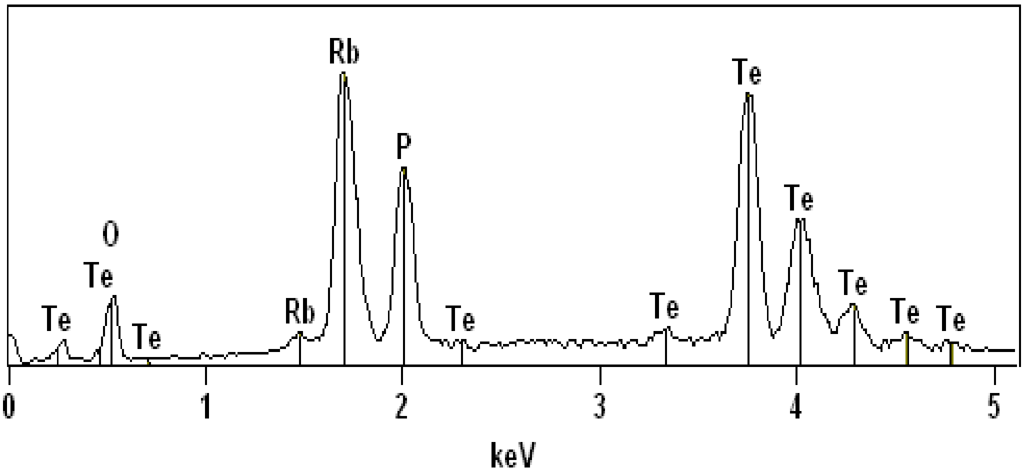

Figure 3.4 EDS spectrum showing typical composition of the synthesized $RbH(PO_3H){\cdot}Te(OH)_6$ powder (Hydrogen is not detectable by EDS analysis)

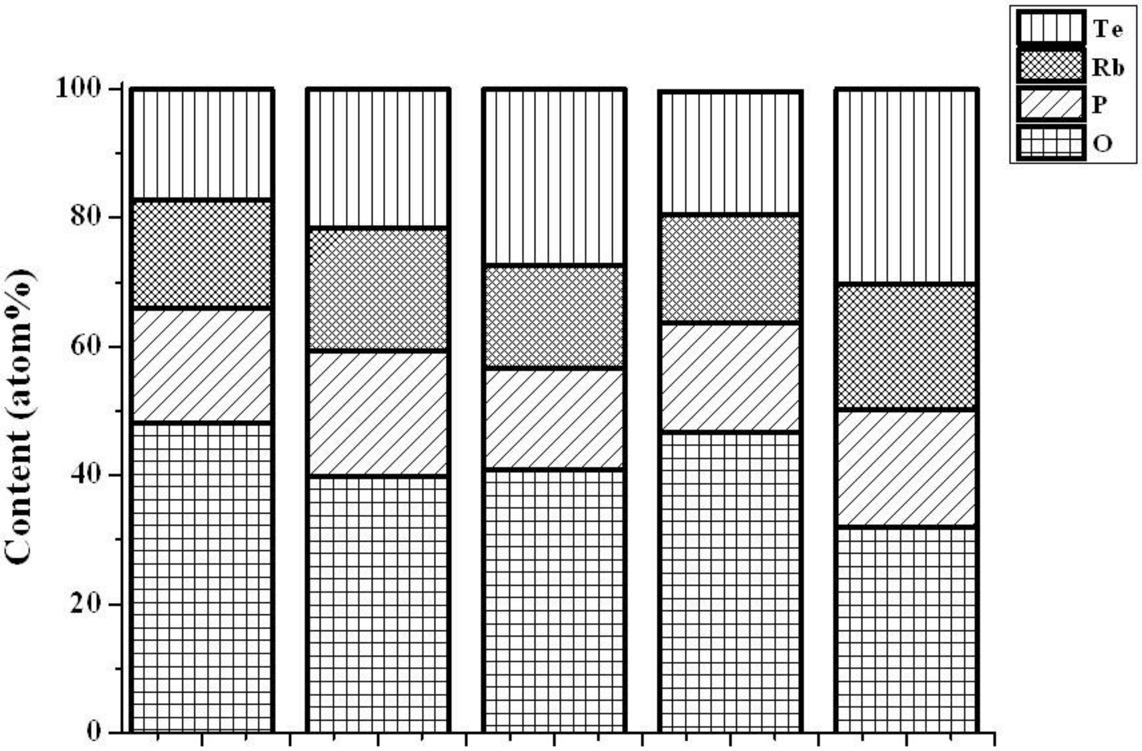

Figure 3.5 Point analysis showing distribution of detectable elements at five different points on the surface of the synthesized $RbH(PO_3H)\cdot Te(OH)_6$ (Hydrogen is not detectable by EDS analysis)

Thermal analysis reveals the thermal behavior of the $RbH(PO_3H)\cdot Te(OH)_6$ powder and to monitor weight losses due to dehydration. Figure 3.6 and Figure 3.7 (a), respectively, indicate that both DTA and DSC profiles of $RbH(PO_3H)\cdot Te(OH)_6$ show a pronounced endothermic peak at 233 °C on the first heating cycle. While cooling from a maximum temperature of 500 °C, no reverse of the first transition is seen in Figure 3.7 (a). Moreover, Figure 3.7 (b) demonstrates neither an endothermic nor an exothermic peak occurs during the second heating/cooling cycles. The weight loss accompanied by the endothermic peak is completed at about 315 °C with a total loss of 4.6 wt.%. The weight loss is in a good agreement with the following dimerization reaction as given the same reaction for all $MH(PO_3H)$ compounds [23]:

$$2RbH(PO_3H)\cdot Te(OH)_6 \rightarrow Rb_2H_2P_2O_5\cdot[Te(OH)_6]_2 + H_2O \qquad \Delta H>0 \tag{3.2}$$

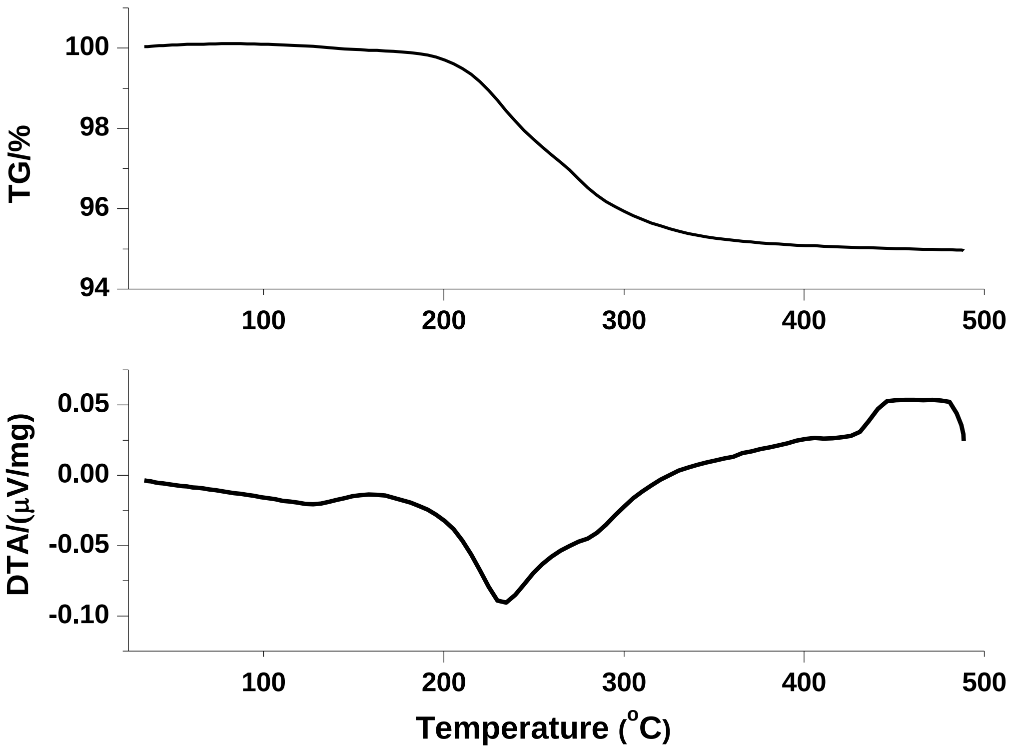

Figure 3.6 TG/DTA analysis of the synthesized $RbH(PO_3H)\cdot Te(OH)_6$ at a scan rate of 5 °C min^{-1}

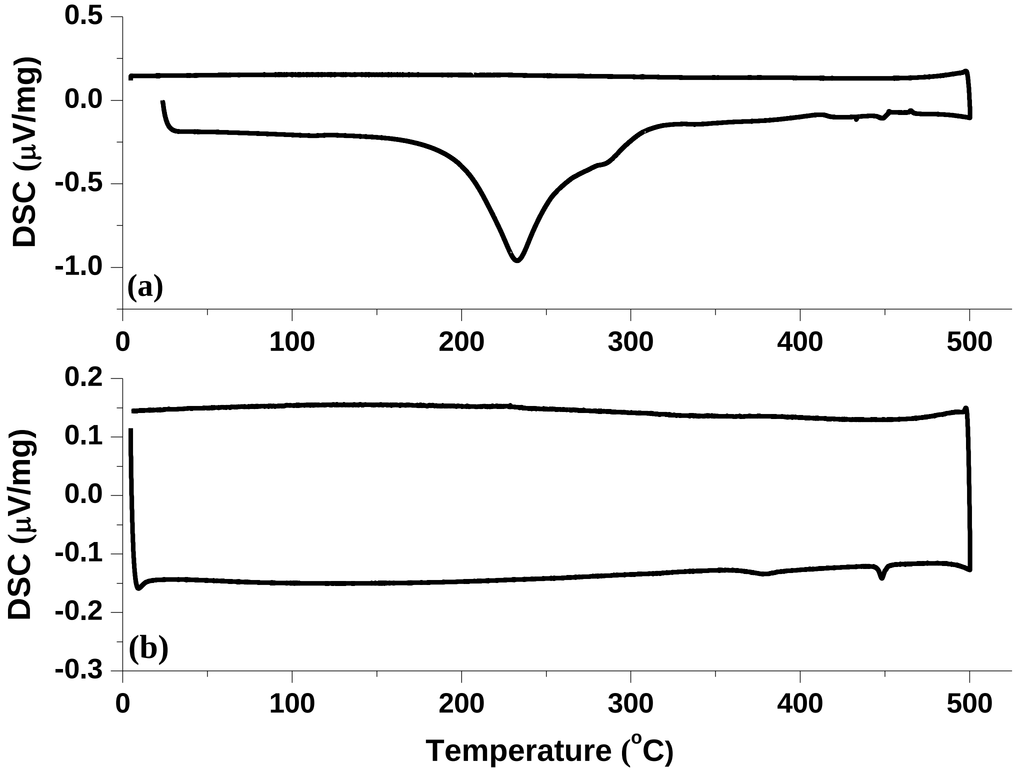

Figure 3.7 DSC analysis of the synthesized $RbH(PO_3H)\cdot Te(OH)_6$ at a scan rate of 5 °C min^{-1} (a) first heating/cooling cycle, (b) second heating/cooling cycle

The endothermic peak that reaches a completion at about 315 °C on the first heating cycle does not show any reverse action on the first cooling cycle. This indicates that the dehydration of $RbH(PO_3H)\cdot Te(OH)_6$ is completed at about 315 °C. This is evident not only from the DSC analysis, but also from the weight loss at 315 °C, which is in an agreement with the dimerization reaction (3.2) of $RbH(PO_3H)\cdot Te(OH)_6$. The observed weight loss for $RbH(PO_3H)\cdot Te(OH)_6$ extends over a wide temperature ranges as reported for all phosphite salts in the literature [23].

Figure 3.8(a) gives room temperature XRD patterns of the synthesized $RbH(PO_3H)\cdot Te(OH)_6$ indexing of amorphous and crystalline structures. All pellets were investigated up to dehydration temperature of $RbH(PO_3H)\cdot Te(OH)_6$. Figure 3.8(b-e) show room temperature XRD patterns of the pellets A, B, C, D after the conductivity measurements. Figure 3.8(b and c) represent a transformation from amorphous towards a more crystalline structure becomes visible for the tested pellets A and B, while it reaches the completion for the tested pellet C as seen in Figure 3.8(d). Figure 3.8(e) illustrates the tested pellet D mainly has a crystalline structure with some residuals amorphous structure, it is seen that a complete dehydration of $RbH(PO_3H).Te(OH)_6$ was not achieved for a two-hour pretreatment at 450 °C. XRD results of the tested pellets, however, show that only pellet C reached a complete of dehydration while pellets A, B and D did not. This situation can be attributed to the difference in the operating time of the pellets. Although, the test for the pellet C was performed under the same conditions as used for the pellets A and B, it was investigated at temperatures up to 176 °C for 360 hours prior to the experiment. On the other hand, pellet D was heated up to 450 °C, kept at that temperature for two hours and then cooled down to room temperature prior to measurements. XRD results of the tested pellet D still shows both crystalline and amorphous structures. As a result of this, it can be said that $RbH(PO_3H){\cdot}Te(OH)_6$ needs a heating duration of more than two hours to be dehydrated completely at 450 °C.

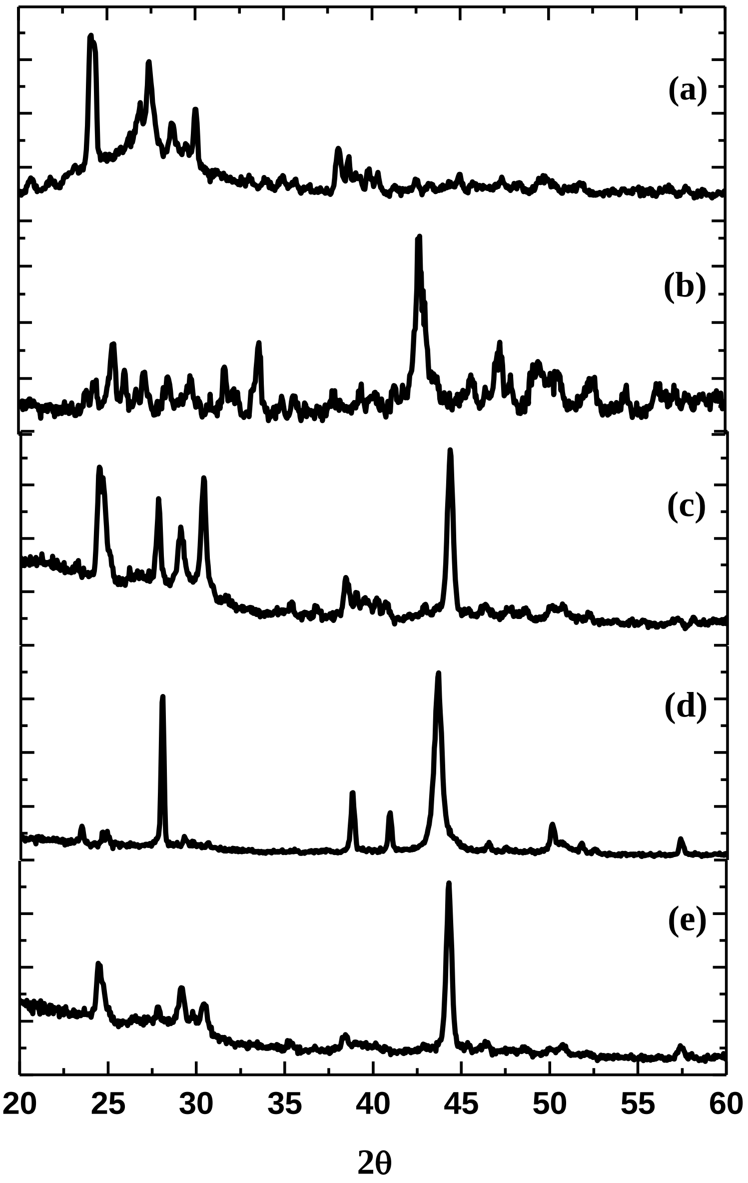

Figure 3.8 XRD diagrams of (a) the synthesized $RbH(PO_3H).Te(OH)_6$ powder, (b) the tested pellet A, (c) the tested pellet B, (d) the tested pellet C and (e) the tested pellet D. The pellets A and B were tested respectively with platinum-carbon and gold electrodes for 135 hours between 113 to 317 °C. The pellet C (earlier investigated at various temperatures up to 176 °C for 360 hours) and the pellet D (heated up to 450˚C and then cooled down to room temperature prior to the measurement) were tested with gold electrodes under the same conditions as used for the pellets A and B.

3.3.2 Electrochemical Impedance Spectroscopy

Impedance spectra were obtained in the temperature range of 113 °C to 317 °C. Comparisons of conductivity results for the pellets A and B and for the pellets C and D are given in Figure 3.9 and Figure 3.10, respectively. As seen in Figure 3.9, the measured conductivities of both pellets A and B increases by changing the atmosphere from dry air ($pH_2O < 0.001$ bar) to humidified air ($pH_2O=0.1$ bar) at 113 °C. It increases further when changing the gas from humidified air to humidified gas mixture of 9 %H_2 in N_2 ($pH_2O=0.1$ bar) at 176 °C. The pellets investigated generally for 20-25 hours at each temperature show a small decrease in the conductivity by the operating time. In contrast to the general view, the conductivity decreases remarkably by operating for 40 hours at 240 °C. It can be seen that the conductivity of $RbH(PO_3H).Te(OH)_6$ depends on temperature, operating time, atmosphere and water content of flowing gases. The measured conductivity of the pellet B shows higher values than that of the pellet A and this difference in the conductivity reaches one order of magnitude at 240 °C. Figure 3.11 gives two impedance spectra of both pellets A and B measured at 240 °C. The conductivities of the pellets C and D also increases by changing atmosphere from dry air to humidified air at 113 °C and by flowing gas from humidified air to humidified gas mixture of 9 %H_2 in N_2 at 176 °C. The conductivity of the pellet C decreases by operating time as seen for the pellets A and B. Even though, the measured conductivity of the pellet D decreases by time under both dry and humidified air, it shows enhanced stability in the conductivity over time under humidified gas mixture of 9 % H_2 in N_2.

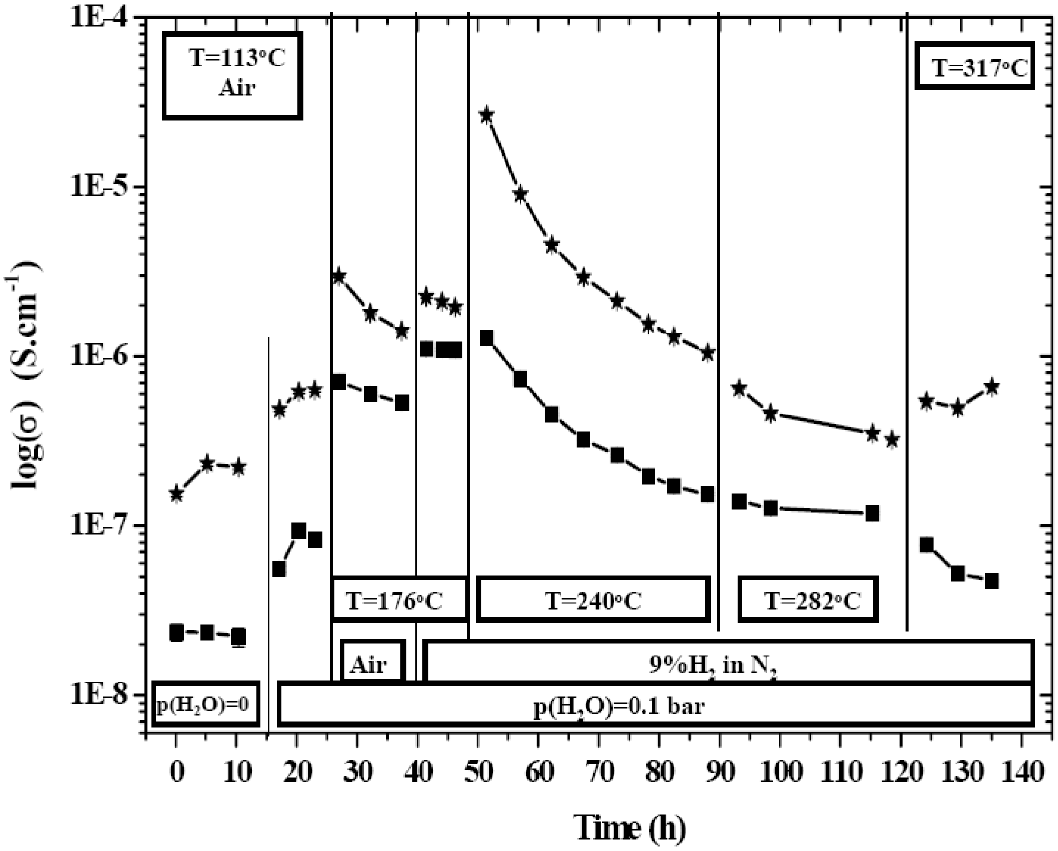

Figure 3.9 Plot of conductivity (log(σ) versus time) for ■ the pellet A, ✶ the pellet B at various temperatures and atmospheres. The pellets A and B were tested with platinum-carbon and gold electrodes, respectively.

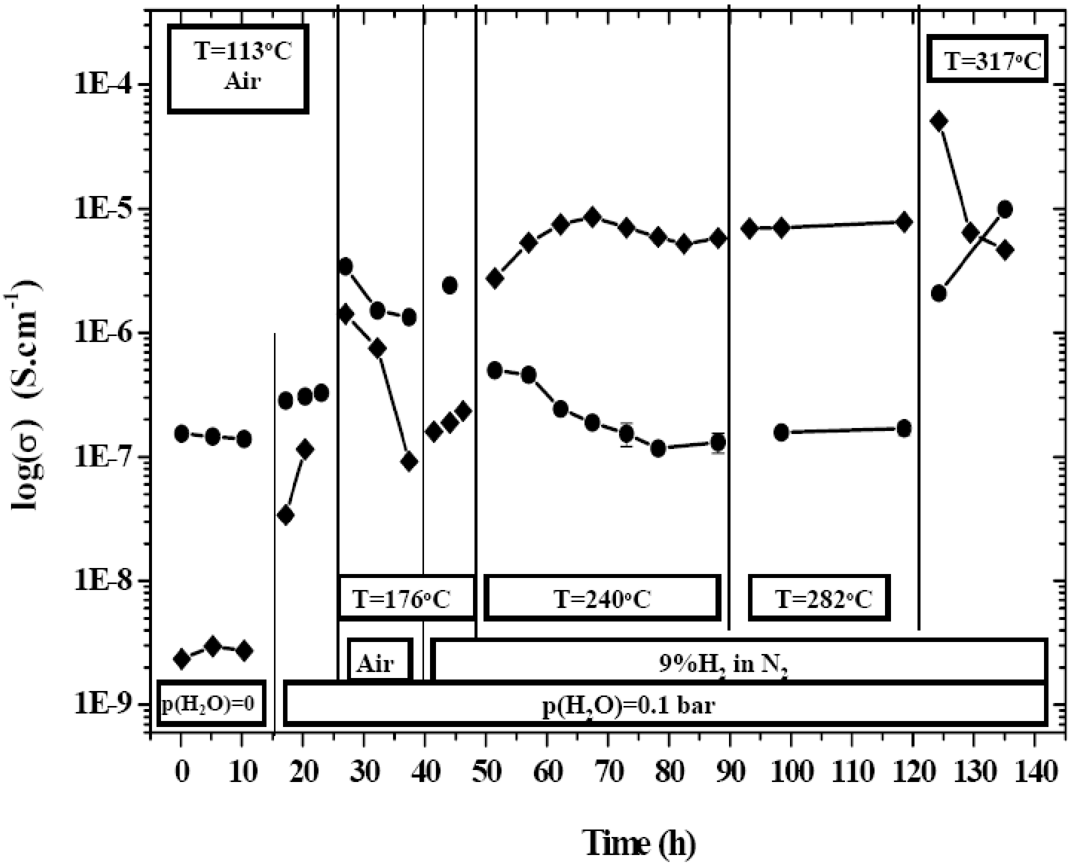

Figure 3.10 Plot of conductivity (log(σ) versus time) for ● the pellet C, ◆ the pellet D at various temperatures and atmospheres. Both pellets were tested with gold electrodes.

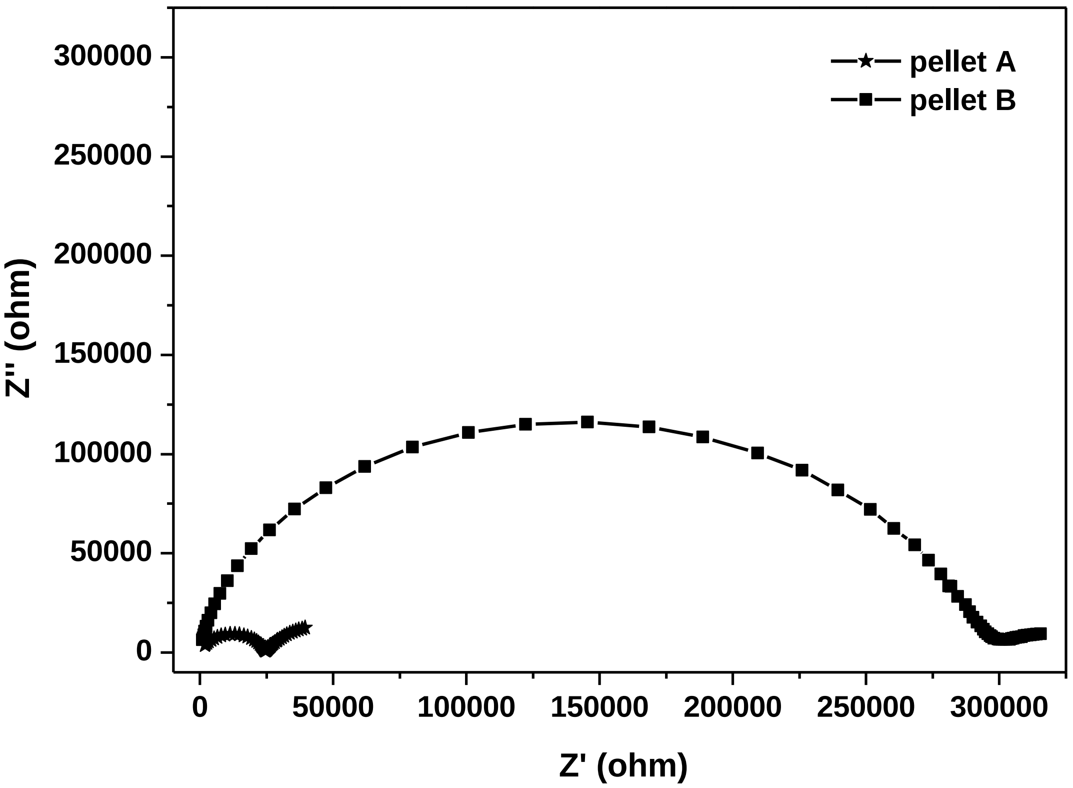

Figure 3.11 Impedance spectra of ■ the pellet A, ✶ the pellet B at 240 °C; the pellets A and B were tested with platinum-carbon and gold electrodes, respectively.

It can be concluded that all pellets show an increase in the conductivity by changing atmosphere from dry air to humidified air at 113 °C and this trend with humidified air continues between temperatures of 113 °C to 176 °C. Even though the conductivities of all pellets decrease by time at 176 °C under humidified air, yet the pellet D shows a greater decrease in the conductivity (more than one order of magnitude) as compared to others. At this temperature, all pellets also show an increase in the conductivity by changing from humidified air to humidified gas mixture of 9 %H_2 in N_2. Under the gas mixture, the conductivities of all pellets decrease by time at 240 °C with the exception of the pellet D. While the pellet A tested with platinum-carbon paper electrodes shows a conductivity of $1.28 \cdot 10^{-6}$ S cm^{-1} at 240 °C, the pellet B tested with gold electrodes reaches a conductivity value of $2.66 \cdot 10^{-6}$ S cm^{-1} at the same temperature. This difference can be attributed to the electrode contribution, as the ohmic resistance associated with the pellet A has not been subtracted.

Moreover, the conductivities of the pellets A and B decrease to $4.04\cdot10^{-8}$ S cm^{-1} and $6.6\cdot10^{-7}$ S cm^{-1} at 317 °C respectively, while pellet C, which completed the dehydration at that temperature, shows an unexpected rise in the conductivity with a value of $9.89\cdot10^{-6}$ S cm^{-1}. The conductivities of the pellets A, B and C decrease during the dehydration and this behavior is in an agreement with the literature. The conductivity of the pellet C, however, starts to increase after the completion of the dehydration at 317 °C. The dehydration mechanism (see 3.1) can be responsible for this unexpected rise in the conductivity in two ways:

(1) Monoprotic $RbH(PO_3H)$ part of $RbH(PO_3H)\cdot Te(OH)_6$ compound becomes diprotic $Rb_2H_2P_2O_5$ part of $Rb_2H_2P_2O_5\cdot[Te(OH)_6]_2$ compound upon dehydration

(2) Dehydrated compound, $Rb_2H_2P_2O_5\cdot[Te(OH)_6]_2$, has a higher hydrogen density than $RbH(PO_3H)\cdot Te(OH)_6$

The heat treatment was done in order to investigate in depth the conductivity of dehydrated compound. In contrast to the other samples, that of applied to the pellet D shows stability under reducing atmosphere (9% H_2 in N_2). The conductivity of the pellet D reaches the value of $8.58\cdot10^{-6}$ S cm^{-1} at 240 °C and remains almost constant at this value up to 317 °C. The conductivity of the pellet D shows a value of $5.41\cdot10^{-5}$ S cm^{-1} at 317 °C and then it starts to decrease as a function of operating time. This behavior may be attributed to the pretreatment process for the pellet D is not long enough to dehydrate $RbH(PO_3H)\cdot Te(OH)_6$ compound totally.

Conductivity measurements are in an agreement with DTA and DSC data. It has been reported previously superprotonic phase transitions in $MH(PO_3H)$ compounds only occur for samples that exhibit a monoclinic structure [23]. Amorphous $RbH(PO_3H)\cdot Te(OH)_6$ does not show any superprotonic conductivity.

Plots of conductivity (i.e. log(σ) versus 1/T) for all pellets are given in Figure 3.12. The average conductivity values are given for each temperature. The conductivities of all pellets increase by increasing temperature up to 176 °C. Above that temperature, the pellets B and D keep increasing in the conductivity up to 240 and 317 °C, respectively, while the pellets A, and C started decreasing up to 280 °C. The conductivities of all pellets except for the pellet A shows an increase at 317 °C. The pellet C, however, shows an unexpected rise in the conductivity at that temperature.

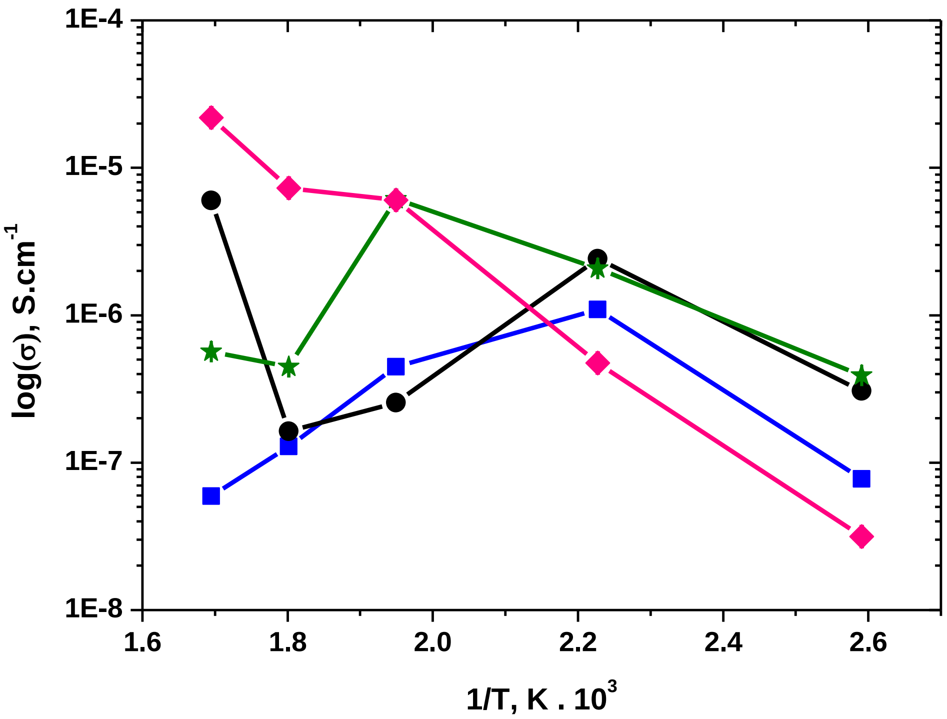

Figure 3.12 Plot of conductivity (log(σ) versus 1/T) for ■ the pellet A, ★ the pellet B, ● the pellet C and ◆ the pellet D. The average conductivity values are given for each temperature. The pellets A and B were tested respectively with platinum-carbon and gold electrodes for 135 hours between 113 to 317 °C. The pellet C (earlier investigated at various temperatures up to 176 °C for 360 hours) and the pellet D (heated up to 450˚C and then cooled down to room temperature prior to the measurement) were tested with gold electrodes under the same conditions as used for the pellets A and B.

3.3.3 Calculations of the Equivalent Capacity

Calculation of the equivalent capacity, C_{ω}, defined by (2.2) [60]. The average equivalent capacities were calculated for each temperature and their temperature dependence is given in Figure 3.13. The equivalent capacities of the pellets A, B and C show similar behavior by increasing temperature and their capacities remains almost constant with change of temperature. The pellet C, however, shows an increase in the equivalent capacity at 317 °C. On the contrary, the equivalent capacity of the pellet D generally shows a decrease by increasing temperature. Similar equivalent capacitances were calculated for the pellets A, B and C. The pellet C, however, shows an increase in the equivalent capacity at 317 °C upon the completion of the dehydration. The pellet D, which is not completely dehydrated after a two-hour heat treatment at 450 °C, shows a different behavior upon changes in temperature as compared to the other pellets.

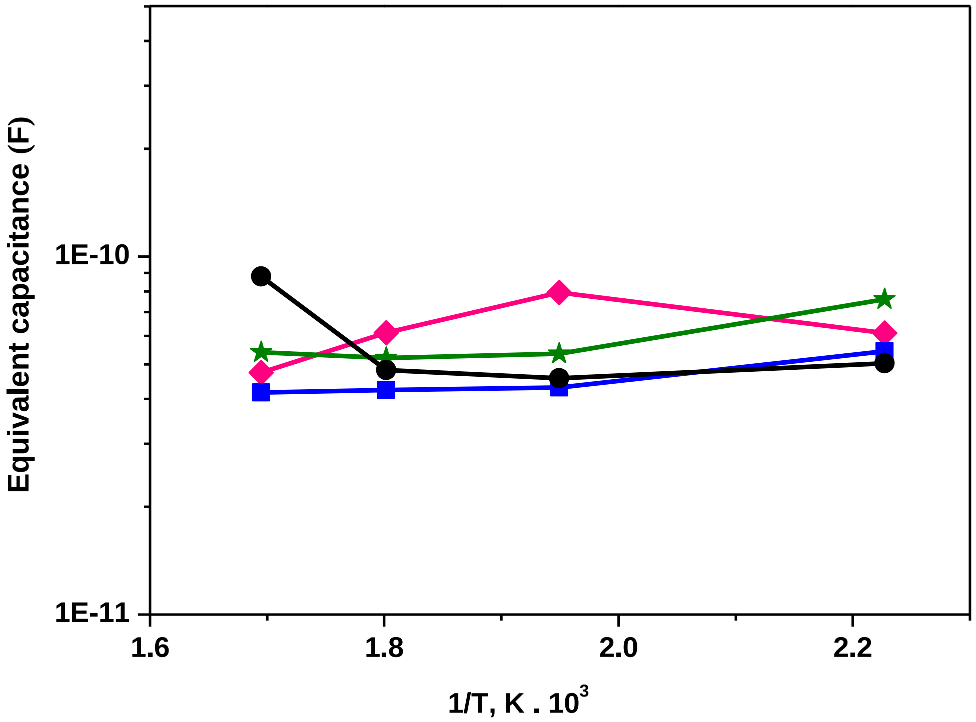

Figure 3.13 Plot of equivalent capacitances versus 1/T for ■ the pellet A, ★ the pellet B, ● the pellet C and ◆ the pellet D. The average equivalent capacitance values are given for each temperature. The pellets A and B were tested respectively with platinum-carbon and gold electrodes for 135 hours between 113 to 317 °C. The pellet C (earlier investigated at various temperatures up to 176 °C for 360 hours) and the pellet D (heated up to 450 °C and then cooled down to room temperature prior to the measurement) were tested with gold electrodes under the same conditions as used for the pellets A and B.

The results shown in Figure 3.14 demonstrate that $RbH(PO_3H)\cdot Te(OH)_6$ powder does not undergo a phase transition upon heating. This observation is further confirmed by differential scanning calorimetry as given in Figure 3.6.

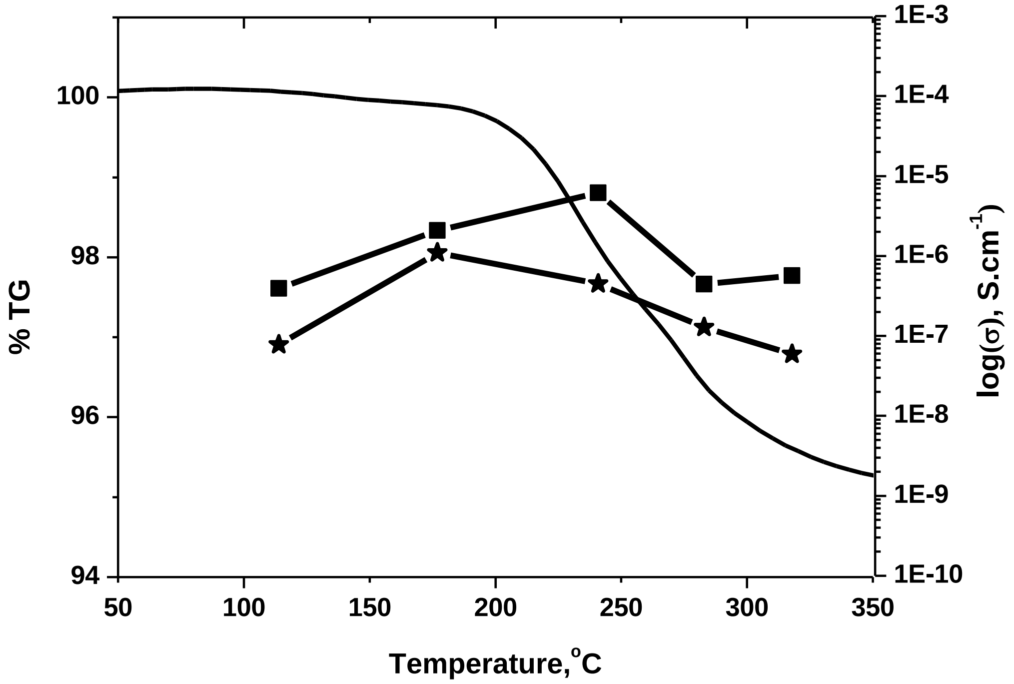

Figure 3.14 Plot of conductivity log(σ) and thermal behavior TG% versus temperature for $RbH(PO_3H)\cdot Te(OH)_6$ (■ pellet A, ★ pellet B) The pellets A and B were tested respectively with platinum-carbon and gold electrodes for 135 hours between 113 to 317 °C.

3.4 Conclusions

The $RbH(PO_3H)\cdot Te(OH)_6$ compound forms in an amorphous and crystalline structure. Unlike monoclinic phosphites, super protonic conductivity is not seen in this rubidium phosphite tellurate compound. The conductivity of the compound decreases during dehydration, as expected, and average conductivity values of $5.91\cdot10^{-8}$ and $5.67\cdot10^{-7}$ S cm^{-1} are obtained for the pellets A and B at 317 °C, respectively. It shows that the electrode contribution, as the ohmic resistance associated with the pellet A has not been subtracted.

The pellet C shows a jump in the conductivity at 317 °C (from $2.09\cdot10^{-6}$ S cm^{-1} to $9.9\cdot10^{-6}$ Scm^{-1}). Although all pellets were treated under the same conditions, the pellet C was investigated up to 176 °C for 360 hours prior to the experimentation. Due to the effect of operating time on dehydration, a new compound, $Rb_2H_2P_2O_5\cdot[Te(OH)_6]_2$, occurs by the dehydration of the pellet C at 317 °C. The conductivity of the pellet C reaches $9.9\cdot10^{-6}$ S cm^{-1} at that temperature. Dehydration is not usually responsible for increasing conductivity. This increase in the conductivity is due to the fact that the monoprotic $RbH(PO_3H)$ part of $RbH(PO_3H)\cdot Te(OH)_6$ becomes a diprotic $Rb_2H_2P_2O_5$ part of $Rb_2H_2P_2O_5\cdot[Te(OH)_6]_2$ compound by dehydration. The dehydrated compound has also a higher hydrogen density relative to the starting compound. For that reason, it can be assumed that the dehydration of the $RbH(PO_3H)\cdot Te(OH)_6$ enhances the conductivity. The measurements done with the pellet D, dehydrated $RbH(PO_3H)\cdot Te(OH)_6$ prior to measurement, support that the dehydrated compound have a conductivity of $5.41\cdot 10^{-5}$ S cm^{-1} at 317 °C. Moreover, it is seen that a dehydrated compound shows stability against operating time and temperature changes up to 317 °C. The decrease in conductivity of the pellet D at 317 °C may be attributed to the fact that the pretreatment process for the pellet D is not long enough to reach the complete dehydration.

CHAPTER 4

RUBIDIUM SELENATE with a SECONDARY PHASE of RbOH

In this chapter, the high temperature properties of Rb_2SeO_4 were studied by calorimetry, impedance spectroscopy and X-ray powder diffraction. The synthesized Rb_2SeO_4 included a second phase of Rb_2SeO_3, which could be eliminated upon heating the compound. As expected, no conductivity was seen in dry ($pH_2O<0.001$ bar) air. By changing the dry air to humidified ($pH_2O=0.1$ bar) air at 176 ˚C, the conductivity increased sharply, rising from $8.64\cdot10^{-8}$ S cm^{-1} to $1.73\cdot10^{-6}$ S cm^{-1}. Under humidified ($pH_2O=0.1$ bar) reducing atmosphere (9 %H_2 in N_2), the conductivity increased to $2.01\cdot10^{-4}$ S cm^{-1} at 317 °C. Decompositions of Rb_2SeO_3 and Rb_2SeO_4 to RbOH, which is known as a proton conductor, are responsible for the obtained conductivity in humidified atmospheres. This event may be an approach to explain the conductivity rise in solid acid electrolytes, including sulfate and selenate groups, around their decomposition temperatures in humidified atmospheres.

4.1 Introduction

Rubidium selenate, Rb_2SeO_4, belongs to a family of A_2BX_4-type (X = Br, Cl and O) compounds with the β-K_2SO_4 type structure [87-89]. The crystal structure of β -K_2SO_4 is well established: it crystallizes in the orthorhombic space group Pnma (62) and all atoms (except for the oxygen atoms occupying the 8d sites) lie on the two crystallographic mirror planes within the unit cell (on 4c sites, at y=1/4, 3/4). However, at higher temperatures (about 587 °C) a first order phase transition of β-K_2SO_4 to α-K_2SO_4 occurs. The high-temperature phase belongs to the hexagonal space group $P6_3/mmc$ [89]. The above structures all contain SeO_4 or SO_4 tetrahedral anions.

Some data related to the thermal decomposition of rubidium selenate in air have already been reported. Gattow [90] studied the crystal structure and the thermal decomposition of Rb_2SeO_4 and reported that the β→α transition of Rb_2SeO_4 occurs at 552 °C on heating. Shigematsu et al. [87] performed heat capacity, X-ray scattering and neutron scattering experiments on Rb_2SeO_4, confirming an anomaly due to the phase transition at 548 °C. On the other hand, under humidified reducing atmosphere, Rb_2SeO_4 may decompose to SeO_2 and RbOH; the latter of which is known as a proton conductor [91]. The solid hydroxides of the alkali metals, Na, K, Rb and Cs undergo a transition from a monoclinic (NaOH, KOH, RbOH) or orthorhombic (CsOH) to a cubic structure. This cubic high-temperature phase of RbOH with free-rotating OH^- ions enhances electrical conductivity caused by a Grotthus-type conduction mechanism [92-94]. Haas and Schindewolf [92] reported that RbOH has a conductivity of 10^{-6} to 10^{-5} S cm^{-1} below 223 ˚C and at the phase transition temperature (235 ˚C), conductivity increases to 10^{-4} S cm^{-1}. This conductivity further rises steeply up to 10^{-1} S cm^{-1} from 335 ˚C to the melting point of 392 ˚C. The paper presents synthesis, structural, thermal and electrical studies of Rb_2SeO_4 with a secondary phase of RbOH.

4.2 Experimental

26.6 mmol rubidium carbonate (99.8%, Sigma-Aldrich) was dissolved in approximately 20 ml distilled water. After stirring for 3 hours, about 7 ml selenic acid (40 wt. % H_2O, 99.95% Sigma-Aldrich) was slowly added to the rubidium carbonate solution at room temperature. Rb_2SeO_4 powder was obtained by slow evaporation of the solution continuously at approximately 50 °C for 2 days. The powder was dried in an oven in air at about 200 °C for two weeks prior to experiments.

Scanning Electron Microscopy and Energy Dispersive X-ray Spectroscopy analysis were done using a Zeiss Evo 60. EDS data were analyzed using the *NSS 2.2 X-ray MicroAnalysis* program. Phase identification was carried out by X-ray powder diffraction analysis on a Bruker D8 diffractometer with Cu Kα radiation. Soller slits and a programmable horizontal slit were used on the primary beam (illuminated width 6 mm). Diffracted radiation was analyzed with a *Lynx-Eye Bruker PSD* covering 2.5 degree. A Ni filter was used on the secondary side. Experiments were performed both at ambient and elevated temperatures (by 50 °C intervals up to T= 600 °C) in dry air. A high temperature chamber with Kapton windows (MRI, Karlsruhe) with a platinum heater foil was used. Collected data were analyzed using the *STOE Win XPOW 2.20* program.

Thermal analysis (TG, DTA and DSC) were carried out using TG-DTA system (Netzsch STA 409 CD) and Netzsch DSC 200 F3 with a heating rate of 5 °C min^{-1}. While TG analysis was performed in both air and reducing (gas mixture of 9% H_2 in N_2) atmospheres from room temperature to 500 °C, DTA analysis was just performed in reducing atmosphere. In order to determine the phase transition of Rb_2SeO_4 more accurately, DSC analysis was measured in two heating/cooling cycles in air from room temperature up to 650 °C with a scan rate of 5 °C min^{-1}. Samples were ground in an agate mortar prior the measurements.

Conductivity measurements were performed using electrochemical impedance spectroscopy. Two pellets were produced by pressing Rb_2SeO_4 powder into discs of about 1 mm thickness and 8 mm diameter at 200 MPa pressure. The pellets were sintered at 200 °C during two weeks. This processing was applied to eliminate, as much as possible, the water content in the sample and to obtain dense pellets. The pellets were equipped with gold electrodes, sputtered on both sides of the pellets. Both pellets were investigated from 113 °C to 317 °C for 135 hours. The measurements were done under dry air ($pH_2O<0.001$ bar), humidified air ($pH_2O=0.1$ bar) and humidified gas mixture of 9% H_2 in N_2 ($pH_2O=0.1$ bar). The gases were humidified by bubbling the gas through a heated water bottle ($T(H_2O)=46$ °C). Impedance spectra were recorded under flowing gases (50 mL/min) using a Solartron 1260 frequency analyzer in both measurement series. An excitation voltage of 20 mV was used, with no applied dc bias. The temperature of measurements was increased stepwise with heating rates of 5 °C min^{-1}. Measurements were carried out over the frequency range of 1 MHz to 1 Hz. Data analysis was done using the software *ZSimpWin 3.21,* supplied by Princeton Applied Research.

4.3 Results and Discussions

4.3.1 Structural and Thermal Analysis

The reaction for synthesis of Rb_2SeO_4 is:

$$Rb_2CO_3 + H_2SeO_4 \rightarrow Rb_2SeO_4 + CO_2 + H_2O \tag{4.1}$$

Synthesis with slow evaporation resulted in Rb_2SeO_4 particles with diameters in the range of 1 to 30 μm. Figure 4.1(a) illustrates a SEM micrograph of the synthesized powder. It is seen that smaller particles tend to form agglomerates. A cross section SEM image of the Rb_2SeO_4 pellet is shown in Figure 4.1(b). Lighter regions of the SEM image indicate presence of a second phase in the Rb_2SeO_4. Figure 4.2 gives a typical EDS spectrum, which shows that the powder consist of the expected elements. Figure 4.3 shows the results of 5 EDS point analyses on the surface of the powder, which shows a variation of elements for different points. Referring to Figure 4.3, the difference in composition (atomic %) of the synthesized Rb_2SeO_4 compound that is seen for each point investigated by EDS analysis may be attributed to variation of the chemical composition across the sample rather than topographical effect. This is in agreement with the cross section SEM results. The second phase in the compound might be Rb_2SeO_3 and formed due to the reaction of rubidium carbonate with selenious acid (4.2). Since selenic acid is a very powerful oxidizer and has been purchased as 40 wt. % in H_2O, H_2SeO_4 might be reduced to H_2SeO_3 (4.3). The 5 EDS point analysis also supports the presence of Rb_2SeO_3 structure in the compound.

$$Rb_2CO_3 + H_2SeO_3 \rightarrow Rb_2SeO_3 + CO_2 + H_2O \tag{4.2}$$

$$SeO_4^{2-} + 2H_3O^+ \leftrightarrow H_2SeO_3 + 2H_2O + \tfrac{1}{2}\,O_2 \tag{4.3}$$

In literature, it has been reported that a very small amount of Rb_2SeO_3 undergoes disproportionation with formation of elemental selenium at 180 °C, in air. That elemental selenium gives a reddish color to the sample when it is absorbed on the surface [95]. The synthesized compound also becomes reddish in color when it is dried at about 200 °C in air and this event may be attributed to the presence of Rb_2SeO_3.

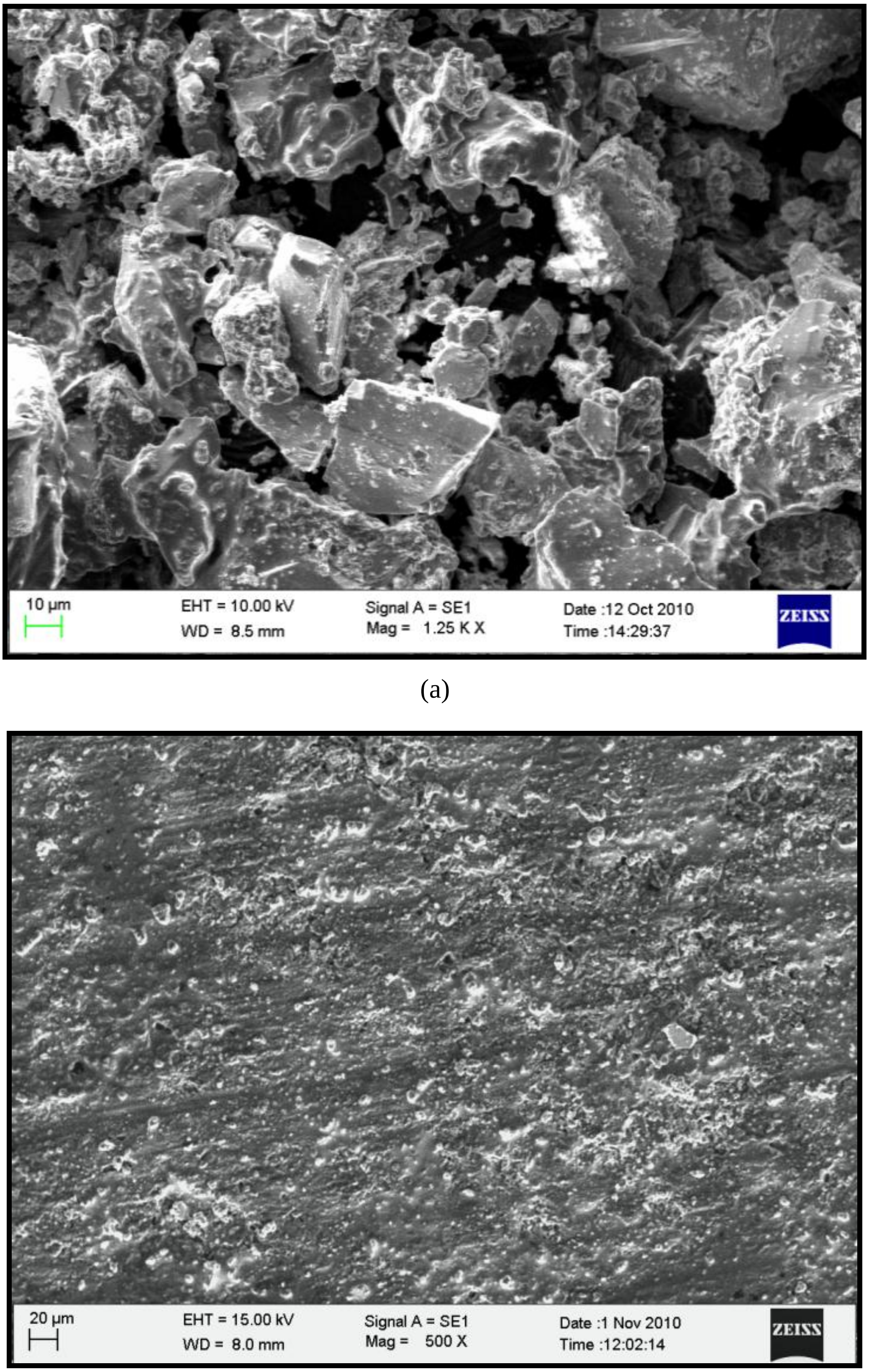

(a)

(b)

Figure 4.1 (a) SEM image of the synthesized Rb_2SeO_4 powder, X1250; (b) cross section SEM image of Rb_2SeO_4 pellet, X500

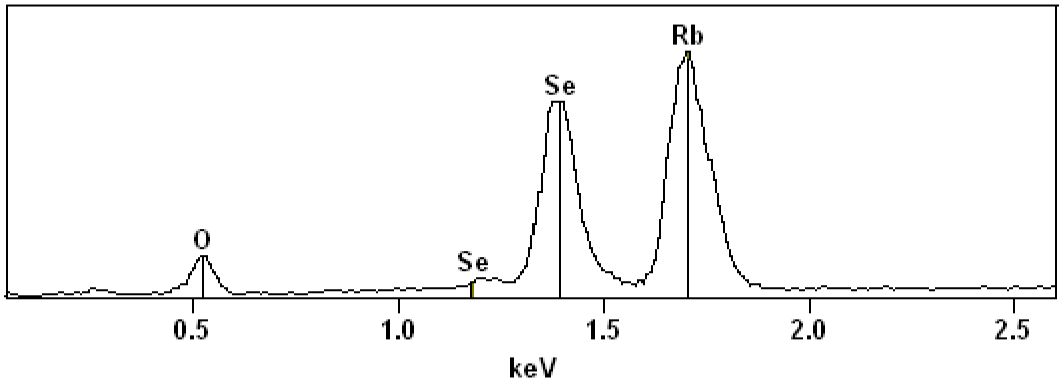

Figure 4.2. EDS spectrum showing typical composition of the synthesized Rb_2SeO_4 powder

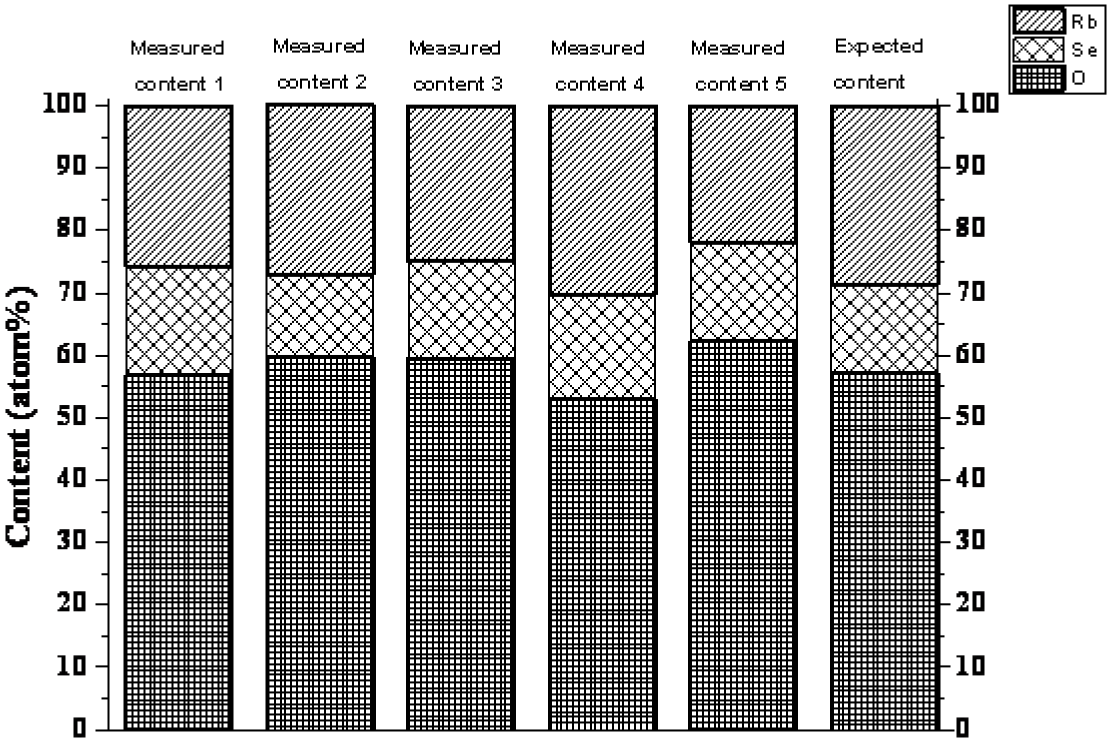

Figure 4.3 Point analysis showing distribution of detectable elements at five different points on the surface of the synthesized Rb_2SeO_4

Figure 4.4 gives thermal analysis of the compound under both air (Figure 4.4 (a,b)) and humidified ($pH_2O=0.1$ bar) reducing atmosphere (9% H_2 in N_2) (Figure 4.4 (c,d). As seen in Figure 4.4 (d), an exothermic peak on heating cycle and this exothermic reaction continues down to 550 °C while cooling from a maximum temperature of 600 °C.

As expected, Rb_2SeO_4 decomposes to RbOH and SeO_2 under reducing atmosphere with the following two-step reaction (4.4 and 4.5):

$$Rb_2SeO_4 + H_2 \rightarrow Rb_2SeO_3 + H_2O \tag{4.4}$$

$$Rb_2SeO_3 + H_2O \leftrightarrow 2RbOH + SeO_2 \tag{4.5}$$

Above 400 °C, reaction shifts to the right due to sublimation of SeO_2. Referring to Figure 4.4 (a,c), mass loss of 6-8 wt.% at 500 °C is seen under both air and reducing atmospheres. As given with (4.5), impurity of Rb_2SeO_3 in the compound reacts with moisture in air to form RbOH and SeO_2. Due to the synthesized compound being kept at 200 °C prior to the analysis, some amount of Rb_2SeO_3 in the compound might be converted into RbOH and SeO_2 when it was exposed to ambient temperature. Moreover, this conversion can be responsible for the observed conductivity observed by changing the atmosphere from dry air to humidified air.

In order to determine the phase transitions more accurately, DSC analysis of the Rb_2SeO_4 was performed. Figure 4.5 (a,b) show the DSC analysis performed from room temperature to 500 °C, which shows a peak around 260 °C in the first heating and cooling cycles. In the second heating/cooling cycle, the peak shifts to 335 °C on heating and to 220 °C on cooling. It is therefore likely a thermal events relating to the crystallographic change of RbOH. Figure 4.5(c and d) demonstrate another DSC measurement done from room temperature to 650 °C to confirm the transition of orthorhombic Rb_2SeO_4 to the hexagonal phase. A sharp peak was observed at 549 °C in both heating/cooling cycles. Thus, the observed transition temperature is in close agreement with the previously reported values of 545 °C [89], 548 °C [87] and 552 °C [90]. Moreover, as seen in Figure 4.5 (d), no other peak except for the phase transition peak of Rb_2SeO_4 was seen in the second heating/cooling cycle. It is obvious that the second phase of Rb_2SeO_3 in the compound was totally converted into Rb_2SeO_4 upon heating above the phase transition temperature of Rb_2SeO_4.

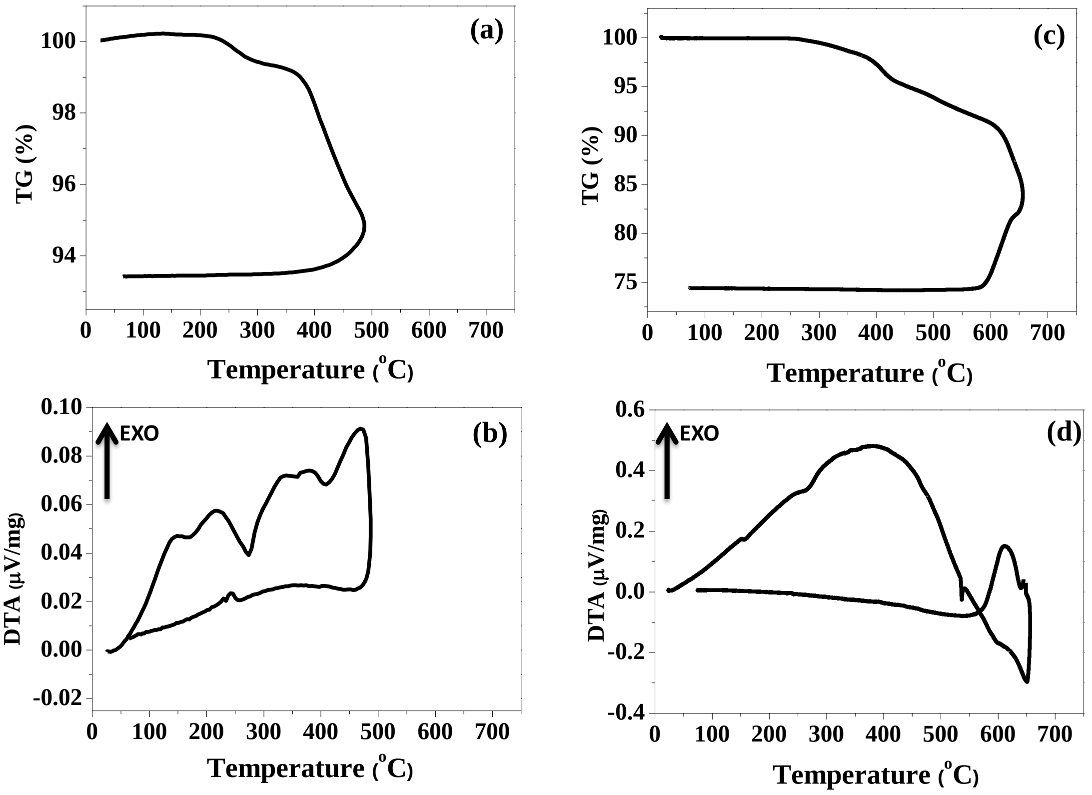

Figure 4.4 TG/DTA analysis of the synthesized Rb_2SeO_4 under (a,b) air and (c,d) 9 % H_2 in N_2. For both experiments, the scan rate was 5 °C min^{-1}

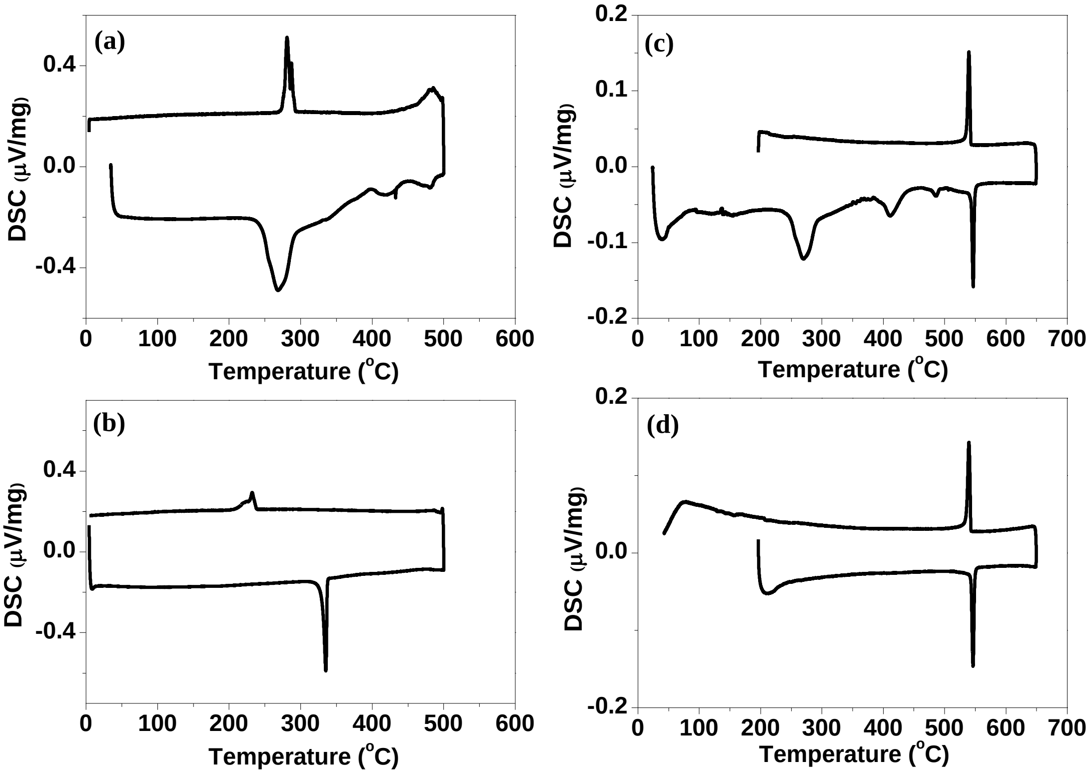

Figure 4.5 DSC analysis of the synthesized Rb_2SeO_4 under air at a scan rate of 5 °C min^{-1}; (a) first and (b) second heating/cooling cycles up to 500 °C, (c) first and (d) second heating/cooling cycles up to 650 °C

XRD patterns were obtained at both ambient and elevated temperatures. HT-X-ray diffraction was performed on the compound in flowing dry air up to 600 °C (by 50 °C intervals). Figure 4.6(a) shows the XRD pattern of the synthesized powder, which compares well to the orthorhombic Rb_2SeO_4 phase (# 24-966 in the JCPDS database, Pnma = Space Group 62) with lattice constants of a=7.979, b=10.82 and c= 6.174 Å. This structure is isostructural with K_2SeO_4 and β-K_2SO_4 Figure 4.6(b) illustrates the XRD pattern of the powder heated up to 600 °C and then cooled down to room temperature. The patterns at room temperature before heating and that after heating to 600 °C are identical as to peak positions, apart from a small instrumental 2 theta shift. Such a shift is usually ascribed to a slight movement up or down of the filament during heating/cooling. Therefore, it may be assured that no chemical decomposition had taken place. Figure 4.6(c) shows the room temperature XRD pattern of the Rb_2SeO_4 pellet after the conductivity measurement. It is seen that Rb_2SeO_4 began to decompose after conductivity measurements under reducing atmosphere. This result conforms to that obtained from the TG/DTA analysis under the same conditions.

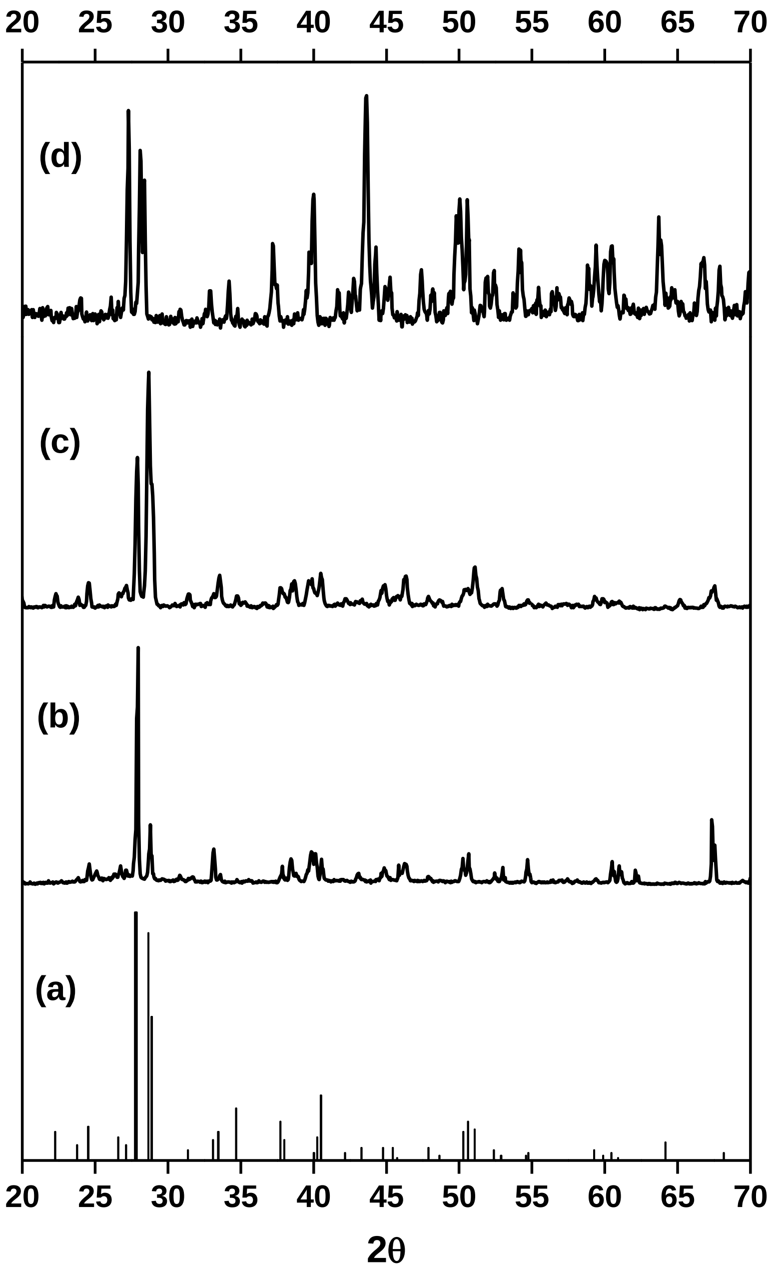

Figure 4.6 XRD diagrams of (a) Rb_2SeO_4 pattern (# 24-966 in the JCPDS database), (b) the synthesized powder, (c) the powder heated up to 600 °C and then cooled down to room temperature, (d) the tested pellet with gold electrodes for 135 hours between 113 to 317 °C

Figure 4.7 represents the HT-XRD patterns of the synthesized Rb_2SeO_4. The observed relative peak heights deviate from those in the rubidium selenate reference. This can be ascribed to texture and/or development of different facets in the sample under test and in the reference. Crystal growth may also occur during heating to 600 °C. Moreover, a doublet develops at 300 °C but disappears again at elevated temperatures. It may be due to the second phase of Rb_2SeO_3 in the compound. It has already been reported that a stepwise oxidation begins at about 310 °C and leads to the formation of a product whose composition corresponds to the formula $Rb_2SeO_3 \cdot 3Rb_2SeO_4$ and Rb_2SeO_3 is converted into the selenate at 400 °C [73]. Furthermore, another doublet develops at 550 °C, which is in agreement with the transition of orthorhombic Rb_2SeO_4 to the hexagonal phase. When all the results are taken into account, it can be concluded that the synthesised powder includes a second phase of Rb_2SeO_3, which decomposes to RbOH and SeO_2 under humidified atmosphere. However, this second phase of Rb_2SeO_3 can easily be eliminated upon heating above the phase transition temperature of Rb_2SeO_4.

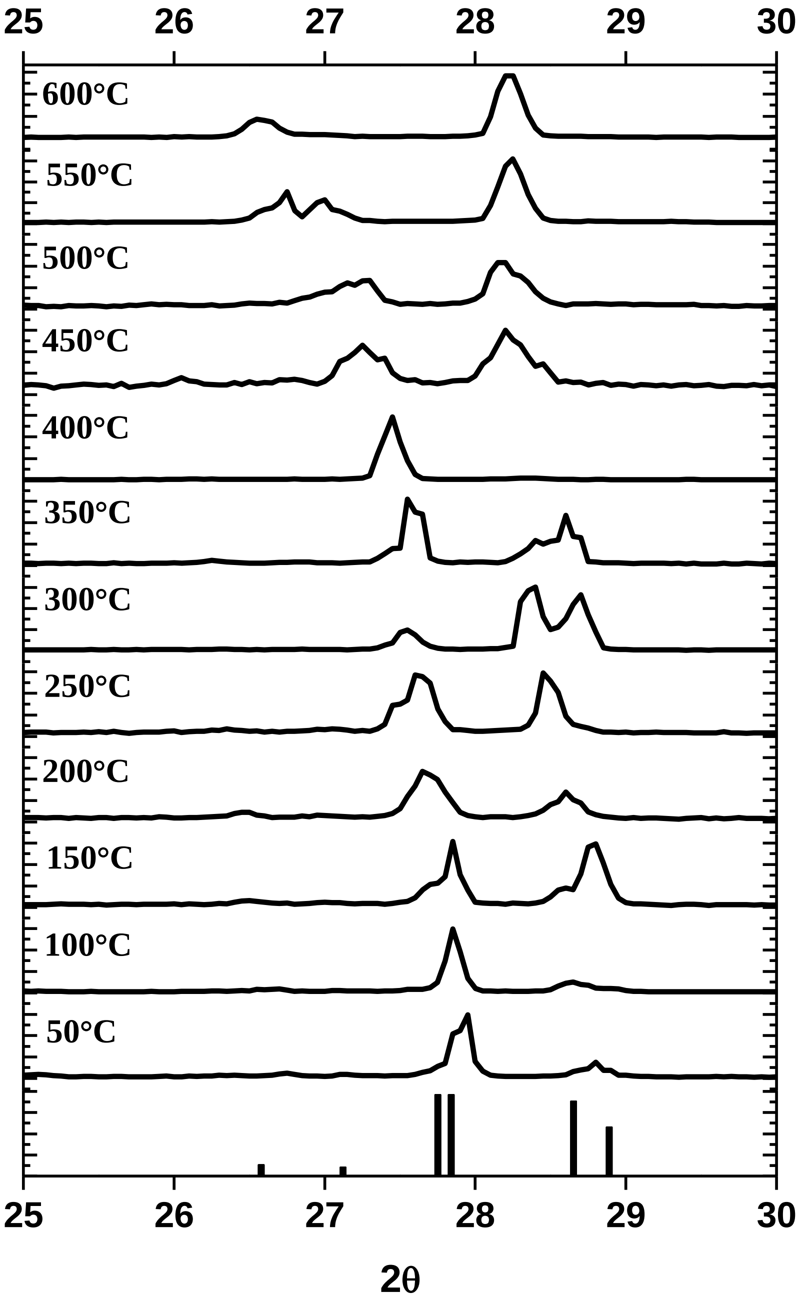

Figure 4.7 HT-XRD diagrams of the synthesized Rb_2SeO_4 powder

4.3.2 Electrochemical Impedance Spectroscopy

Both pellets were tested in the temperature range of 113 °C to 317 °C. At each temperature, similar impedance spectra and conductivities were obtained for both pellets. As expected, no conductivity was measured for the pellets at 113 °C under dry air ($pH_2O \leq 0.001$ bar). Changing the atmosphere from dry air to humidified air

(pH_2O=0.1 bar) at the same temperature, a very low conductivity ($\leq 10^{-9}$ S cm^{-1}) was measured. Figure 4.8 gives a comparison of the conductivity results for the pellets tested in the temperature range of 176 to 317 °C. As seen in Figure 4.8, the conductivity of the pellets increases from ca. $9 \cdot 10^{-8}$ S cm^{-1} to ca. $2 \cdot 10^{-6}$ S cm^{-1} in humidified air at 176 °C. The conductivity increases further when changing the gas from humidified air to humidified gas mixture of 9 % H_2 in N_2 (pH_2O=0.1 bar) reaching a value of ca. 10^{-5} S cm^{-1} at that temperature. The pellets investigated for 12 hours at 176 °C in humidified air show an increase in the conductivity with time. However, the conductivity decreases when the pellets are held in humidified gas mixture of 9% H_2 in N_2.

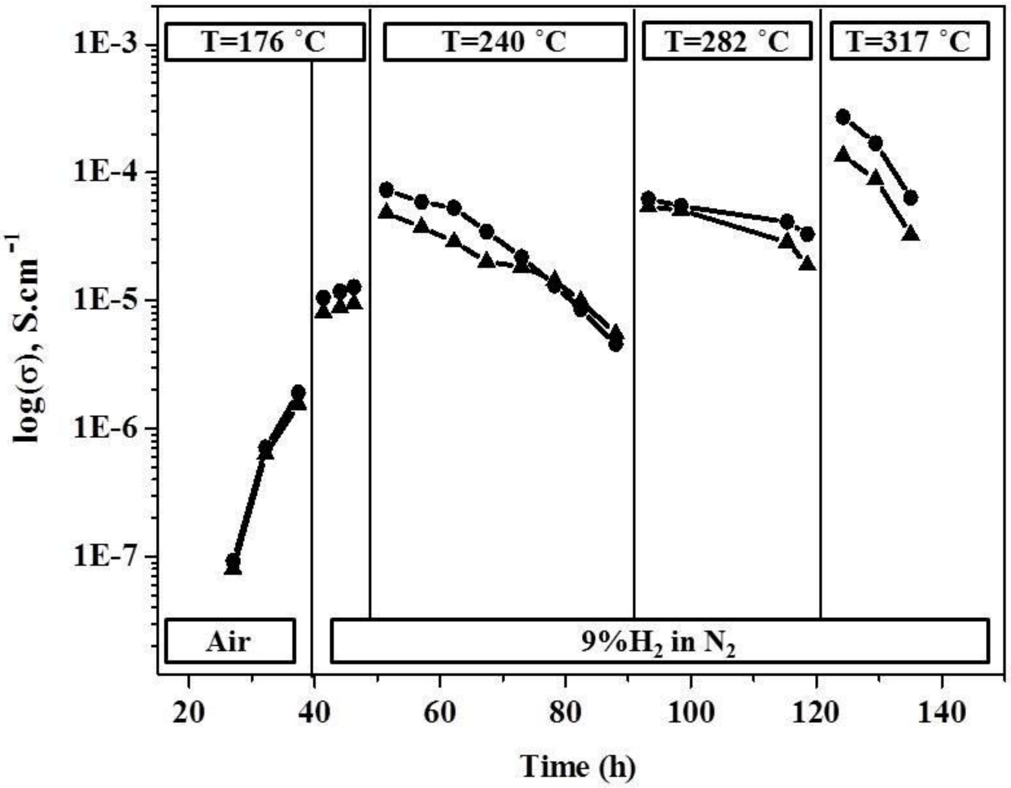

Figure 4.8 Plot of conductivity log(σ) versus time for ● the first and ▲ the second pellets at various temperatures and atmospheres. Both pellets were tested with gold electrodes under the same conditions

Figure 4.9 shows the rig before and after the measurement. It seems some amount of selenium is adsorbed on the platinium current collectors and this causes the poisoning.

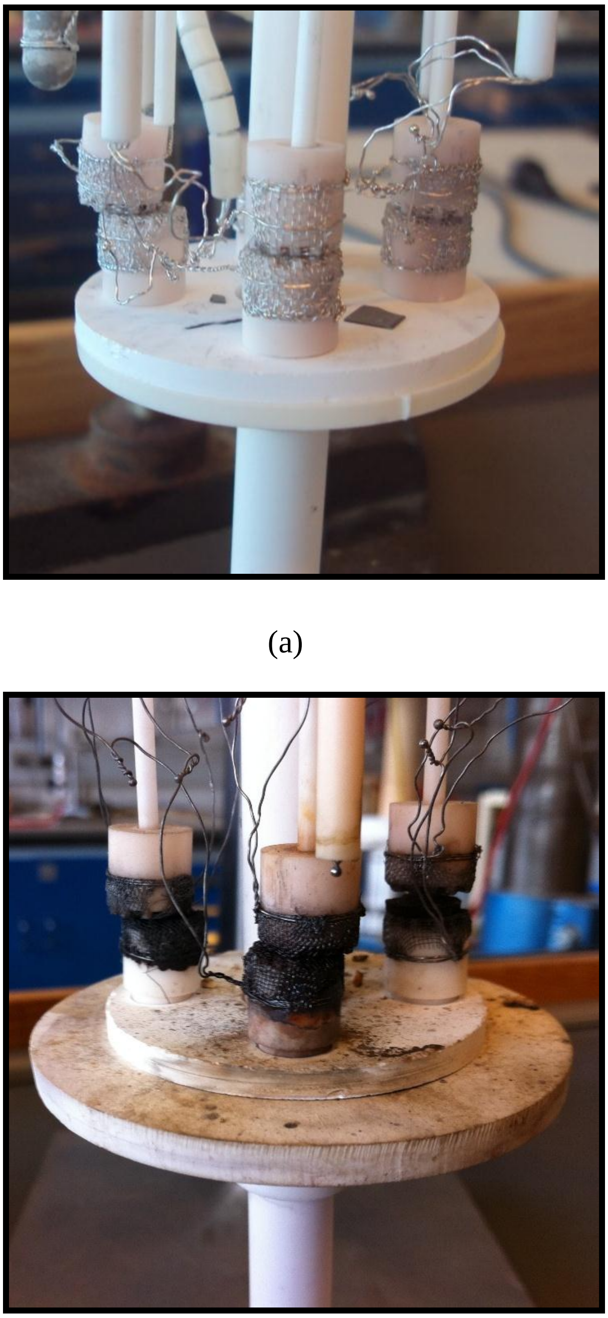

(a)

(b)

Figure 4.9 The rig used in the experiments; (a) pre-test, (b) post-test

Plots of conductivity log (σ) versus 1/T for the pellets are given in Figure 4.10. The average conductivity values are given for each temperature in humidified gas mixture of 9 % H_2 in N_2. It is clear that the conductivities of the pellets increase by increasing temperature.

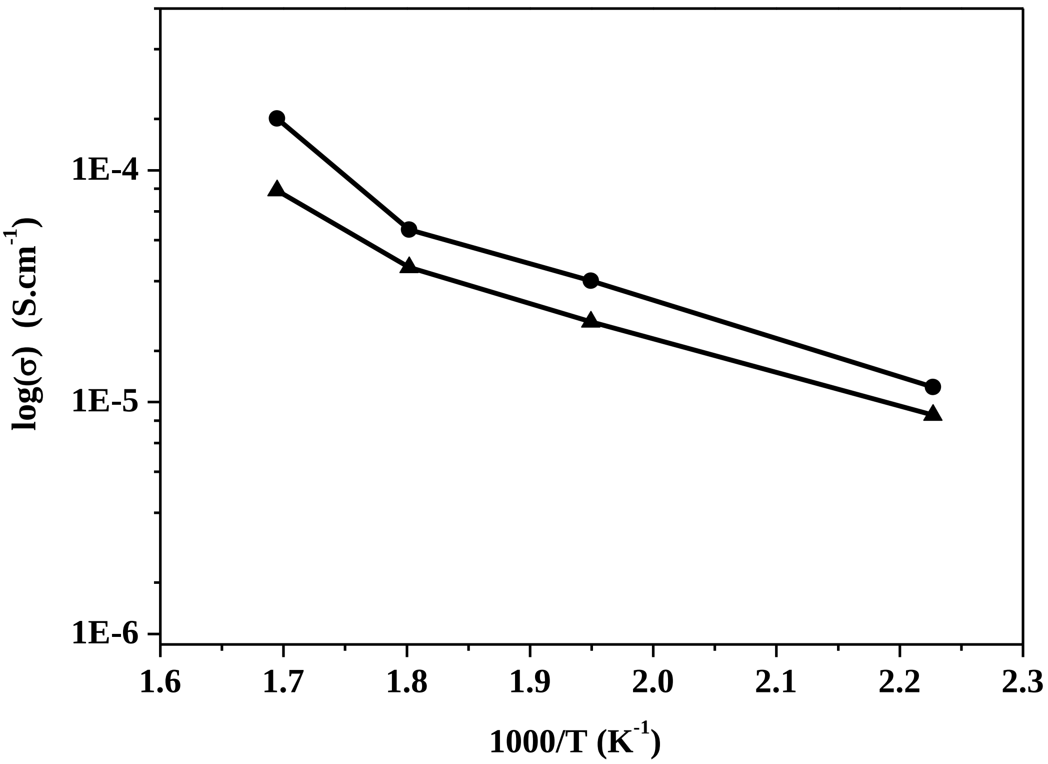

Figure 4.10 Plot of conductivity log(σ) versus 1/T for two pellets of Rb_2SeO_4, tested with gold electrodes under the humidified gas mixture of 9%H_2 in N_2

Conversion of Rb_2SeO_4 into RbOH is necessary to achieve conductivity and this conversion can be obtained under reducing atmosphere. Conversion of the second phase of Rb_2SeO_3 into RbOH is responsible of the obtained conductivity in humidified air. The obtained conductivity values of $1.11 \cdot 10^{-5}$ S cm^{-1} at 176 °C and $6.07 \cdot 10^{-5}$ S cm^{-1} at 240 °C are also close agreement with those of RbOH, which were reported as 10^{-6}-10^{-5} S cm^{-1} below 223 °C, ca. 10^{-4} S cm^{-1} at 230 °C [92].

Figure 4.11 illustrates typical impedance spectra obtained in the temperature range of 176 °C to 317 °C. No spectra were obtained in dry air. As expected, the spectra became measurable with humidification of the air. Figure 4.11(a) gives the impedance spectrum at 176 °C in humidified air, while Figure 4.11(b) shows that in humidified gas mixture of 9% H_2 in N_2. It is seen that the resistance of the compound decreased by changing the atmosphere from humidified air to humidified reducing gas mixture. Figure 4.11(c) presents the impedance spectra obtained at 240, 282 and 317 °C in humidified gas mixture.

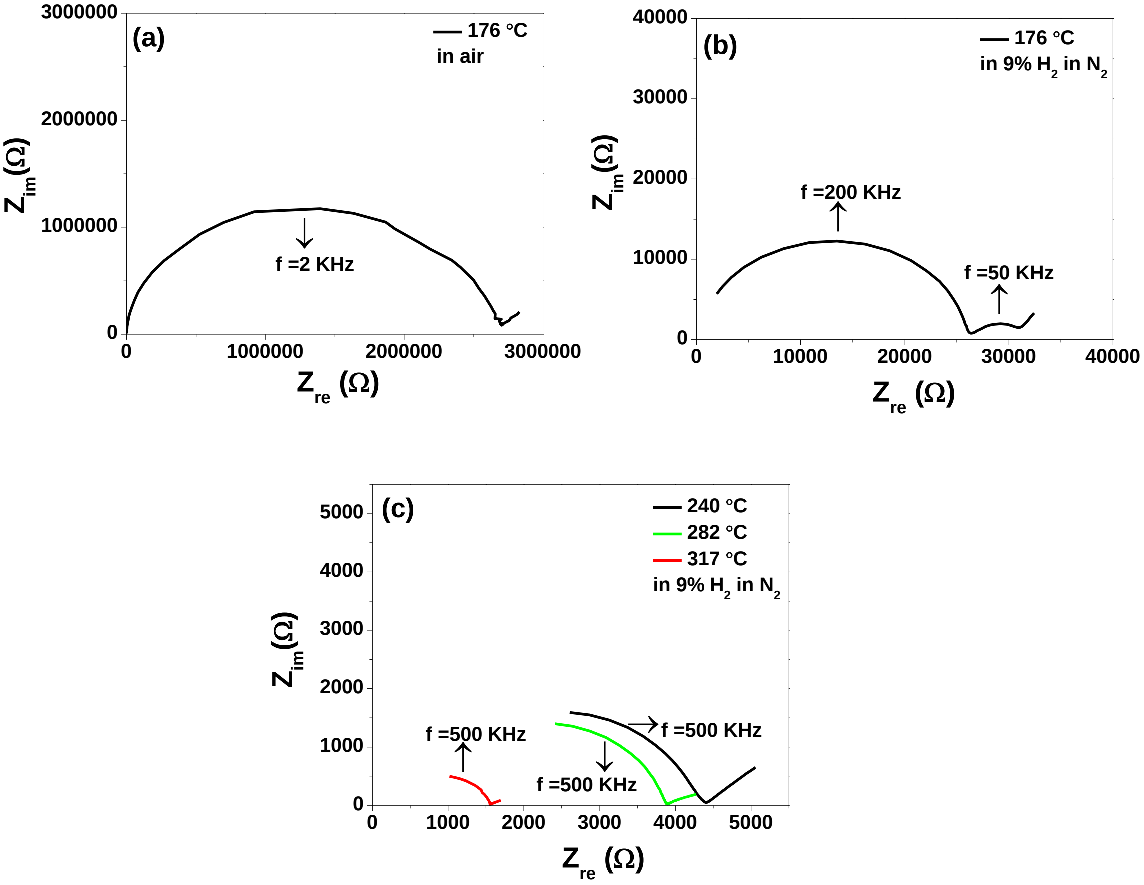

Figure 4.11 Impedance spectra of the Rb_2SeO_4 pellet at (a) 176 ˚C in air, (b) 176 ˚C in gas mixture of 9% H_2 in N_2, (c) 240, 282 and 317 ˚C in gas mixture of 9% H_2 in N_2

4.4 Conclusions

Rb_2SeO_4, as prepared from Rb_2CO_3, was crystalline and contained a second phase of Rb_2SeO_3, which could be eliminated by heating the compound above the phase transition temperature (549 °C). Decompositions of Rb_2SeO_3 and Rb_2SeO_4 to RbOH, known to be a proton conductor, provided protonic conductivity in humidified atmospheres. With time, the conductivity increased from $8.64 \cdot 10^{-8}$ S cm^{-1} to $1.73 \cdot 10^{-6}$ S cm^{-1} at 176 °C in humidified air. By changing the atmosphere from humidified air to humidified gas mixture of 9 % H_2 in N_2, the conductivity reached a value of $1.11 \cdot 10^{-5}$ S cm^{-1} at that temperature. The obtained conductivity values of $1.11 \cdot 10^{-5}$ S cm^{-1} at 176 °C and $6.07 \cdot 10^{-5}$ S cm^{-1} at 240 °C were also in a close agreement with those previously reported as 10^{-6}-10^{-5} S cm^{-1} below 223 °C and 10^{-4} S cm^{-1} at 230 °C for RbOH [92]. In our experiments, the highest conductivity value of $2.01 \cdot 10^{-4}$ S cm^{-1} was observed at 317 °C. This conductivity value may further increase upon heating, as reported that the conductivity of RbOH reaches to very high levels as about 10^{-1} S cm^{-1} up to melting point of RbOH (382 °C).

It can be concluded that the formation of RbOH by decompositions of Rb_2SeO_4 provided the protonic conductivity and this conductivity increased by increasing temperature. In a previous study, it was reported that upon heating $Rb_3H(SO_4)_2$ under moderate humidification levels, it decomposed to Rb_2SO_4 and showed a rise in the conductivity [73]. As Rb_2SO_4 would not be expected to display particularly high conductivity, the researchers concluded that the second decomposition product, identified as $Rb_mH_n(SO_4)_p$ (with $p=(m+n)/2$), must be responsible for the rise in the conductivity. However, the second decomposition product may also be Rb_2SO_4 or/and Rb_2SO_3. Since sulfur and selenium compounds have very similar chemical properties; formation of RbOH by decompositions of Rb_2SO_4 or/and Rb_2SO_3 under humidified atmospheres can be responsible for the rise in the conductivity at decomposition temperature. This fact may be an approach to explain the conductivity rise in solid acid electrolytes, including sulfate and selenate groups, around their decomposition temperatures in humidified atmospheres.

CHAPTER 5

CESIUM DIHYDROGEN PHOSPHATE TELLURITE GLASS

In this chapter, a new cesium dihydrogen phosphate-tellurite (CsH_2PO_4-TeO_2) glass was studied. CsH_2PO_4-TeO_2 glass was synthesized and chracterized for the first time. The high conductivity value of $2\cdot10^{-2}$ S cm^{-1} was observed at 240 ºC. This high conductivity was kept in the wide temperature range of 240 ºC to 348 ºC. This wide operating remperature provide ability to CsH_2PO_4-TeO_2 glass to be used as electrolyte in low and intermediate temperature SOFCs. It is obvious that TeO_2 addition into CsH_2PO_4 is significantly effective in enhancing the thermal stability of the CsH_2PO_4.

5.1 Introduction

Cesium dihydrogen phosphate, CsH_2PO_4, is one of the members of potassium dihydrogen phosphate (KH_2PO_4-type) family. Under sufficient humidification, CsH_2PO_4 transforms from a monoclinic to a stable, cubic phase at 228 °C and 1 atm total pressure and exhibits high proton conductivity ($>10^{-2}$ Scm^{-1}) above this phase transition, known as the superprotonic phase transition [96, 97]. Due to its high conductivity in the superprotonic state and relatively high melting point (ca. 345 °C), CsH_2PO_4 has become an attractive candidate for fuel cells operating at low and intermediate temperatures.

However, conditions limit the range of CsH_2PO_4 superprotonic phase. Under dry conditions, it decomposes to form polymerization products (5.1) at temperatures above 200 ºC [97, 98] and conductivity decreases remarkably.

$$CsH_2PO_4 \rightarrow \tfrac{1}{2}\, Cs_2H_2P_2O_7 + \tfrac{1}{2}\, H_2O \rightarrow CsPO_3 + \tfrac{1}{2}\, H_2O \qquad (5.1)$$

Conductivity of CsH_2PO_4 in the superprotonic phase restrictedly depends on water vapor partial pressure. Although CsH_2PO_4 in superprotonic phase is stable at 30 mol% H_2O in argon, the mechanical properties of crystals at high humidity are not good appreciated for practical application [98]. The narrow temperature range and chemical instability of superprotonic phase limits CsH_2PO_4 to be used in fuel cell applications.

Stabilization of high conductive phase under no humidification is very important for practical uses of CsH_2PO_4. Heterogeneous dispersion of oxide particles provides robustness and enhanced ionic conductivity in low and intermediate temperature regions [97-99]. Heterogenous composites including proton conducting oxy-acid salts and mesoporous silica glass particles exhibit the enhanced conductivity due to high concentration of defects in the interface and disordered state of salt [98, 100-102]. Otomo et al. [97, 99] prepared CsH_2PO_4/SiO_2 composite by mechanical mixing and evaporation-to-dryness methods and observed the enhanced proton conductivity in CsH_2PO_4/SiO_2 composite prepared by the mechanical mixing method. Ponomareva and Shutova [98] showed CsH_2PO_4/SiO_2 composite exhibit conductivity values in the range of 10^{-3} to 10^{-2} S cm^{-1} at 130-250 ºC. CsH_2PO_4 composites can be used as electrolytes in SOFCs operating at intermediate temperatures between 100 and 300 ºC.

Among many oxide glasses, tellurium glasses possess interesting glass-forming ability, glass structure, non-hydroscopic properties with low glass transition temperature (Tg) and low melting point [103-106]. Furthermore, they are preferred over silicate and phosphate glasses due to their high dielectric constant, good corrosion resistance, and thermal and chemical stability etc. [107]. Due to these properties, TeO_2 containing glasses can be used in a wide range of applications, such as optical materials or fast-ions conducting solid electrolytes [108].

TeO_2-containing ternary systems have already been studied as glass materials, such as Eu_2O_3-TeO_2-P_2O_5 [107], ZnO-B_2O_3-P_2O_5-TeO_2 [108], Eu_2O_3-TeO_2-PbO_2 [109], Gd_2O_3-TeO_2-PbO [110], PbO-TeO_2-V_2O_5 [111, 112], Sm_2O_3-TeO_2-V_2O_5 [113], $TeO_2 \cdot B_2O_3$ [114], ZnO-P_2O_5-TeO_2 [115], V_2O_5-TeO_2-BaO [116], LiO-TeO_2-SiO_2 [117], NaO-TeO_2 [118], TeO_2-WO_3-PbO [119], Y_2O_3-TeO_3 [120], TeO_2-Bi_2O_3-GeO_2 [121].

Enhanced stability and conductivity properties of glassy materials and distinctive glass-forming ability of tellurium oxides lead us to investigate CsH_2PO_4/TeO_2 composite material. This part of the study presents the first result of synthesis, structural and electrical studies on CsH_2PO_4/TeO_2 glass.

5.2 Experimental

22 mmol telluric acid (H_6TeO_6) (99%, Sigma-Aldrich), 11 mmol cesium carbonate (Cs_2CO_3) (Alfa Aesar 99% metal basis) was dissolved in approximately 20 ml distilled water, separetly. 22 mmol phosphoric acid (H_3PO_4) (85 wt.% in H_2O, Sigma-Aldrich) was slowly added to the cesium carbonate solution. After three hours, the obtained solution was added to the first H_6TeO_6 one prepared separately and then evaporated slowly at approximately 50 ºC overnight. The expected reaction is (5.2):

$$\frac{1}{2}\, Cs_2CO_3 + H_3PO_4 + Te(OH)_6 \rightarrow CsH_2PO_4.\, Te(OH)_6 + \frac{1}{2}\, CO_2 + \frac{1}{2}\, H_2O \qquad (5.2)$$

Eventually this solution became gel like and it was kept in an oven, which was set to 205 ºC for 2 days. The resulting precipitates were ground in an agate mortar before measurements.

Scanning Electron Microscopy and Energy Dispersive X-ray Spectroscopy analysis was carried out by Zeiss Evo 60. EDS data were analyzed using the NSS 2.2 X-ray MicroAnalysis program.

X-ray diffraction data were recorded at room temperature using Stoe Theta-Theta Phase identification was carried out by X-ray powder diffraction analysis on a Bruker D8 diffractometer with Cu Kα radiation. Experiments were performed both at ambient and elevated temperatures (by 50°C intervals up to T=450°C) in dry air. Collected data were analyzed using the STOE Win XPOW 2.20 program.

Termogravimetry and differential thermal analysis were carried out in air using TG-DTA system (Netzsch STA 409 CD) at a scan rate of 5 °C min^{-1}. Differential scanning calorimetry experiments were performed by Netzsch DSC 200 F3, heating the powder from room temperature to 500 °C at a scan rate of 5 °C min^{-1}.

Conductivity measurements were carried out using electrochemical impedance spectroscopy. The pellet was produced by pressing the powder into discs of 1 mm thickness and 8 mm diameter at 200 MPa pressure. The pellet was tested with gold electrodes between 100 to 457 °C. Gold electrodes were sputtered on both sides of the pellet.

The measurements were done under dry air, humidified (pH_2O=0.1 bar) air and humidified (pH_2O=0.1 bar) gas mixture of 9% H_2 in N_2. The gases were humidified by bubbling through water at 46 °C. In the measurement series, impedance spectra were recorded using a Solartron 1260 frequency analyzer under flowing gases (50 ml/min). An excitation voltage with amplitude 20 mV was used. No bias voltage was applied. The temperature of measurement was increased stepwise with heating rates of 5 °C min^{-1}. Measurements were performed over the frequency range 1 MHz to 1 Hz. Data analysis was carried out using the ZSimpWin 3.21 program.

5.3 Results and Discussions

5.4.1 Structral and Thermal Analysis

A cross section SEM image of the CsH_2PO_4/TeO_2 pellet is illustrated in Figure 5.1. As seen in Figure 5.1, no variation is seen in the image contrast, which can be attributed to that the single phase is obtained.

Figure 5.2 gives a typical EDS spectrum, which shows that the powder consist of the expected elements. Hydrogen is not detectable by EDS analysis. Figure 5.3 shows the results of 5 EDS point analysis on the surface of the compound, which shows distribution of elements for different points. Referring to Figure 5.3, the small difference in composition (atomic %) of the synthesized compound may be attributed to topographical effect rather than variation of the chemical composition across the sample, which is in an agreement with the SEM results. The composition of the compound obtained by EDS analysis supports the expected compound of CsH_2PO_4/TeO_2.

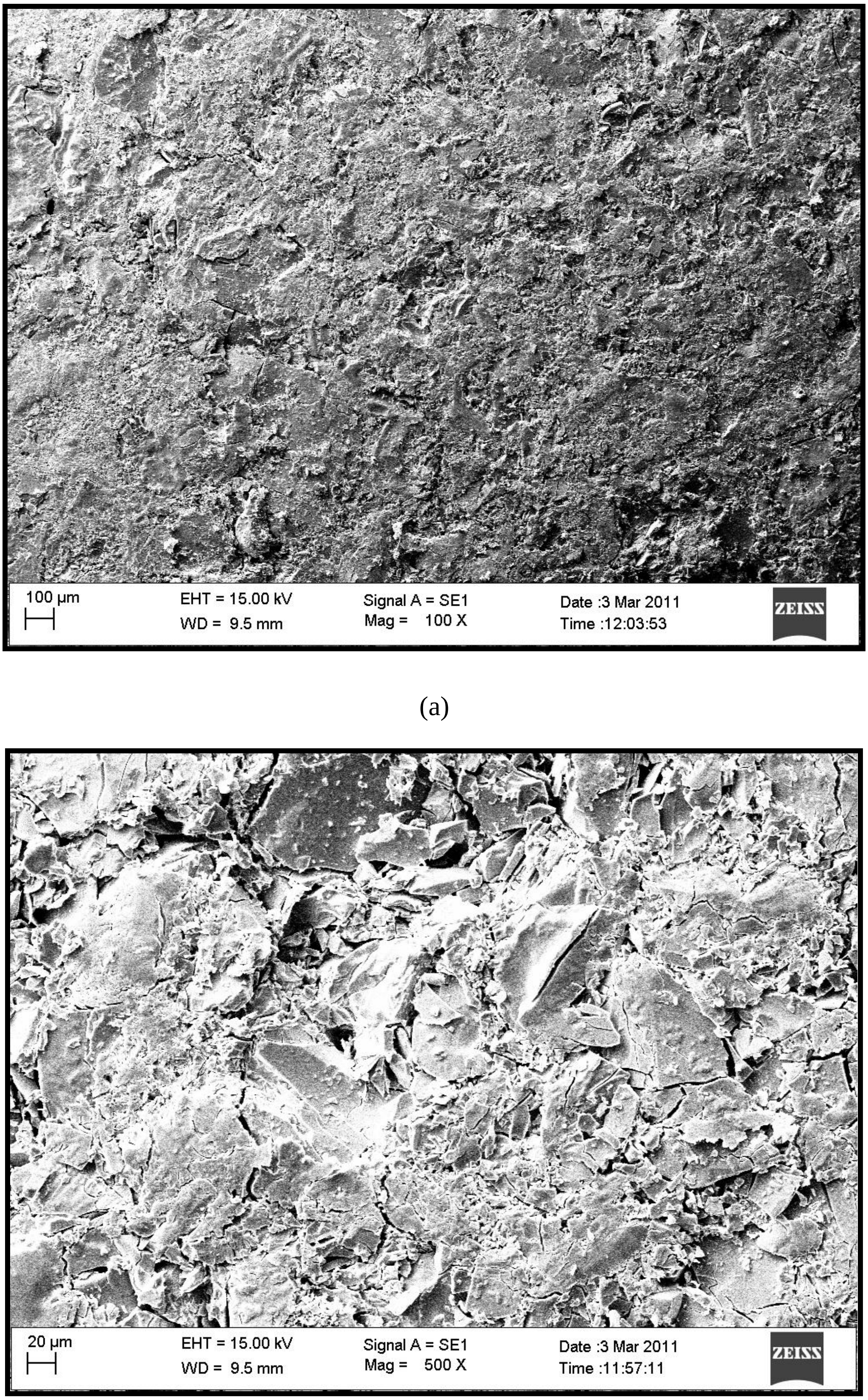

(a)

(b)

Figure 5.1 A cross section SEM image of the CsH_2PO_4/TeO_2 pellet; (a) X100, (b) X500

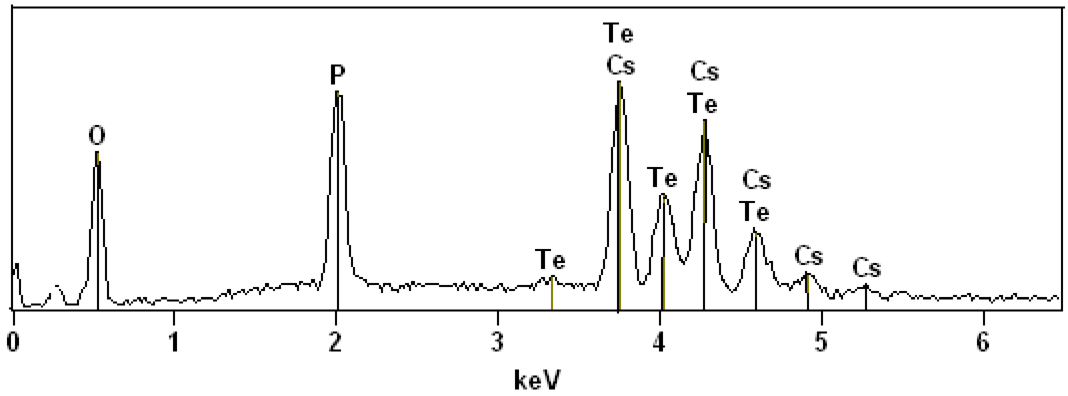

Figure 5.2 EDS spectrum showing typical composition of the synthesized compound (Hydrogen is not detectable by EDS analysis, carbon was detected due to carbon coating of the pellet prior to EDS measurement)

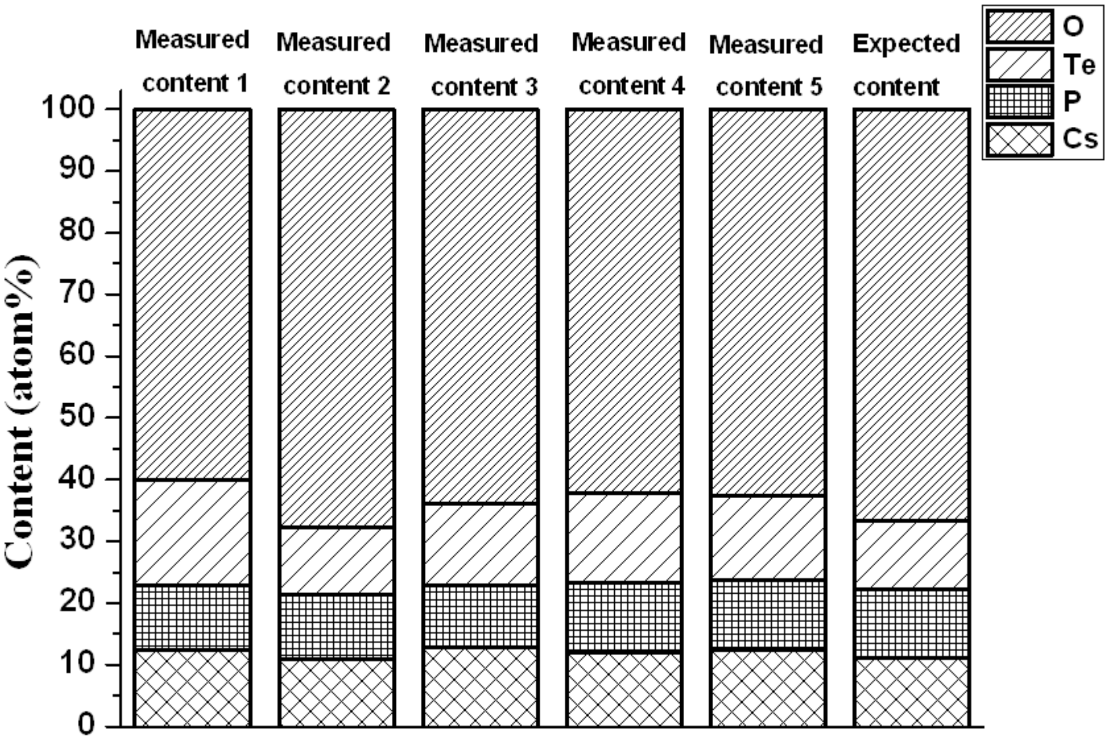

Figure 5.3 Point analysis showing distribution of detectable elements at five different points on the surface of the synthesized CsH_2PO_4/TeO_2

Figure 5.4 shows thermal analysis of the compound under air. An endothermic effect is seen up to 50 °C and above this temperature; an exothermic effect is occurred upon heating. These endothermic and exothermic effects can be attributed to the glass transition and crystallization, respectively. Tadagana et al. [122] reported that a solid acid glass of $70CsHSO_4 \cdot 30NaHSO_4$ shows a glass transition at 17 ºC and crystallization at 58 ºC. On the other hand, no exothermic effect on first and second heating cycles is seen in DSC analysis given in Figure 5.5. In Figure 5.5(a), a broad endothermic effect at 30 ºC and an exothermic effect around 75 °C on the first heating/cooling cycles are slightly observed, which become significant on the second heating/cooling cycyles (Figure 5.5(b)). The endothermic peak is shifted to a higher temperature (50 ºC) on the second heating cycle. Furthermore, Figure 5.4 and Figure 5.5(a) indicate another endothermic peak seen around 345 °C attributed to melting of CsH_2PO_4 reported as 345 ºC in the literature [123]. This observation is in an agreement with the literature. Park [124] and Ponomareva and Shutova [98] reported the expected weight loss of 7.8wt.% for complete dehydration of CsH_2PO_4 is observed during heating up to 400 ºC. The weight loss for CsH_2PO_4/TeO_2 glass is lower (5.2wt.% at 400 ºC) comparing with the pure salt. The observed weight loss of 6.77wt.% up to 500 ºC indicates that dehydration of the CsH_2PO_4/TeO_2 glass is not completed up to that relatively high temperature.

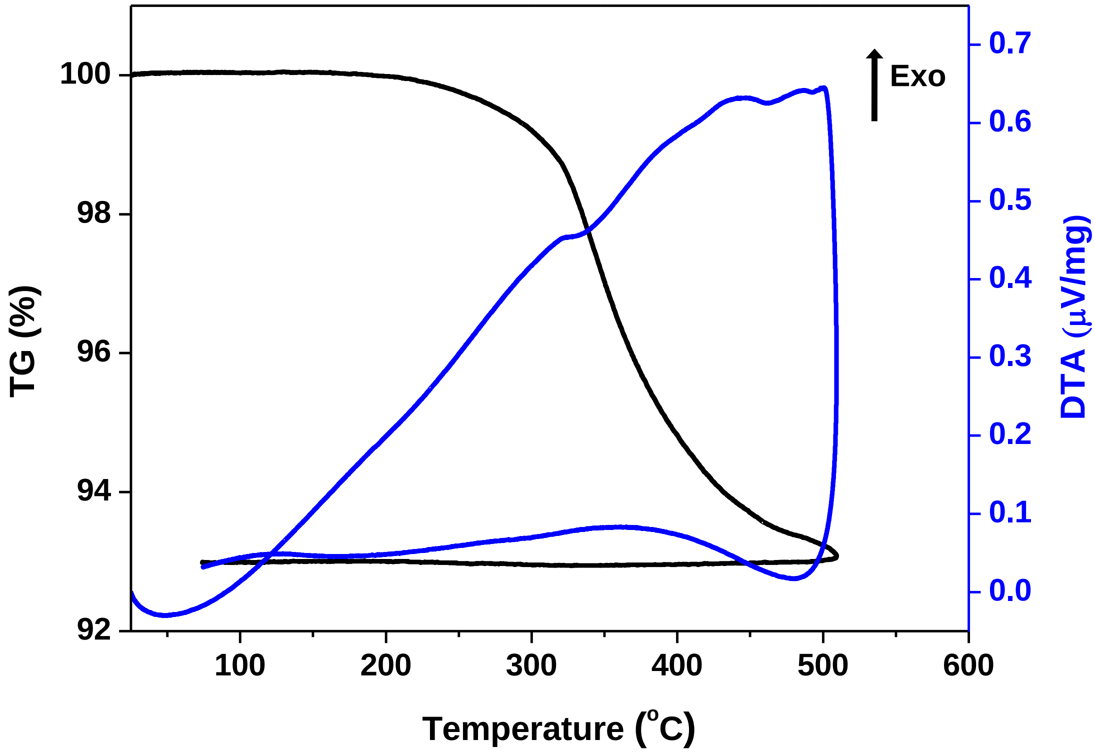

Figure 5.4 TG/DTA analysis of the synthesized compound under air at a scan rate of 5 °C min^{-1}

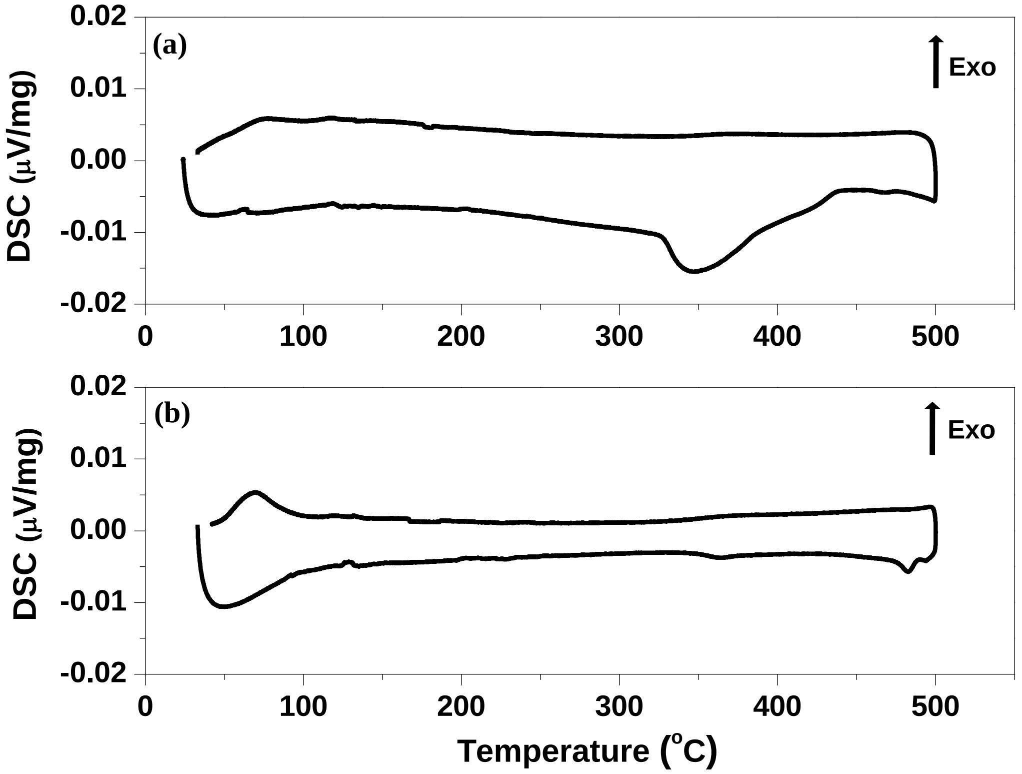

Figure 5.5 DSC analysis of the synthesized powder under air at a scan rate of 5 ˚C min^{-1}; (a) first and (b) second heating/cooling cycles

Figure 5.6 gives HT-XRD diagrams of the synthesized powder. In the room temperature (RT) XRD, a halo pattern is observed, indicating that glass is obtained in this compound. In the XRD pattern at 100 °C, a small peak become visible around 2θ=28 can be attributed to crystallization, which is agreed with the exothermic effect observed above 50 ˚C on the DTA curve although a clear exothermic change due to glass transition is not observed in the DSC curve. In the XRD pattern at 400 ˚C, two other peak (2θ=28.5 and 2θ=30) becomes slightly visible, which are clear at 450 ºC. Therefore, it can be claimed that an onset temperature for changes in the sample is at ca. 400 ˚C. Figure 5.7 shows the RT-XRD of the synthesized powder, the XRD pattern at 450 ˚C and that at 30 ˚C after cooling. The scan at 450 ˚C and that at 30 ˚C after cooling are the same except for a small down shift of the high temperature data due to the thermal expansion. It can be concluded whatever has formed during heating is not undergoing a structural phase transition during cooling. The sample was inspected at room temperature and it had blackened significantly during the heating in air.

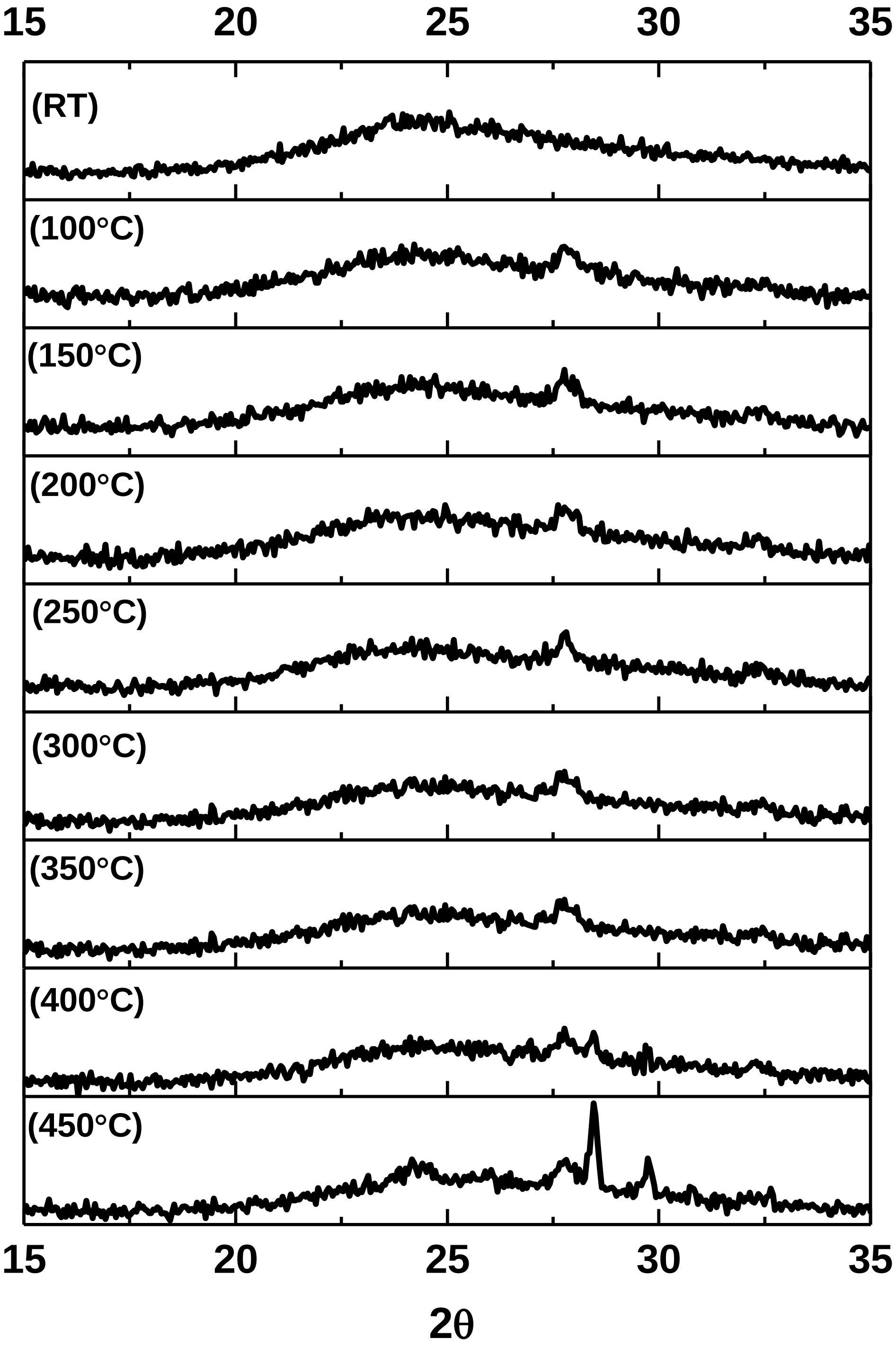

Figure 5.6 HT-XRD diagrams of the synthesized powder

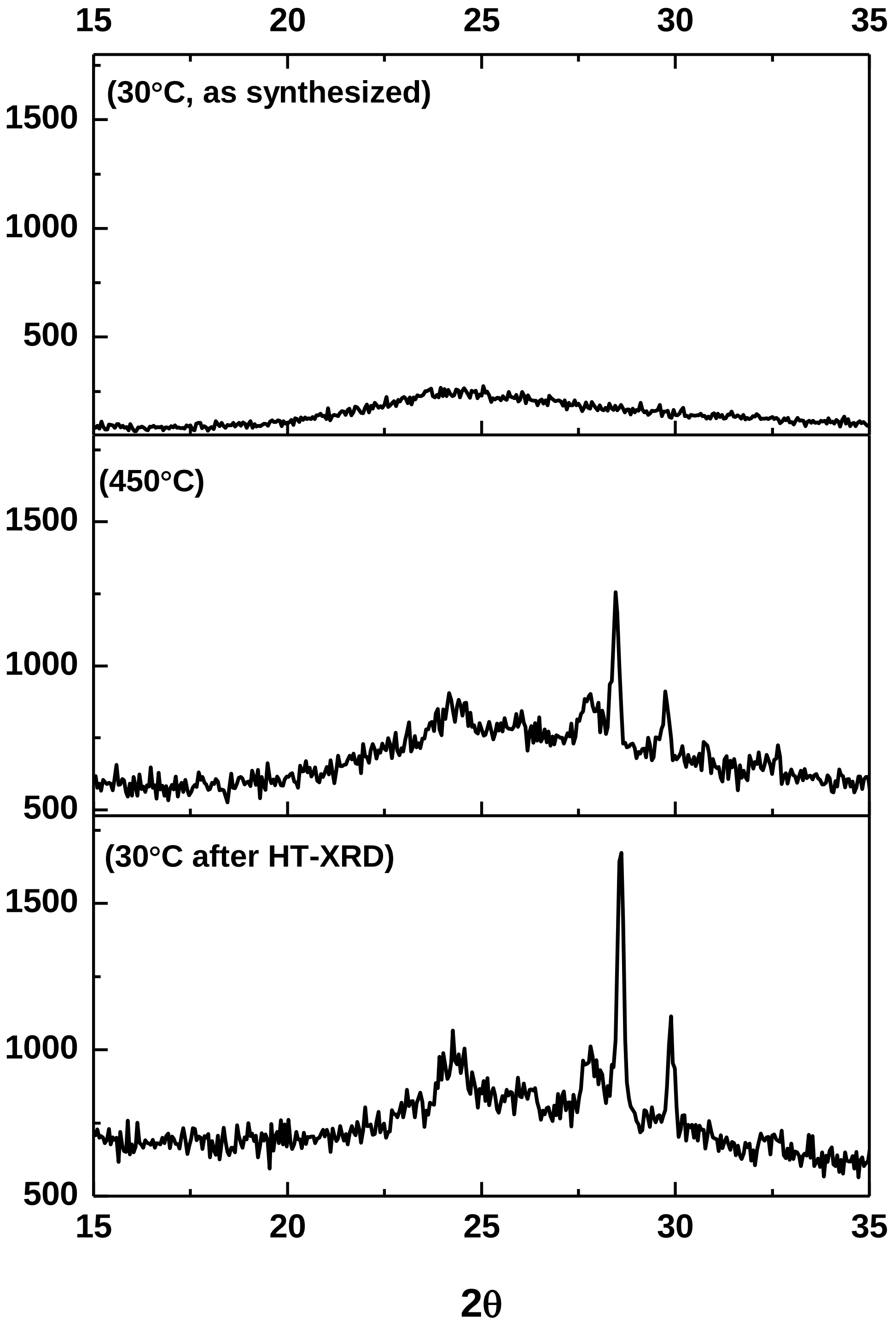

Figure 5.7 The room temperature XRD of the synthesized powder, the last scan at 450 ˚C and that at 30 ˚C after cooling

Figure 5.8 gives a comparison of the XRD patterns of the synthesized compound and tested pellet under humidified reducing atmosphere up to 457 ˚C. It is clear that the obtained compound after conductivity measurement is different from the synthesized compound and the formed compound upon heating up to 450 ˚C under air.

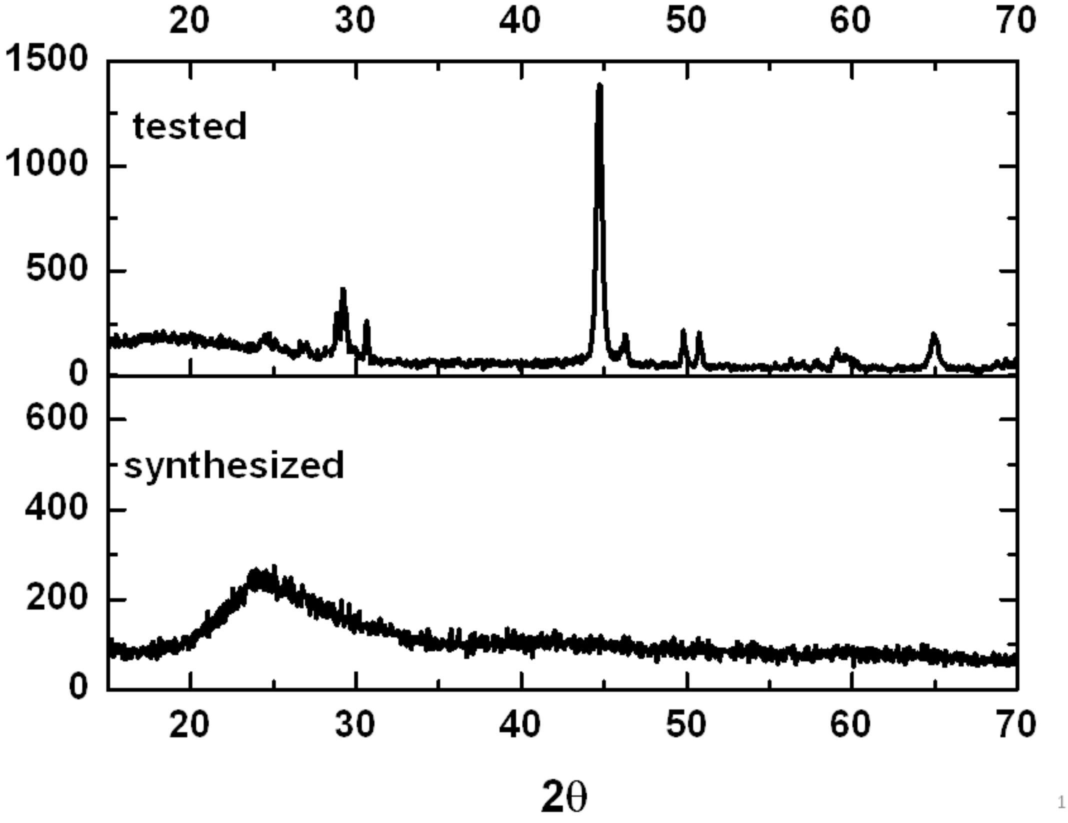

Figure 5.8 The XRD of the synthesized compound and the tested pellet under humidified reducing atmosphere up to 457 ˚C

5.3.2 Electrochemical Impedance Spectroscopy

Figure 5.9 shows plot of conductivity log(σ) versus temperature. In dry air, the conductivity shows an increase upon heating up to 136 ˚C and then starts to decrease up to 166 ˚C. By changing to the humidified air (pH_2O=0.1 bar) at that temperature, the conductivity shows a rise from $2.95 \cdot 10^{-6}$ S cm^{-1} to $9.85 \cdot 10^{-4}$ S cm^{-1}. At same temperature, the atmosphere changed from humidified air to humidified gas mixture of 9% H_2 in N_2 and just a small increase is seen in the conductivity ($2.37 \cdot 10^{-3}$ S cm^{-1}). no significant change in the conductivity is seen.Upon heating under same atmosphere, conductivity shows an almost linear increase up to 240 ºC and reaches a value of

$1.73 \cdot 10^{-2}$ S cm^{-1} at that temperature. Between 240-348 ºC, no change is seen in the conductivity. Above 348 ºC, the conductivity starts to decrease and become a value of $1.5 \cdot 10^{-3}$ S cm^{-1} at 457 ˚C.

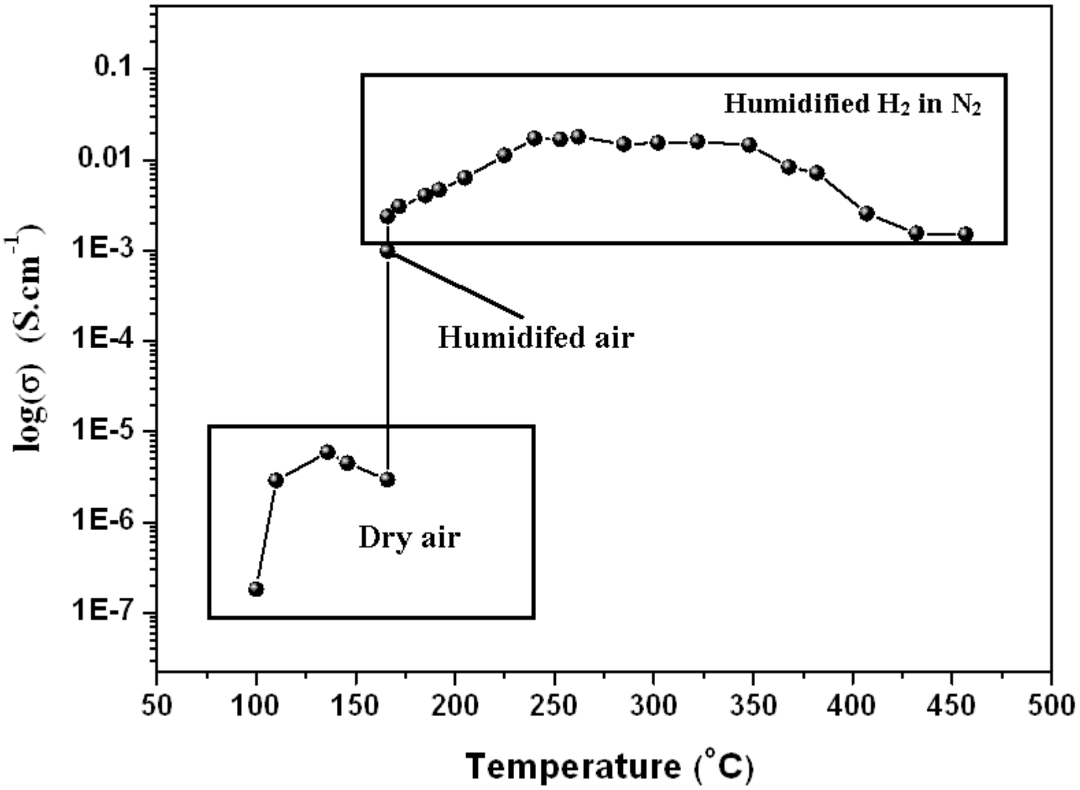

Figure 5.9 Plot of conductivity log(σ) versus temperatures. The pellet was tested with gold electrodes.

All EIS data (except the data at 225 and 262 ºC) were fitted to an equivalent circuit model given in Figure 5.10. A similar model was used in the literature for a comparable system [125].

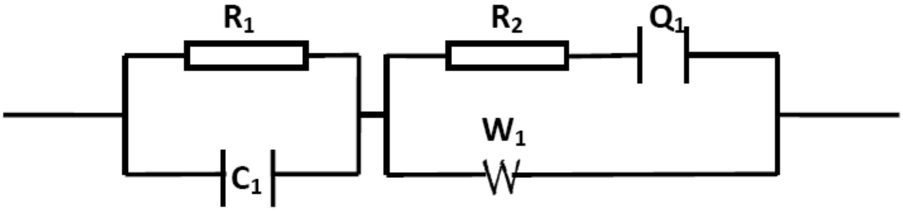

Figure 5.10 Equivalent circuit model used fit the impedance spectra

Figure 5.11 illustrates typical impedance spectra obtained in the temperature range of 100 ºC to 166 ºC in dry air. The resistance of the electrolyte decreases by increasing temperature up to 136 ºC and then starts to increase due to dehydration of the compound.

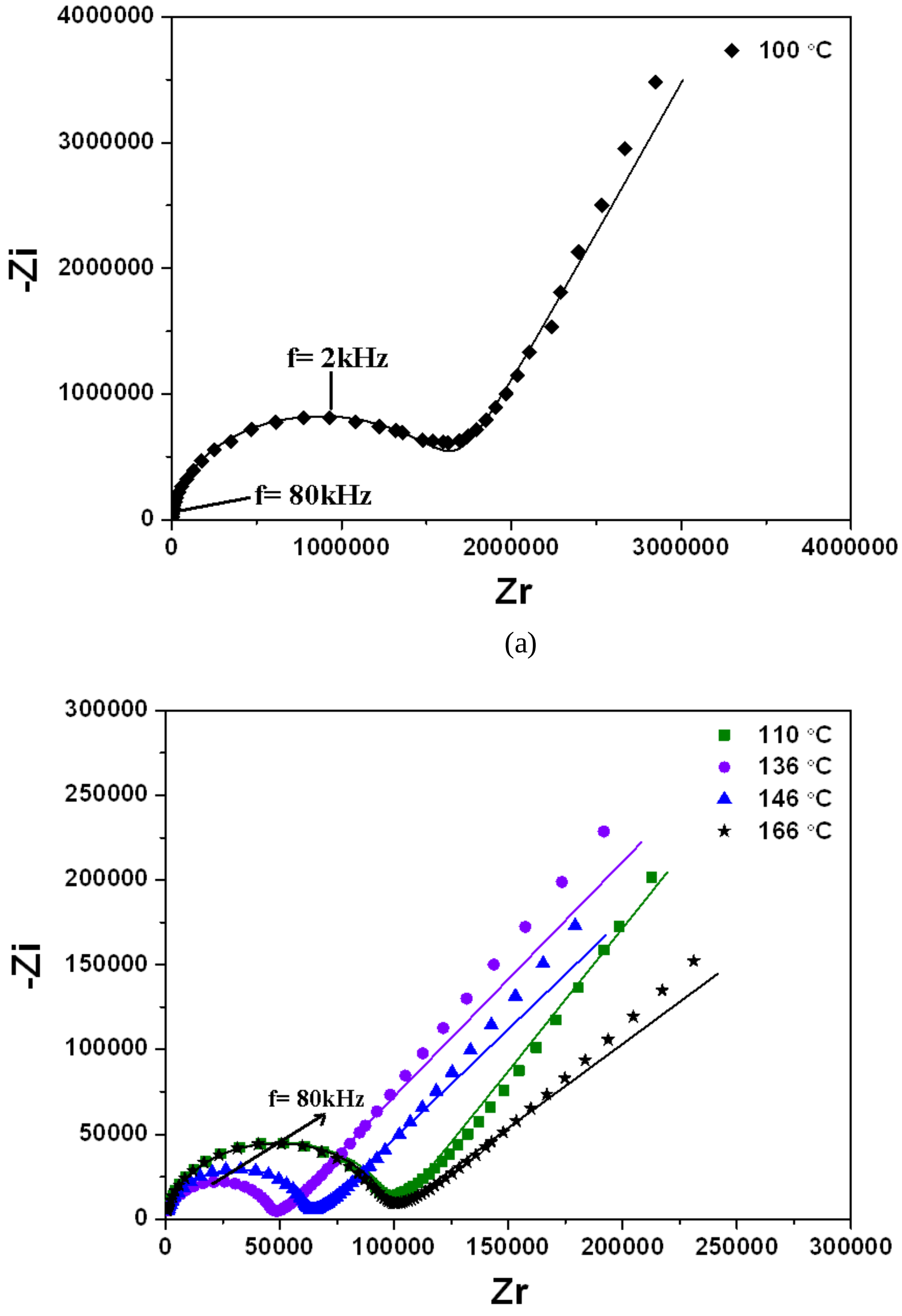

(a)

(b)

Figure 5.11 Impedance spectrum of CsH_2PO_4/TeO_2 pellet at (a) 100 ºC, (b) 110, 136, 146 and 166 ºC in dry air.

Figure 5.12 gives typical impedance spectra obtained at 166 ºC in various atmospheres. While Figure 5.12(a) shows the impedance spectra at 166 ºC in dry air, Figure 5.12 (b and c) gives that in humidified air and humidified gas mixture of 9% H_2 in N_2, respectively. The resistance of the electrolyte remarkably decreases by changing the atmosphere from dry air to humidified air. In the humidified gas mixture of 9% H_2 in N_2, the resistance of the electrolyte keeps decreasing and the intermediate frequency arc becomes visible.

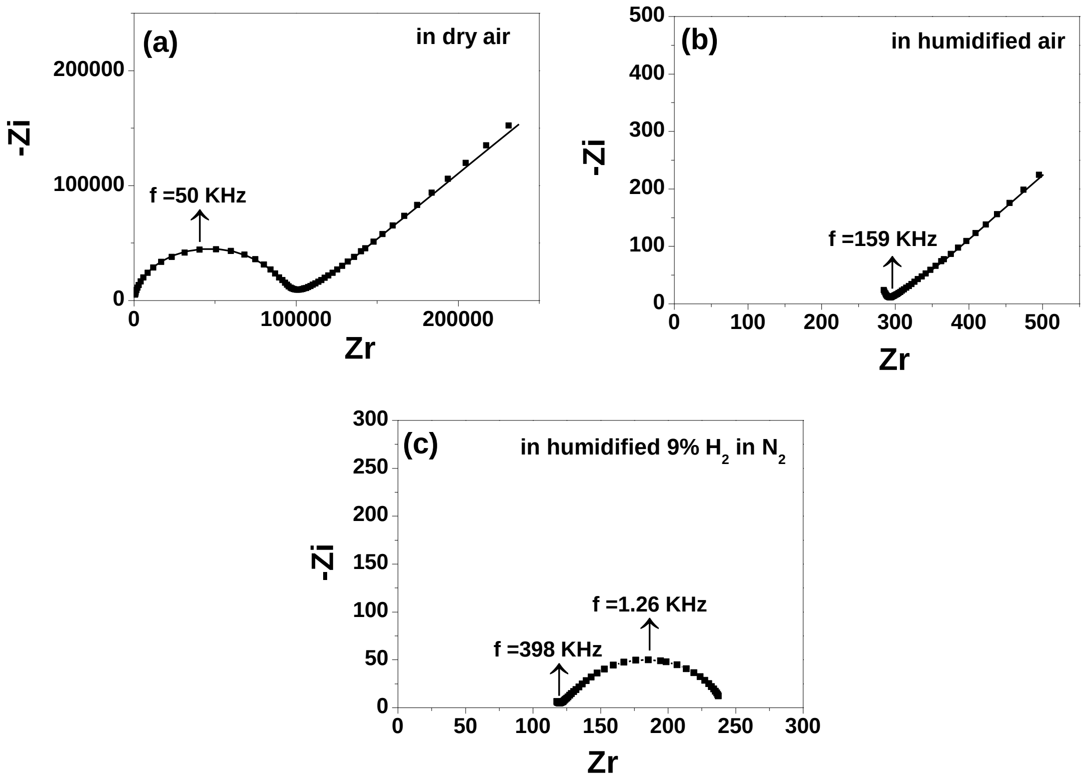

Figure 5.12 Impedance spectrum of CsH_2PO_4/TeO_2 pellet at 166 ºC in (a) dry air, (b) humidified air and (c) humidified gas mixture of 9% H_2 in N_2

In order to investigate the thermal behaviour of the compound, the impedance spectra were measured around the phase transition temperature (230 ºC) of CsH_2PO_4. Figure 5.13 denotes impedance spectra below phase transition 205 ºC, around phase transition 225 ºC and above phase transition 262 ºC. The impedance spectrum was formed at two parts at 205 ºC, which can be considered at medium and high frequencies. The medium frequency arc is attributed to effect of double layer; the high frequency response represents to bulk and grain boundaries. The value n= 0.65 showes a relatively high capacitance and low diffusion of hydrogen ion (H^+) below phase transition 205 ºC, while the value n= 0.14 indicates low capacitance and high diffusion of hydrogen due to superprotonic phase transition around 230 ºC. At the temperatures of 225 and 262 ºC, the arc is distorted into a straight line. The straight line resulted from diffusion impedance indicates the Warburg impedance law for semi-infinite diffusion. The diffusion region is not limited due to high conductivity around and above the phase transition temperature.

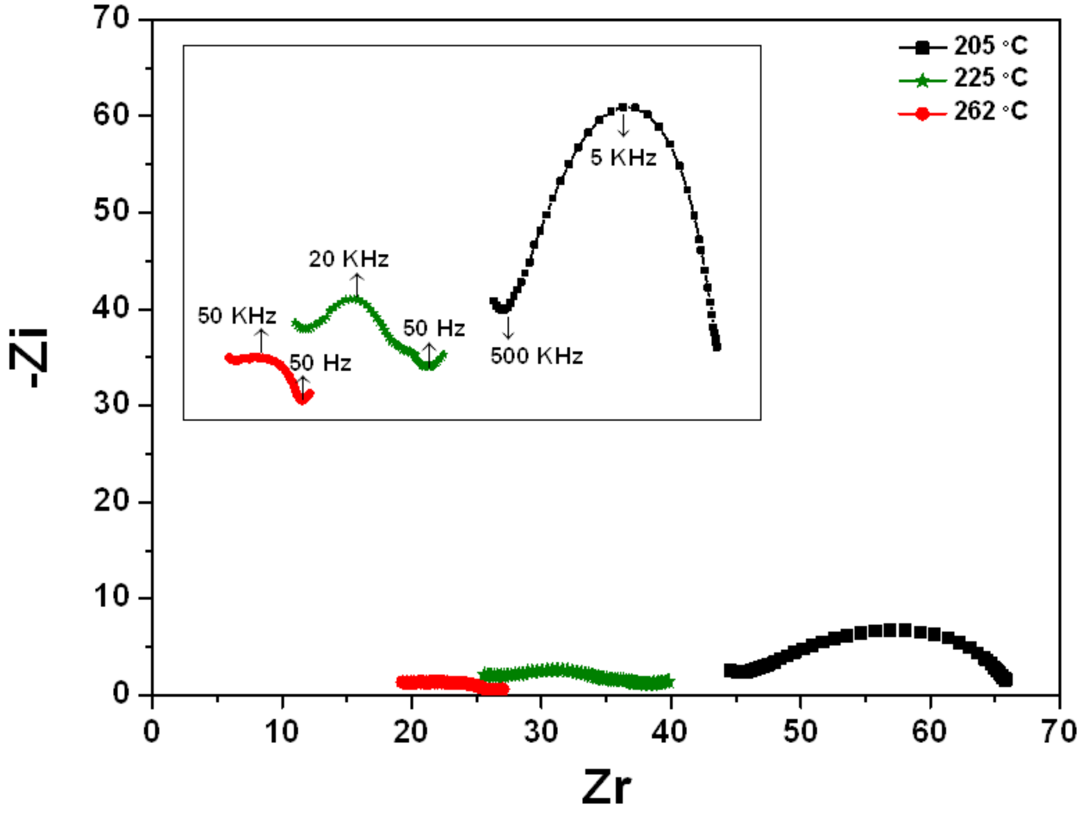

Figure 5.13 Impedance spectrum of CsH_2PO_4/TeO_2 pellet at 205 ºC, 225 ºC and 205 ºC 262 ºC in humidified gas mixture of 9% H_2 in N_2.

5.4 Conclusions

Ionic glass of CsH_2PO_4/TeO_2 was obtained by heat treatment at 205 ºC following a slow evaporation. The CsH_2PO_4/TeO_2 glass exhibited conductivity as high as CsH_2PO_4. The high conductivity value of $2 \cdot 10^{-2}$ S cm^{-1} was observed at 240 ºC and was kept in the wide temperature range of 240 ºC to 348 ºC, which is the melting point (345 ºC) of the CsH_2PO_4. It is revealed that TeO_2 addition into CsH_2PO_4 is significantly effective in enhancing the thermal stability of the CsH_2PO_4. These results suggest that vitrified solid acids have advantages in proton conduction and thermal stability compared with the solid acid.

CHAPTER 6

CONCLUSIONS and RECOMMENDATIONS

The research decribed in this thesis has been focused on developing advanced electrode and electrolyte materials for low and intermediate temperature solid oxide fuel cells. The following conclusions and recommendations are drawn from the findings of this work:

(1) $V_{0.13}Mo_{0.87}O_{2.935}$ powder synthesized by reducing acidified vanadate and molybdate solution at 60 ºC by passing hydrogen sulfide gas through the solution showed a phase transition between hexagonal to orthorhombic structures at 430 ºC. The highest cell performance with a peak power of 2.88 W was observed at 750 ºC in dry H_2. 50 ppm H_2S contamination in dry H_2 caused a 22% decrease in the peak power. The deactivation process was irreversible for a short-term exposure to sulfur free gas. Electrochemical impedance measurements resulted in two responses at high and low frequencies. The thermally activated high frequency response was assigned to diffusion, while the low frequency response, which was relatively independent on temperature, was attributed to the gas conversion on the anode surface. Furthermore, 50 ppm-H_2S contamination in dry H_2 caused an increase in the electrode polarization resistance due to the chemical adsorption of the anode active sites. OCV value of the cell decreased linearly as expected for a typical short-term sulfur poisoning process.

The short-term sulfur poisoning and reactivation process were studied in this study, but the long-term sulfur poisoning and reactivation process are still unknown. Further detailed studies should be done to explore these.

(2) The $RbH(PO_3H)\cdot Te(OH)_6$ compound formed in an amorphous and crystalline structure. The conductivity of the compound decreased during dehydration, as

expected. The electrode contribution, as the ohmic resistance associated with the pellet tested with platinium carbon electrodes was not subtracted. Therefore, higher conductivity values were achieved with the pellets tested with gold electrodes and the highest conductivity value of 5.41 10^{-5} S cm^{-1} was obtained at 317 °C by dehydration of the compound. Dehydration is not usually responsible for increasing conductivity. This increase in the conductivity was due to the fact that the monoprotic $RbH(PO_3H)$ part of $RbH(PO_3H)\cdot Te(OH)_6$ became a diprotic $Rb_2H_2P_2O_5$ part of the formed $Rb_2H_2P_2O_5\cdot[Te(OH)_6]_2$ compound by dehydration. The dehydrated compound has also a higher hydrogen density relative to the starting compound. For that reason, it can be assumed that the dehydration of the $RbH(PO_3H)\cdot Te(OH)_6$ enhances the conductivity. Moreover, it was seen that a dehydrated compound shows stability against operating time and temperature changes up to 317 °C.

The conductivity of the compound was investigated up to 317 °C in this study. Further investigation above that temperature is recommended.

(3) Synthezied Rb_2SeO_4 contained a second phase of Rb_2SeO_3, which can be eliminated by heating the compound above the phase transition temperature (549 °C). The formation of RbOH by decompositions of Rb_2SeO_4 was responsible for the obtained protonic conductivity in humidified atmospheres and this conductivity increases by increasing temperature. The highest conductivity value of $2.01\cdot 10^{-4}$ S cm^{-1} was observed at 317 °C. This conductivity value may further increase upon heating, as reported that the conductivity of RbOH reaches to very high levels as about 10^{-1} S cm^{-1} up to melting point of RbOH (382 °C). Therefore, the conductivity can also be checked for the temperatures above 317 °C.

(4) CsH_2PO_4/TeO_2 glass was obtained by heat treatment at 205 ºC following a slow evaporation. The CsH_2PO_4/TeO_2 glass exhibited conductivity as high as CsH_2PO_4. The highest conductivity value of $2\cdot 10^{-2}$ S cm^{-1} was observed at 240 ºC and was kept in the wide temperature range of 240 ºC to 348 ºC. TeO_2 addition into CsH_2PO_4 positively affected the thermal stability of the CsH_2PO_4. In this study, CsH_2PO_4/TeO_2 glass with a molar ratio 1:1 was investigated. Further studies on this glass should be done for various molar ratios.

REFERENCES

[1]. EG&G Services, Parsons, Inc. and Science Applications International Corporation, (2000). Fuel Cell Handbook, 5th Edition, Business/Technology Books, West Virginia, US.

[2]. EG&G Technical Services, Inc. and Science Applications International Corporation, (2002). Fuel Cell Handbook, 8th Edition, Business/Technology Books, West Virginia, US.

[3]. Gong, M., Liu, X., Trembly, J. and Johnson, C., (2007). "Sulfur-Tolerant Anode Materials for Solid Oxide Fuel Cell Application", Journal of Power Sources, 168(2):289-298.

[4]. Xia, C., Rauch, W., Chen, F. and Liu, M., (2002). "$Sm_{0.5}Sr_{0.5}CoO_3$ Cathodes for Low-Temperature SOFCs", Solid State Ionics, 149(1-2):11-19.

[5]. Zheng, L.L., Wang, X., Zhang, L., Wang, Y.J. and Jiang, P.J., (2012). "Effect of Pd-impregnation on Performance, Sulfur Poisoning and Tolerance of Ni/GDC Anode of Solid Oxide Fuel Cells", International Journal of Hydrogen Energy, 37(13):10299-10310.

[6]. Li, J.H., Fu, X.Z., Luo, J.L., Chuang, K.T. and Sanger, A.R., (2012). "Application of $BaTiO_3$ as Anode Materials for H_2S Containing CH_4 Fueled Solid Oxide Fuel Cells", Journal of Power Sources, 213:69-77.

[7]. Vorontsov, V., An, W., Luo, J.L., Sanger, A.R. and Chuang, K.T., (2008). "Performance and Stability of Composite Nickel and Molybdenum Sulfide Based Anodes for SOFC Utilizing H_2S", Journal of Power Sources, 179:9-16.

[8]. Roushanafshar, M., Luo, J.L., Vincent, A.L., Chuang, K.T. and Sanger, A.R., (2012). "Effect of Hydrogen sulfide Inclusion in Syngas Feed on the Electrocatalytic Activity of LST-YDC Composite Anodes for High Temperature SOFC Applications", International Journal of Hydrogen Energy, 37(9):7762-7770.

[9]. Wenyi, T., Qin, Z., Han, Y., Xiufang, Z. and Hongyi, L., (2012). "Deactivation of Anode Catalyst $La_{0.75}Sr_{0.25}Cr_{0.5}Mn_{0.5}O_{3\pm\delta}$ in SOFC with Fuel Containing Hydrogen Sulfur: The Role of Lattice Oxygen", International Journal of Hydrogen Energy, 37(9):7398-7404.

[10]. Zhu, X., Yan, H., Zhong, Q., Zhao, X. and Tan, W., (2011). "$Ce_{0.9}Sr_{0.1}Cr_{0.5}Fe_{0.5}O_{3\pm\delta}$ as the Anode Materials for Solid Oxide Fuel Cells Running on H_2 and H_2S", Journal of Alloys and Compounds, 509(33):8360-8364.

[11]. Danilovic, N., Luo, J.L., Chuang, K.T. and Sanger, A.R., (2009). "$Ce_{0.9}Sr_{0.1}VO_x$ (x=3,4) as Anode Materials for H_2S Containing CH_4 Fueled Solid Oxide Fuel Cells", Journal of Power Sources, 192(2):247-257.

[12]. Lu, Z.G., Zhu, J.H., Bi, Z.H. and Lu, X.C., (2008). "A Co-Fe Alloy as Alternative Anode for Solid Oxide Fuel Cell", Journal of Power Sources, 180:172-175.

[13]. Kurokawa, H., Yang, L.Y., Jacobson, C.P., De Jonghe, L.C. and Visco, S.J., (2007). "Y-doped $SrTiO_3$ Based Sulfur Tolerant Anode for Solid Oxide Fuel Cells", Journal of Power Sources, 164:510-518.

[14]. Li, J.H., Fu, X.Z., Luo, J.L., Chuang, K.T. and Sanger, A.R., (2012). "Application of $BaTiO_3$ as Anode Materials for H_2S-containing CH_4 Fueled Solid Oxide Fuel Cells", Journal of Power Sources, 213:69-77.

[15] Lu, X.C., Zhu, J.H., Yang, Z., Xia, G. and Stevenson, J.W., (2009). "Pd-impregnated SYT/LDC Composite as Sulfur-Tolerant Anode for Solid Oxide Fuel Cells", Journal of Power Sources, 192:381-384.

[16] Zhu, X., Zhong, Q., Zhao, X. and Yan, H., (2011). "Synthesis and Performance of Y-doped $La_{0.7}Sr_{0.3}CrO_{3-\delta}$ as a Potential Anode Material for Solid Oxygen Fuel Cells", Applied Surface Sources, 257:1967-1971.

[17] Lohsoontorn, P., Brett, D.J.L. and Brandon, N.P., (2008). "The Effect of Fuel Composition and Temperature on the Interaction on H_2S with Nickel-Ceria Anodes for Solid Oxide Fuel Cells", Journal of Power Sources, 183:232-239.

[18] Haile, S.M., Boysen, D.A., Chisholm, C.R.I. and Merle, R.B., (2001). "Solid Acids as Fuel Cell Electrolytes", Nature, 410:910-913.

[19] Boysen, D.A., Uda, T., Chisholm, C.R.I. and Haile, S.M., (2004). "High-Performance Solid Acid Fuel Cells Through Humidity Stabilization", Science, 303:68-70.

[20] Uda, T. and Haile, S.M., (2005). "Thin-Membrane Solid-Acid Fuel Cell", Electrochemical Solid-State Letters, 8(5):A245-A246.

[21] Haile, S.M., Chisholm, C.R.I., Sasaki, K., Boysen, D.A. and Uda, T., (2007). "Solid Acid Proton Conductors: from Laboratory Curiosities to Fuel Cell Electrolytes", Faraday Discussions, 134:17-39.

[22] Li, Z. and Tang, T., (2010). "High-Temperature Thermal Behaviors of XH_2PO_4 (X=Cs, Rb, K, Na) and LiH_2PO_3", Thermochimica Acta, 501:59-64.

[23] Bondarenko, A.S., Zhou, W. and Bouwmeester, H.J.M., (2009). "Superprotonic $KH(PO_3H)$-SiO_2 Composite Electrolyte for Intermediate Temperature Fuel Cells", Journal of Power Sources, 194:843-846.

[24] Zhou, W., Bondarenko, A.S., Boukamp, B.A. and Bouwmeester, H.J.M., (2008). "Superprotonic Conductivity in $MH(PO_3H)$ ($M=Li^+$, Na^+, K^+, Rb^+, Cs^+, NH_4^+)", Solid State Ionics, 179:380-384.

[25] Chisholm, C.R.I., Merle, R.B., Boysen D.A. and Haile, S.M., (2002). “Superprotonic Phase Transition in $CsH(PO_3H)$”, Chemistry of Materials, 14(9):3889-3893.

[26] Matsuo, T., Tanaka, Y., Hatori, J. and Ikehata, S., (2008). “Effect of Uniaxial Stress in Superprotonic Phase Transition in $Cs_3H(SeO_4)_2$”, Solid State Ionics, 179:1125-1127.

[27] Haile, S.M., Calkins, P.M. and Boysen, D., (1997). “Superprotonic Conductivity in β-$Cs_3(HSO_4)_2(H_x(P,S)O_4)$”, Solid State Ionics, 97:145-151.

[28] Ponomareva, V.G. and Lavrova, G.V., (2001). “The Investigation of Disordered Phases in Nanocomposite Proton Electrolytes Based on $MeHSO_4$ (Me= Rb, Cs, K)”, Solid State Ionics, 145:197-204.

[29] Ktari, L., Dammak, M., Madani, A., Mhiri, T. and Kolsi, A.W., (2001). “Conductivity Study of a New Protonic Conductor $Rb_{1.12}(NH_4)_{0.88}SO_4 \cdot Te(OH)_6$”, Solid State Ionics, 145(1-4):225-231.

[30] Litaiem, H., Dammak, M., Mhiri, T. and Cousson, A., (2005). “Structural, Conductivity and Dielectric Studies in $(NH_4)_2SeO_4 \cdot Te(OH)_6$”, Journal of Alloys and Compounds, 396(1-2):34-39.

[31] Abdelhedi, M., Dammak, M., Cousson, A. and Kolsi, A.W., (2005). “Structural, Calorimetric and Conductivity Study of the New Mixed Solution $Rb_2(SO_4)_{0.5}(SeO_4)_{0.5}Te(OH)_6$”, Journal of Alloys and Compounds, 398(1-2):55-61.

[32] Dammak, M., Litaiem, H., Gravereau, P., Mhiri, T. and Kolsi, A.W., (2007). “X-Ray and Electrical Conductivity Studies in the Rubidium Selenate Tellurate”, Journal of Alloys and Compounds, 442:316-319.

[33] Dammak, M., Hadrich, A. and Mhiri, T., (2007). “Structural, Dielectric and Vibrational Studies in the Dipotassium Sulfate Selenate Tellurate Mixed Solid Solution”, Journal of Alloys and Compounds, 428:8-16.

[34] Taninouchi, Y.K., Uda, T., Awakura, Y., Ikeda, A. and Haile, S.M., (2007). “Dehydration Behavior of the Superprotonic Conductor CsH_2PO_4 at Moderate Temperatures: 230 to 260 Degrees C”, Journal of Materials Chemistry, 17(30):3182-3189.

[35] Goñi-Urtiaga, A., Presvytes, D. and Scott, K., (2012). “Solid Acids as Electrolyte Materials for Proton Exchange Membrane (PEM) Electrolysis: Review”, International Journal of Hydrogen Energy, 37:3358-3372.

[36] Adams, A.H., Haaß, F., Buhrmester, T., Kunert, J., Ott, J., Vogel, H. and Fuess, H., (2004). “Structure and Reaction Studies on Vanadium Molybdenum Mixed Oxides”, Journal of Molecular Catalysis A: Chemical, 216:67-74.

[37] Mougin, O., Dubois, J.L., Mathieu, F. and Rousset, A., (2000). “Metastable Hexagonal Vanadium Molybdate Study”, Journal of Solid State Chemistry, 152(2):353-360.

[38] Chandra, A., Roberts, A.J. and Slade, R.C.T., (2008). “Studies of Nanostructures and Conductivity in the System $V_xMo_{1-x}O_y$”, Solid State Communications, 147(3-4):83-87.

[39] Lin, M.M., (2003). “Complex Metal Oxide Catalysts for Selective Oxidation of Propane and Derivatives: II. The Relationship among Catalyst Preparation, Structure and Catalytic Properties”, Applied Catalysis A: General 250(2):287-303.

[40] Feist, T.P. and Davies, P.K., (1991). “Soft Chemical Synthesis of New Compounds with the Hexagonal Molybdenum Oxide Structure”, Chemistry of Materials, 3(6):1011-1012.

[41] Schur, M., Berns, B., Dassenoy, A., Kassatkine, I., Urban, J., Wilmes, H., Hinrichsen, O., Muhler, M. and Schlögl, R., (2003). “Continuous Coprecipitation of Catalysts in a Micromixer: Nanostructured Cu/ZnO Composite for the Synthesis of Methanol”, Angewandte Chemie International Edition, 42(32):3815-3817.

[42] Espinal, L., Malinger, K.A., Espinal, A.E., Gaffney, A.M. and Suib, S.L., (2007). “Preparation of Multicomponent Metal Oxides Using Nozzle Spray and Microwaves”, Advanced Functional Materials, 17(14):2572-2579.

[43] Lochař, V. and Drobná, H., (2004). “FTIR Study of the Interaction of Crotonaldehyde and Maleic Anhydride with V_2O_5 and MoO_3”, Applied Catalysis A: General, 269(1-2):27-31.

[44] Taufiq-Yap, Y.H. and Waug, K.C., (2001). “A Study of the Nature of the Oxidant in V_2O_5–MoO_3/Al_2O_3 Catalyst”, Chemical Engineering Science, 56(20):5787-5792.

[45] Tichỳ, J., (1997). “Oxidation of Acrolein to Acrylic Acid over Vanadium-Molybdenum Oxide Catalysts”, Applied Catalysis A: General, 157(1-2):363-385.

[46] Imawan, C., Steffes, H., Solzbacher, F. and Obermeier, E., (2001). “Structural and Gas-sensing Properties of V_2O_5–MoO_3 Thin Films for H_2 Detection”, Sensors and Actuators, 77(1-2):346-351.

[47] Hu, X.K., Ma, D.K., Liang, J.B., Qin, X., Zhu, Y.C. and Qian, Y.T., (2007). “Hydrothermal Synthesis of $V_{0.13}Mo_{0.87}O_{2.935}$ Nanowires with Strong Blue Photoluminescence”, The Journal of Physical Chemistry C, 111(16):5882-5885.

[48] Hu, Y.T. and Davies, P.K., (1993). “Synthesis, Thermal Stability, and Structure of $(V_{.13}Mo_{.87})O_{2.935}$: A New Oxide with the Open "Hexagonal MoO_3" Structure”, Journal of Solid State Chemistry, 105(2):489-503.

[49] Dupont, L., Larcher, D. and Touboul, M., (1999). “The Phase Transitions between $H_{0.13}V_{0.13}Mo_{0.87}O_3 \cdot 0.26H_2O$ and MoO_3: An X-Ray, Thermal Analysis, and TEM Study”, Journal of Solid State Chemistry, 143:41-51.

[50] Timurkutluk, B., Celik, S., Timurkutluk, C., Mat, M.D. and Kaplan, Y., (2012). “Novel Electrolytes for Solid Oxide Fuel Cells with Improved Mechanical Properties”, International Journal of Hydrogen Energy, 37(18):13499-13509.

[51] Timurkutluk, B., Celik, S., Timurkutluk, C., Mat, M.D. and Kaplan, Y., (2012). “Novel Structured Electrolytes for Solid Oxide Fuel Cells”, Journal of Power Sources, 213:47-54.

[52] Timurkutluk, B., Celik, S., Toros, S., Timurkutluk, C., Mat, M.D. and Kaplan, Y., (2012). “Effects of Electrolyte Pattern on Mechanical and Electrochemical Properties of Solid Oxide Fuel Cells”, Ceramics International, 38(7):5651-5659.

[53] Perry, R.H. and Green, D.W., (1997). Perry’s Chemical Engineer’s Handbook, 7th Edition, Mc Graw Hill.

[54] Pillai, M.R., Kim, I., Bierschenk, D.M. and Barnett, S.A., (2008). “Fuel-flexible Operation of a Solid Oxide Fuel Cell with $Sr_{0.8}La_{0.2}TiO_3$ Support”, Journal of Power Sources, 185(2):1086-1093.

[55] Zhang, L., Jiang, S.P., He, H.Q., Chen, X., Ma, J. and Song, X.C., (2010). “A Comparative Study of H_2S Poisoning on Electrode Behavior of Ni/YSZ and Ni/GDC Anodes of Solid Oxide Fuel Cells”, International Journal of Hydrogen Energy, 35(22):12359-12368.

[56] Rasmussen, J.F.B. and Hagen, A., (2009). “The Effect of H_2S on the Performance of Ni–YSZ Anodes in Solid Oxide Fuel Cells”, Journal of Power Sources, 191(2):534-541.

[57] Hjalmarsson, P., Søgaard, M. and Mogensen, M., (2009). “Electrochemical Behaviour of $(La_{1-}xSrx)sCo_{1-}yNiyO_{3-\delta}$ as Porous SOFC Cathodes”, Solid State Ionics, 180(26-27):1395-1405.

[58] Hjalmarsson, P., Søgaard, M. and Mogensen, M., (2008). “Electrochemical Performance and Degradation of $(La_{0.6}Sr_{0.4})_{0.99}CoO_{3-\delta}$ as Porous SOFC-cathode”, Solid State Ionics, 179(27-32):1422-1426.

[59] Blennow, P., Hansen, K.K., Wallenberg, L.R. and Mogensen, M., (2006). “Effects of Sr/Ti-ratio in $SrTiO_3$-based SOFC Anodes Investigated by the Use of Cone-shaped Electrodes”, Electrochimica Acta, 52(4):1651-1661.

[60] Poulsen, F.W., Bonanos, N., Linderoth, S., Mogensen, M. and Zachau-Christiansen, B. “High Temperature Electrochemistry: Ceramics and Metals”, 17th Risø International Symposium on Materials Science, 1996, Risø National Laboratory, Roskilde, Denmark.

[61] Ebbesen, S.D. and Mogensen, M., (2009). “Electrolysis of Carbon Dioxide in Solid Oxide Electrolysis Cells”, Journal of Power Sources, 193:349-358.

[62] Primdahl, S. and Mogensen, M., (1999). “Gas Diffusion Impedance in Characterization of Solid Oxide Fuel Cell Anodes”, Journal of The Electrochemical Society, 146(8):2827-2833.

[63] Primdahl, S. and Mogensen, M., (1998). “Gas Conversion Impedance: A Test Geometry Effect in Characterization of Solid Oxide Fuel Cell Anodes”, Journal of The Electrochemical Society, 145(7):2431-2438.

[64] Barfod, R., Hagen, A., Ramousse, S., Hendriksen, P.V. and Mogensen, M., (2006). “Break Down of Losses in Thin Electrolyte SOFCs”, Fuel Cells, 6(2):141-145.

[65] Flores, O.G.M. and Ha, S., (2009). “Activity and Stability Studies of MoO_2 Catalyst for the Partial Oxidation of Gasoline”, Applied Catalysis A: General, 352(1-2):124-132.

[66] Afanasiev, P., (2008). “Synthetic Approaches to the Molybdenum Sulfide Materials”, Comptes Rendus Chimie, 11(1-2):159-182.

[67] Liu, M., Wei, G., Luo, J., Sanger, A.R. and Chuang, K.T., (2003). “Use of Metal Sulfides as Anode Catalysts in H_2S-Air SOFCs”, Journal of The Electrochemical Society, 150(8):A1025-A1029.

[68] Liu, M., (2004). H_2S-Powered Solid Oxide Fuel Cells, PhD Thesis, University of Alberta.

[69] Low, Q.X., Huang, W., Fu, X.Z., Melnik, J., Luo, J.L., Chuang, K.T. and Sagner, A.R., (2011). “Copper Coated Nickel Foam as Current Collector for H_2S-Containing Syngas Solid Oxide Fuel Cells”, Applied Surface Science, 258(3):1014-1020.

[70] Kosterina, E.V., Troyanov, S.I., Kemnitz, E. and Aslanov, L.A., (2001). “Synthesis and Crystal Structure of Acid Phosphites RbH_2PO_3, CsH_2PO_3, and TlH_2PO_3”, Russian Journal of Coordination Chemistry, 27(7):458-462.

[71] Kosterina, E.V., Troyanov, S.I., Aslanov, L.A. and Kemnitz, E., (2001). “Superacid Univalent Metal Phosphites $(MH_2PO_3)_2 \cdot H_3PO_3$ (M = Rb, Tl(I)) and $MH_2PO_3 \cdot H_3PO_3$ (M = K, Cs): Synthesis and Structure”, Russian Journal of Coordination Chemistry, 27(8):527-536.

[72] Chisholm, C.R.I. and Haile, S.M., (2000). “X-ray Structure Refinement of CsHSO4 in Phase II”, Solid State Ionics, 136-137:229-241.

[73] Cowan, L.A., Morcos, R.M., Hatada, N., Nevrotsky, A. and Haile, S.M., (2008). “High Temperature Properties of $Rb_3H(SO_4)_2$ at Ambient Pressure: Absence of a Polymorphic, Superprotonic Transition”, Solid State Ionics, 179:305-313.

[74] Dammak, M., Khemakhem, H., Zouari, N., Kolsi, A.W. and Mhiri, T., (2000). “Electrical properties of ferroelectric addition compound $K_2SeO_4 \cdot Te(OH)_6$”, Solid State Ionics, 127:125-132.

[75] Dammak, M., Khemakhem, H. and Mhiri, T., (2000). “Superprotonic Conduction and Ferroelectricity in Addition Cesium Sulfate Tellurate $Cs_2SO_4 \cdot Te(OH)_6$”, Journal of Physics and Chemistry of Solids, 62:2069-2074.

[76] Boudaya, C., Chabchoub, N., Khemakhem, H. and Von der Muhll, R., (2003). “Ionic Conduction and Dielectric Properties in the Telluric Sulfate $K_2(SO_4) \cdot Te(OH)_6$”, Journal of Alloys and Compounds, 352:304-308.

[77] Chabchoub, N. and Khemakhem, H., (2004). “AC Ionic Conductivity Investigations on the CsK(SO4)·Te(OH)6 Material”, Journal of Alloys and Compounds, 370:8-17.

[78] Ktari, L., Dammak, M., Hadrich, A., Cousson, A., Nierlich, M., Romain, F. and Mhiri, T., (2004). “Solid State Sciences Structural, Vibrational and Dielectric Properties of the New Mixed Solution $K_{0.84}(NH_4)_{1.16}SO_4 \cdot Te(OH)_6$”, Solid State Sciences, 6:1393-1401.

[79] Dammak, M., Ktari, L., Cousson, A. and Mhiri, T., (2005). "Structural and Conductivity Study of a New Protonic Conductor $Cs_{0.86}(NH_4)_{1.14}SO_4 \cdot Te(OH)_6$", Journal of Solid State Chemistry, 178:2109-2116.

[80] Chabchoub, N., Khemakhem, H. and Von der Muhll, R., (2005). "Dielectric, Electric and Raman Studies on the $RbK(SO_4) \cdot Te(OH)_6$ Material", Journal of Alloys and Compounds, 386:319-325.

[81] Dammak, M., Litaiem, H. and Mhiri, T., (2006). "Structural, Thermal and Dielectric Studies in $Na_2SeO_4 \cdot Te(OH)_6 \cdot H_2O$", Journal of Alloys and Compounds, 416: 228-235.

[82] Chabchoub, N., Darriet, J. and Khemakhem, H., (2006). "Structural and conductivity studies of $CsKSO_4 \cdot Te(OH)_6$and $Rb_{1.25}K_{0.75}SO_4 \cdot Te(OH)_6$ materials", Journal of Solid State Chemistry, 179:2164-2173.

[83] Abdelhedi, M., Ktari, L., Dammak, M., Cousson, A. and Kolsi, A.W., (2008). "DSC, Structural Single Crystal and X-ray Powder Diffraction Study of the Ammonium Sulfate Selenate Tellurate Mixed Solid Solution", Journal of Alloys and Compounds, 460:147-151.

[84] Ktari, L., Dammak, M., Kolsi, A.W. and Cousson, A., (2009). "Neutron Structural, X-ray Powder and Vibrational Studies of the Mixed Solid Solution Rubidium Ammonium Sulfate Tellurate", Journal of Alloys and Compounds, 476:54-59.

[85] Ktari, L., Abdelhedi, M., Bouhlel, N., Dammak, M. and Cousson, A., (2009). "Synthesis, Calorimetric, Structural and Conductivity Studies in a New Thallium Selenate Tellurate Adduct Compound", Materials Research Bulletin, 44:1792-1796.

[86] Goodhew, P.J., Humphreys, J. and Beanland, R., (2001). Electron Microscopy and Analysis, 3rd Edition, Taylor & Francis, London.

[87] Shigematsu, H., Akishige, Y., Mashiyama, H., Tojo, T., Kawaji, H., Atake, T. and Matsui, T., (2005). "Heat Capacity, X-Ray Scattering and Neutron Scattering Studies in Rb_2SeO_4", Journal of the Korean Physical Society, 46(1):235-238.

[88] Shigematsu, H., Akishige, Y., Matsui, T., Tojo, T., Kawaji, H. and Atake, T., (2005). "Structures and phase transitions in $(K_{1-x}Rb_x)_2SeO_4$", Journal of Thermal Analysis and Calorimetry, 81(3):555-558.

[89] Ghedia, S., Dinnebier, R. and Jansen, M., (2009). "The Crystal Structure of Rb_2SeO_4 at High Temperature", Solid State Sciences, 11:72-76.

[90] Gattow, G., (1962). "Die Kristallstrukturen von K_2SeO_4, Rb_2SeO_4 und Cs_2SeO_4", Acta Crystallographica, 15(4):419.

[91] Haas, K.H. and Schindewolf, U., (1984). "The Electrical Conductivity of Solid Alkali Hydroxides", Journal of Solid State Chemistry, 54(3):342-345.

[92] Spaeth, M., Kreuer, K.D., Dippel, T.H. and Maier, J., (1997). "Proton Transport Phenomena in Pure Alkaline Metal Hydroxides", Solid State Ionics, 97(1-4):291-297.

[93] Stephen, P.M.S. and Howe, A.T., (1980). "Proton Conductivity and Phase Relationship in Solid KOH between 248 and 406°C", Solid State Ionics, 1(1-5):461-471.

[94] Verma, V.P., (1999). "A Review of Synthetic, Thermoanalytical, IR, Raman and X-ray Studies on Metal Selenites", Thermochimica Acta, 327(1-2):63-102.

[95] Lenher, V. and Wochter, E.J., (1925). "Selenic Said and the Selenates", Journal of the American Chemical Society, 47(6):1522-1523.

[96] Ikeda, A. and Haile, S.M., (2012). "The Thermodynamics and Kinetics of the Dehydration of CsH_2PO_4 $_S$tudied in the Presence of SiO_2", Solid State Ionics, 213:63-71.

[97] Otomo, J., Ishigooka, T., Kitano, T., Takahashi, H. and Nagamoto, H., (2008). "Phase Transition and Proton Transport Characteristics in CsH_2PO_4/SiO_2 Composites", Electrochimica Acta, 53:8186-8195.

[98] Ponomareva, V.G. and Shutova, E.S., (2007). "High-Temperature Behavior of CsH_2PO_4 and CsH_2PO_4-SiO_2 Composites", Solid State Ionics, 178:729-734.

[99] Otomo, J., Minagawa, N., Wen, C.J., Eguchi, K. and Takahashi, H., (2003). "Protonic Conduction of CsH_2PO_4 and its Composite with Silica in Dry and Humid Atmospheres", Solid State Ionic, 156:357-369.

[100] Ponomareva, V.G., Uvarov, N.F., Lavrova, G.V. and Hairetdinov, E.F., (1996). "Composite Protonic Solid Electrolytes in the CsH_2PO_4-SiO_2 System", Solid State Ionics, 90:161-166.

[101] Ponomareva, V.G., Lavrova, G.V. and Simonova, L.G., (1999). "Effect of SiO_2 Morphology and Pores Size on the Proton Nanocomposite Electrolytes Properties", Solid State Ionics, 119:295-299.

[102] Wang, S., Otomo, J., Ogura, M., Wen, C., Nagamoto, H. and Takahashi, H., (2005). "Preparation and Characterization of Proton-Conducting $CsHSO_4$-SiO_2 Nanocomposite Electrolye Membranes", Solid State Ionics, 176:755-760.

[103] Rada, S., Pascuta, P., Rada, M. And Culea, E., (2011). "Effects of Samarium (III) Oxide Content on Structural Investigation of the Samarium-Vanadate-Tellurate Glasses and Glass Ceramics", Journal of Non-Crystalline Solids, 357:3405-3409.

[104] Suzuki, T., Shiosaka, T.W., Miyoshi, S. and Ohishi, Y., (2011). "Computational and Raman Studies of Phospho-Tellurite Glasses as Ultrabroad Raman Gain Media", Journal of Non-Crystalline Solids, 357:2702-2707.

[105] Holland, D., Bailey, J., Ward, G., Turner, B., Tierney, P. And Dupree, R., (2005). "A ^{125}Te and ^{23}Na NMR Investigatıın of the Structure and Crystallisation of Sodium Tellurite Glasses", Solid State Nuclear Magnetic Resonance, 27:16-27.

[106] Jayaseelan, S., Muralidharan, P., Venkateswarlu, M. and Satyanarayana, N., (2004). "Ion Transport and Relaxation Studies of Silvervanadotellurite Glasses at Low Temperatures", Materials Chemistry and Physics, 87:370-377.

[107] Rada, S. and Culea, E., (2009). "FTIR Spectroscopic and DFT Theoretical Study on Structure of Europium–phosphate–tellurate Glasses and Glass Ceramics", Journal of Molecular Structure, 929:141-148.

[108] Mošner, P., Vosejpková, K., Koudelka, L., Montagne, L. and Revel, B., (2010). "Structure and Properties of ZnO–B2O3–P2O5–TeO2 Glasses", Materials Chemistry and Physics, 124:732-737.

[109] Rada, S., Dehelean, A. and Culea, E., (2011). "FTIR and UV-VIS Spectroscopy Investigations on the structure of the Europium–Lead–Tellurate Glasses", Journal of Non-Crystalline Solids, 357:3070-3073.

[110] Rada, S., Culea, E. And Rada, M., (2011). "The Experimental and Theoretical Investigations on the Structure of the Gadolinium–lead–tellurate Glasses", Materials Chemistry and Physics, 128:464-469.

[111] Rada, M., Maties, V., Rada, S. and Culea, E., (2010). "Novel Layered Structures in Lead–vanadate–tellurate Unconventional Glass Ceramics", Journal of Non-Crystalline Solids, 356:1267-1271.

[112] Rada, S., Neumann, M. and Culea, E., (2010). "Experimental and Theoretical Investigations on the Structure of the Lead–vanadate–tellurate Unconventional Glasses", Solid State Ionics, 181:1164-1169.

[113] Rada, S., Pascuta, P., Rada, M. and Culea, E., (2011). "Effects of Samarium (III) Oxide Content on Structural Investigations of the Samarium–vanadate–tellurate Glasses and Glass Ceramics", Journal of Non-Crystalline Solids, 357:3405-3409.

[114] Rada, S., Culea, M. and Culea, E., (2008). "Structure of $TeO_2.B_2O_3$ Glasses Inferred from Infrared Spectroscopy and DFT Calculations", Journal of Non-Crystalline Solids, 354:5491-5495.

[115] Mošner, P., Vosejpková, K., Koudelka L., Montagne, L. and Revel, B., (2011). "Structure and Properties of Glasses in $ZnO–P_2O_5–TeO_2$ System", Journal of Non-Crystalline Solids, 357:2648-2652.

[116] Szu, S. and Chang, F.S., (2005). "Impedance Study of $V_2O_5–TeO_2–BaO$ Glasses", Solid State Ionics, 176:2695-2699.

[117] Rodrigues, A.C.M., Keding, R. And Russel, C., (2000). "Mixed Former Effect between TeO_2 and SiO_2 in the $Li_2O·TeO_2·SiO_2$ System", Journal of Non-Crystalline Solids, 273:53-58.

[118] Holland, D., Bailey, J., Ward, G., Turner, B., Tierney, P. and Dupree R., (2005). "A ^{125}Te and ^{23}Na NMR Investigation of the Structure and Crystallisation of Sodium Tellurite Glasses", Solid State Nuclear Magnetic Resonance, 27:16-27.

[119] Munoz-Martín, D., Villegas M.A., Gonzalo J. and Fernández-Navarro, J.M., (2009). "Characterisation of Glasses in the $TeO_2–WO_3–PbO$ System", Journal of the European Ceramic Society, 29:2903-2913.

[120] Noguera, O., Jouin J., Masson, O., Jancar, B. and Thomas, P., (2012). "Phase Formation and Crystal Structure Determination in the Y_2O_3–TeO_2 System Prepared in an Oxygen Atmosphere", Journal of the European Ceramic Society, DOI:10.1016/j.jeurceramsoc.2012.07.015.

[121] Shivachev, B.L., Petrov, T., Yoneda,H., Titorenkova, R. and Mihailova, B., (2009). "Synthesis and Nonlinear Optical Properties of TeO_2–Bi_2O_3–GeO_2 Glasses", Scripta Matterialia, 61:493-496.

[122] Tadanaga, K, Yamashita, Y., Hayashi, A. and Tatsumisago, M., (2010). "Preparation of Proton Conducting Ionic Glasses in the Systems $CsHSO_4$-$MHSO_4$ (M=Na, K, Rb)", Solid State Ionics, 181:187-189.

[123] Taninouchi, Y.K., Uda, T. and Awakura, Y., (2008). "Dehydration of CsH_2PO_4 at Temperatures Higher than 260 ºC and the Ionic Conductivity of Liquid Product", Solid State Ionic, 178:1648-1653.

[124] Park, J.H., (2004). "Possible Origin of the Proton Conduction Mechanism of CsH_2PO_4 Crystals at High Temperatures", Physical Review B, 69:0541041-0541046.

[125] Hosseini, S., Homaiee, M., Mohamad, A.B., Malekbala, M.R. and Khadum, A.A.H., (2011). "Surfactant Effect on the Conductivity Behavior of CsH_2PO_4: Characterization by Electrochemical Impedance Spectroscopy", Physica B, 406:1689-1694.

BACKGROUND

PERSONAL

Name Surname	: D. Berceste BEYRİBEY
Birthday and Place	: 1st April 1980, İstanbul, Turkey
Languages	: Turkish (Native) English (Advanced)
E-mail	: b_berceste@hotmail.com, berceste@yildiz.edu.tr

EDUCATION

Degree	**Field**	**School/University**	**Graduation Year**
MSc	Chemical Engineering	Yıldız Technical University	2006
BSc	Chemical Engineering	Yıldız Technical University	2004
High School	Art&Science	İstanbul Sabri Çalışkan	1997

EXPERIENCE

2005-continued	Yıldız Technical University	Research and Teaching Assistant

PUBLICATIONS

Peer Reviewed Publications

International Journals

1. Beyribey B., Hallinder J., Poulsen F.W., Bonanos N. and Mogensen M. (2012), “Studies of rubidium selenate with secondary phase of RbOH under humidified reducing atmosphere”, Journal of Alloys and Compounds, DOI:10.1016/j.jallcom.2012.08.034

2. Beyribey B. and Hallinder J. (2012), Structural, thermal and electrical studies of a novel rubidium phosphite tellurate compound, Ceramics International, 33(6), 5095-5102.

3. Beyribey B. (2012), A new way of synthesis of hexagonal $V_{0.13}Mo_{0.87}O_{2.935}$ and an investigation on its structural, thermal and anodic properties, Research on Chemical Intermediates, DOI: 10.1007/s11164-012-0676-9.

4. Ismail O. and **Beyribey B.**, (2012), Swelling Characterization of the Superabsorbent Copolymer in the Petroleum-Based Solvent-Water Mixtures, Journal of Macromolecular Science, Part A, 49(5), 432-438.

5. Ismail O. and **Beyribey B.**, (2012), Open-air sun drying in Thrace region of Greece: The experimental investigation of thyme and mint leaves, Latin American Applied Research, Accepted.

6. Ismail, O., **Beyribey, B.** and Turhan, K., (2011), “Removal of Water in Liquid Fuel with Super Absorbent Copolymer”, Energy Sources, Part A: Recovery, Utilization and Environmental Effects, 33(18), 1669-1667.

7. Yarman, A., **Beyribey B.** and Afsar H., (2010), “Usage of Solid Paraffin for Purification, Storage and Handling of Metallic Sodium”, Asian Journal of Chemistry, 22 (2), 1645-1646.

8. Ismail, O., Keyf, S., **Beyribey B** and Corbacioglu, B., (2008), “Effects of Dipping Solutions on Air-Drying Rates of the Seedless Grapes”, Food Science and Technology Research, 14 (6): 547-552.

National Journal

1. ***Beyribey, B.,*** Corbacioglu, B. and Altin, Z. “Synthesis of Platinum Particles from H_2PtCl_6 with Hydrazine as Reducing Agent”, (2009), G.U. Journal of Science, 21(2): 33-36.

Proceedings and Presentations

1. Berceste Beyribey, Burcu Çorbacıoğlu, Zehra Altın, Seyfettin Erturan, "The Synthesis of Transition Metal Sulfide Catalysts for H_2S-Powered Solid Oxide Fuel Cells", 2010, 5th International Ege Energy Symposium and Exhibition (IEESE-5), June 27-30th, Denizli, Turkey. *(Oral Presentation)*

2. Osman Ismail, **Berceste Beyribey**, İbrahim Doymaz, "The Effect of the Absorbent Polymers on Removal of Water in Liquid Fuel", 2010, 5th International Ege Energy Symposium and Exhibition (IEESE-5), June 27-30th, Denizli, Turkey. *(Poster Presentation)*

3. Berceste Beyribey, Zehra Altin, Burcu Corbacioglu and Seyfettin Erturan, "Effects of Reducing Agent, pH Value and Temperature on Platinum Particle Size", 2008, Knowledge Management for Composite Materials (KMCM 2008), July 08-11th, Vancouver, Canada. *(Oral Presentation)*

4. Berceste Beyribey, Huseyin Afsar, Seyfettin Erturan and Zehra Altin, "The Production of Sodium Borohydride by a Novel Electrolysis Method", 2007, 2nd International Hydrogen Energy Congress & Exhibition, July 13-15th, Istanbul, Turkey. *(Oral Presentation)*

5. Berceste Beyribey, Zehra Altin, Burcu Corbacioglu and Seyfettin Erturan, "Human Health and Environmental Assessment of batteries, accumulators and fuel cells", 2009, National Solid Waste Assessment Congress, May 27-29th, Eskisehir, Turkey. *(Poster Presentation)*

6. Berceste Beyribey and Burcu Corbacioglu, "Recovery of Precious Metal from Electronic Waste", 2009, National Solid Waste Assessment Congress, May 27-29th, Eskisehir, Turkey. *(Oral Presentation)*

7. Berceste Beyribey, Zehra Altin, Burcu Corbacioglu and Seyfettin Erturan, "Comparison of Claus Process with Solid Oxide Fuel Cells for production of elemental sulfur", 2008, 7th National Clean Energy Symposium, December 17-19th, Istanbul, Turkey. *(Oral Presentation)*

8. Berceste Beyribey, Zehra Altin, Burcu Corbacioglu and Seyfettin Erturan, "Methods for Hydrogen Sulfide and Environmental Assessment", 2008, National Symposium on Air Pollution and Its Control, October 22-25th, Hatay, Turkey. *(Poster Presentation)*

9. Berceste Beyribey, Zehra Altın and Burcu Corbacioglu, "The Production of Sodium Borohydride by Electrolysis", 22rd National Chemistry Congress, 2008, October 06-10th, Magusa, Cyprus. *(Poster Presentation)*

10. Berceste Beyribey, Seyfettin Erturan and Zehra Altin, "Solid Oxide Fuel Cells Operating by Hydrogen Sulfide as a Fuel and Its environmental value", 2008, Environmental Problems Symposium, May 14-17th, Kocaeli, Turkey. *(Oral Presentation)*

11. Berceste Beyribey, Huseyin Afsar, Seyfettin Erturan and Zehra Altin, "The synthesis of PtRu/C and PtIr/C composite electrodes for H_2-O_2 fuel cells", 2006, 7th National Chemical Engineering Congress, September 05-08th, Eskisehir, Turkey. *(Poster Presentation)*

Funded Projects

International

1. "Hydrogen production from H_2S decomposition in micro-structured proton-conducting solid oxide membrane reactors", BS-ERA.NET Project, Researcher (01.12.2011-continued).

National

1. "Preparation and development of hydrophobic/oleophobic functional surface coating materials to be used on glass surfaces", Research Fund of Yildiz Technical University, Researcher (01.09.2011-continued).

2. "Production and mathematical modeling of a solid oxide fuel cell operating at low temperatures by using H_2S as fuel", Project No: 27-07-01-05, Research Fund of Yildiz Technical University, Researcher (2007-2010).

3. "Hydrogen production from different compounds and development of fuel cell - Production of sodium tetraborate from Turkish boron compounds", Project No: 23-DPT-07-01-01, T.R. Prime Ministry State Planning Organization, Researcher (2003-2006).